
Multi-Visual-Inertial Sensor Calibration: Analysis, Calibration and Estimation

Yulin Yang - yuyang@udel.edu
Patrick Geneva - pgeneva@udel.edu
Guoquan Huang - ghuang@udel.edu

Department of Mechanical Engineering
University of Delaware, Delaware, USA

RPNG

Robot Perception and Navigation Group (RPNG)
Tech Report - RPNG-2023-MVIS
Last Updated - November 20, 2023

Contents

1	Introduction	1
2	Related Work	3
2.1	Multi-inertial navigation	3
2.2	Multi-camera aided inertial navigation	4
2.3	Multi-camera and multi-IMU navigation	5
3	Multi-Visual-Inertial System	5
3.1	IMU Model	5
3.2	Camera Model	7
3.3	State Vector	8
3.4	NLS Formulation	9
4	ACI³: Preintegration with Intrinsics	10
4.1	Pre-integration Terms	11
4.2	Recursive Formulation	11
4.3	Mean Prediction	12
4.4	Covariance Prediction	14
5	Base Inertial Costs	17
6	Auxiliary Inertial Costs	19
6.1	Auxiliary IMU Cost	20
6.2	Auxiliary Gyroscope Cost	21
6.3	Auxiliary Inertial Sensor Initialization	22
7	Visual Costs	22
8	Observability Analysis	24
8.1	Reduced State Vector	24
8.2	Linearized Observability Analysis	25
9	Degenerate Motion Analysis	28
9.1	Spatiotemporal Calibration of Auxiliary Inertial Sensors	28
9.1.1	No Rotation	29
9.1.2	One-Axis Rotation	29
9.1.3	Constant Local Angular Velocity	29
9.1.4	Constant Local Angular and Global Linear Velocity	29
9.1.5	Constant Local Angular and Linear Velocity	30
9.2	Intrinsics for Auxiliary Inertial Sensors	30
10	Simulation Results	36
10.1	Fully-Excited Motion	37
10.2	Degenerate One-Axis Motion	37
10.3	Degenerate Circular-Planar Motion	37

11 Experimental Results	38
11.1 4 IMUs + 3 GS Cameras	38
11.1.1 Calibration with Different Number of Cameras	44
11.1.2 Comparison with Kalibr	44
11.1.3 Comparing IMU Intrinsic Quality	44
11.2 4 IMUs + 2 GS Cameras + 2 RS Cameras	45
11.2.1 Calibration for IMU and GS/RS	45
11.2.2 Evaluation of Multiple Gyroscopes Calibration	45
11.2.3 Temporal Calibration	46
11.3 Planar Motion with 4 IMUs + 2 GS Cameras	46
11.4 Discussion on Estimation Convergence	46
Appendix A Degenerate Motion For Inertial Intrinsics	50
A.0.1 $^w w_1$ constant	50
A.0.2 $^w w_2$ constant	50
A.0.3 $^w w_3$ constant	50
A.0.4 $^a a_1$ constant	50
A.0.5 $^a a_2$ constant	51
A.0.6 $^a a_3$ constant	51
References	52

Abstract

In this paper, we study state estimation of multi-visual-inertial systems (MVIS) and develop sensor fusion algorithms to optimally fuse an arbitrary number of asynchronous inertial measurement units (IMUs) or gyroscopes and global and/or rolling shutter cameras. We are especially interested in the full calibration of the associated visual-inertial sensors, including the IMU/camera intrinsics and the IMU-IMU/camera spatiotemporal extrinsics as well as the image readout time of rolling-shutter cameras (if used). To this end, we develop a new analytic combined IMU integration with inertial intrinsics – termed ACI³ – to pre-integrate IMU measurements, which is leveraged to fuse auxiliary IMUs and/or gyroscopes alongside a base IMU. We model the multi-inertial measurements to include all the necessary inertial intrinsic and IMU-IMU spatiotemporal extrinsic parameters, while leveraging IMU-IMU rigid-body constraints to eliminate the necessity of auxiliary inertial poses and thus reducing computational complexity. By performing observability analysis of MVIS, we prove that the standard four unobservable directions remain – no matter how many inertial sensors are used, and also identify, for the first time, degenerate motions for IMU-IMU spatiotemporal extrinsics and auxiliary inertial intrinsics. In addition to the extensive simulations that validate our analysis and algorithms, we have built our own MVIS sensor rig and collected over 25 real-world datasets to experimentally verify the proposed calibration against the state-of-the-art calibration method Kalibr. We show that the proposed MVIS calibration is able to achieve competing accuracy with improved convergence and repeatability, which is open sourced to better benefit the community.

1 Introduction

A camera can provide 2 degree-of-freedom (DoF) texture-rich images of the environment while an inertial measurement unit (IMU), which consists of a gyroscope and an accelerometer, can read high-frequency angular velocity from its gyroscope and linear acceleration from its accelerometer. The combination of cameras and IMUs have become prevalent in autonomous vehicles and mobile devices in the recent decade due to their decrease in cost and complementary sensing nature. This has lead to a significant progress of developing visual-inertial navigation system (VINS) algorithms focusing on efficient and accurate pose estimation [1]. While many works have shown accurate estimation for the minimal sensing case of a single camera and IMU [2, 3, 4, 5, 6], it is known that the inclusion of additional sensors can provide improved accuracy due to additional information and robustness to single sensor failure cases [7, 8]. Recently, multi-visual-inertial systems (MVIS) – which uses multiple IMUs and multiple cameras for 6 DoF pose tracking and 3D mapping – have been deployed to micro aerial vehicles (MAVs), AR/VR devices and autonomous vehicles, thus the need for accurate sensor calibration and state estimation algorithms continues to grow. We have previously investigated the single IMU-Camera calibration case [9], showing that even a small perturbation to calibration parameters may cause significant trajectory accuracy loss, which calls for accurate calibration of MVIS.

Regarding state estimation, many works have explored to use multiple vision sensors for better VINS performance [10, 11, 7, 12, 13, 14, 15]. In particular, [10], [11] and [15] have shown that stereo camera or multiple cameras can achieve better pose accuracy or lower the uncertainties of IMU-Camera calibration. Only a few works recently investigate multiple inertial sensor fusion for VINS [16, 17, 18, 19, 20], showing that the system robustness and pose accuracy can be improved by fusing additional IMUs. For optimal fusion of multiple asynchronous visual and inertial sensors for MVIS, it is crucial to provide accurate full-parameter calibration for these sensors, which include: (i) IMU-IMU/camera rigid transformation, (ii) IMU-IMU/camera time offset, (iii) IMU inertial intrinsics, including scale/skewness correction for gyroscope/accelerometer, g-sensitivity, and rotation between

gyroscope and accelerometer , (iv) camera projection/distortion model parameters, and (v) image readout time of rolling shutter (RS) cameras.

While there exists literature regarding to multi-camera and multi-IMU navigation systems [21, 22, 16, 6, 8, 15, 23], most of these works do not support full parameter calibration. For example, only synchronized multiple global shutter (GS) cameras are supported in [6, 15], which cannot handle measurements from multiple asynchronous inertial sensors or rolling shutter cameras . Only rigid transformations for multiple IMUs can be calibrated in the work of [16]. Although the work [23] can handle the spatiotemporal calibration for asynchronous cameras and IMUs, rolling shutter (RS) calibration and IMU/camera intrinsic calibration are missing. The work [8] can calibrate multiple asynchronous RS cameras but the IMU intrinsic parameters (including scale/skewness correction and g-sensitivity) cannot be estimated. Although the work [21] and its extension [22] support the spatiotemporal calibration for multiple IMUs and cameras with their intrinsics, they do not support hybrid calibration of global and rolling shutter (GS/RS) cameras. The IMU-IMU or IMU-Camera time offsets cannot be jointly optimized, either. None of the aforementioned works can perform joint optimization of all the mentioned calibration parameters.

In this paper, we are aiming for full-parameter joint calibration of MVIS, including IMU-IMU/Camera spatiotemporal calibration, IMU/Camera intrinsics and rolling shutter readout time. The joint calibration can benefit the sensor fusion (e.g., VINS, MVIS) in several aspects. [24] showed that calibrating the full-parameter model when running VINS can improve the system accuracy than calibrating partial IMU-Camera model parameters. [25] showed that jointly calibrating rolling shutter and IMU intrinsics can lower down image reprojection errors, and hence, improve the pose accuracy. [22] showed in their experiments that joint IMU intrinsic calibration can also improve the IMU-Camera extrinsic calibration. Joint full-parameter calibration for a multi-sensor system might be more convenient and efficient than calibrating each sensor individually. For example, if calibrating the IMU intrinsics, a turntable with a special fixture for an IMU might be needed for accurate calibration. Several data collections might also be performed to make sure all the IMUs can be reliably calibrated. The joint sensor calibration algorithm can calibrate the parameters of all the IMUs with one data collection without special setup for the IMUs. Joint calibration for a multi-sensor system can also leverage more information (e.g., multi-sensor rigid-body constraints, data association from multiple cameras) to improve calibration performances. [15] showed that joint calibration of a multiple-camera system can greatly reduce the camera related calibration uncertainties than a single camera system. Note that in the following paper, we refer to the MVIS containing multiple IMUs (IMU-IMU) or at least one IMU with additional gyroscopes (IMU-gyroscope). We specifically mention the gyroscopes, because they can read the angular velocities for the same sensor platform to which they are rigidly attached. Hence, it is straightforward to improve orientation estimation by fusing these gyroscopes readings with pretty efficient algorithms [18]. Even with multiple extra IMUs, we can fuse only the gyroscopes from these IMUs for the consideration of saving the computation complexity by not processing the noisy acceleration measurements.

Moreover, no observability analysis focusing on MVIS is performed. In particular, the degenerate motion study of the spatiotemporal calibration for IMU-IMU/gyroscope is missing from the literature , which greatly limits our understanding of such kind system.

To fill this gap, we first leverage our previous work on analytic combined IMU integration [26] to derive a new IMU integrator for IMU intrinsic calibration (i.e., ACI³). Different from previous IMU pre-integration algorithms [4, 27, 28], ACI³ models accurate covariance correlations between IMU navigation states (IMU pose and velocity) and biases. It also analytically computes Jacobians regarding to both the biases and IMU intrinsics. Based on this, we design a novel algorithm to fuse multiple IMU/gyroscope measurements by using the rigid body constraints between these inertial sensors. A complete MVIS algorithm is developed , which can truly jointly estimate all the calibra-

tion parameters (spatiotemporal parameters between IMU-IMU/camera, IMU/camera intrinsics, readout time) within a batch nonlinear least squares (NLS) optimization framework. Based on the linearized system models, observability analysis of MVIS with full-calibration is performed. We show that all these calibration parameters are observable given fully excited motions, and also, for the first time, identify the degenerate motions for IMU-IMU/gyroscope spatiotemporal calibration. By building our own MVIS sensor rig with multiple IMUs and GS/RS cameras for data collection, we validate the proposed system against the state-of-art Kalibr [21, 22]. In particular, the main contributions of this work are the following:

- We propose an optimization-based multi-visual-inertial (IMU and/or gyroscope) sensor calibration algorithm, which jointly estimates *all* spatiotemporal (including RS readout time) and intrinsic parameters for an arbitrary number of visual and inertial sensors.
- Building upon our prior work [26], we develop a new analytic combined IMU integrator with inertial intrinsics (i.e., ACI³), which corrects both mean and covariance of pre-integrated IMU measurements when IMU bias and intrinsic linearization changes. We also propose an auxiliary IMU fusion algorithm that allows for both the extrinsic and intrinsic calibration for multiple IMU sensors.
- We perform comprehensive observability analysis for the MVIS with full-parameter calibration, and, for the first time, identify the degenerate motions related to IMU-IMU/gyroscope calibration. We show that under one-axis rotation motion, the rotation between IMU and gyroscope is unobservable along rotation axis. We also show that under constant local angular and linear velocity, the time offset between IMUs is observable, which counters our intuitions.
- We conduct extensive simulations with three typical motion profiles. The simulation results confirm that we are able to recover all visual and inertial calibration parameters with the proposed MVIS in the fully-excited motion case. Specifically, 25 datasets collected by our self-made sensor rig are also used for evaluating the proposed MVIS against state-of-art calibration methods, and the results prove that the proposed approach achieves comparable accuracy and better repeatability. The identified degenerate motions for the pertinent calibration parameters are also verified through both simulation and real-world experiments.

The paper is organized as follows: after briefly reviewing the related works in the next section, we present the proposed MVIS estimation framework in Section 3. The visual-inertial measurement constraints used by the system are explained in Sections 4-7, while in Sections 8-9 we present the observability analysis and identified degenerate motions. We validate our analysis and algorithms in Sections 10-11 and conclude the paper in Section ??.

2 Related Work

While there exists rich literature in VINS [1], in the following, we only review the works closely related to MVIS and the calibration of MVIS, which can be categorized as: (i) multiple inertial sensors aided navigation systems, (ii) multiple cameras aided inertial navigation systems, and (iii) multi-camera and multi-IMU navigation systems.

2.1 Multi-inertial navigation

There are a few works using multiple inertial sensors to improve navigation system. [19] proposed to use triple IMUs with wheel encoders to improve dead reckoning and showed that the drifting rates

continue dropping as the number of used IMU increases. [20] proposed to use best axes composition (BAC) algorithm to select the best fitting data from multiple inertial sensors to avoid systematic errors when fusing multiple customer grade IMUs. They showed that the inertial navigation system performances can be improved by increasing the number of used inertial sensors. [16] fused multiple IMUs through reformulating pre-integration [4] by transforming the auxiliary inertial readings into the base inertial frame. However, they relied on the numerical computation of angular accelerations to perform this transformation. They did not estimate the IMU-IMU related calibration parameters, either.

[18] proposed to convert the readings from multiple IMUs into a single “virtual” synthetic IMU measurement, which is expected to be less noisy. While offering computational savings compared to other multi-inertial fusion algorithms, it relies on having perfectly known spatiotemporal calibration for these inertial sensors. It is clear that the above mentioned works all assume the high-accuracy IMU-IMU calibration is provided and they leverage multiple IMUs but with only one camera for pose estimation. [29] showed that the fusion of three low-cost calibrated IMUs can be used to achieve similar pose tracking performances as a single high-end IMU in the application of tracking head mounted device (HMD). They also proposed to use static IMU measurements to calibrate accelerometer intrinsics and non-static IMU measurements to calibrate the gyroscope intrinsics. [30] proposed an extrinsic calibration algorithm for multiple IMUs when these IMUs are rigidly connected and moving arbitrarily. Only measurements from these IMUs are needed for the calibration. However, the time offsets between these IMUs and the IMU intrinsic calibration are all missing from this work.

Although all the above mentioned works have shown that fusion of multiple IMUs to wheel-INS or VINS can improve pose tracking accuracy, most of them rely entirely or partially on high-accuracy prior calibration of these IMUs: including IMU-IMU spatiotemporal calibration and the inertial intrinsics of these IMUs. Instead, this paper aim to solve the full parameter calibration for multiple IMUs, including intrinsics, extrinsics and time offsets, especially for the application of multiple inertial sensors in VINS domain.

2.2 Multi-camera aided inertial navigation

There have been quite a few works investigating fusing observations from multiple cameras for visual-inertial navigation. Processing all the measurements from multiple cameras will significantly slow down the system. Hence, [13] proposed an information based keyframe selection algorithm for efficient multi-camera fusion. [31] proposed an efficient feature selection and tracking algorithm to speed up the measurement processing for multiple cameras. These two works only fuse visual observations from multiple cameras but without considering the sensor calibration. [15] proposed to use multiple synchronized cameras to improve IMU-Camera calibration. They proved that the extrinsic covariance bound will be smaller when more cameras are used. This indicates that the IMU-Camera calibration can converge faster with more confidences. Our previous work, OpenVINS [6] supports synchronized multi-camera aided VINS with extrinsic, intrinsic and temporal calibration between IMU and camera. However, rolling shutter cameras are not supported by either of the above works.

In this paper, the proposed MVIS support the extrinsic and intrinsic calibration for multiple asynchronous global shutter or rolling shutter cameras. We provide quantitative analysis for how the calibration estimates is improved when 1, 2, or 3 cameras are used simultaneously. In addition, the proposed MVIS supports simultaneous calibration of global shutter and rolling shutter cameras with image readout time.

2.3 Multi-camera and multi-IMU navigation

There are only a few works focusing on joint calibration for multiple cameras and multiple IMUs. [23] proposed MultiCal, which exploits continuous-time curves to represent pose states and supports the spatial and temporal calibration for multiple IMUs and cameras with planar targets. However, rolling shutter camera calibration and IMU/camera intrinsic calibration are not supported. [8] proposed a filter based framework for fusing multiple IMUs and multiple cameras by estimating each auxiliary IMU with full state (containing orientation, position, velocity, and biases), and enforced relative pose constraints between sensors at fixed rates. It also showed robustness to inertial sensor failures. This work does not take into account the inertial intrinsic parameters and only includes the IMU-IMU/camera spatiotemporal calibration. Additionally, their multi-IMU constraints required an additional 6 DoF pose for each auxiliary IMU since each IMU is propagated independently forward. [22], extended the continuous-time Kalibr framework [21], to calibrate the extrinsic and intrinsic parameters of auxiliary inertial sensors by formulating the angular velocity and linear accelerations as functions of the trajectory spline derivatives. However, when performing IMU-camera and IMU-IMU calibration, the camera intrinsics and IMU-IMU time offset are fixed instead of jointly optimized with other parameters. It does not support visual-inertial rolling shutter calibration. In addition, no theoretical consistency analysis or 3 sigma plots for IMU intrinsic calibration are provided for validation.

Unlike the above mentioned works, the proposed MVIS supports multiple IMU/gyroscope calibrations with both global shutter and rolling shutter cameras. All related parameters, including IMU/camera intrinsics, spatial and temporal parameters between IMUs and cameras, can be calibrated. In addition, we also, for the first time, provide MVIS observability analysis, which shows that all these calibration parameters are observable given fully excited motions. We also investigate the degenerate motions that might cause certain calibration parameter to fail, especially for IMU-IMU/gyroscope spatiotemporal calibrations.

3 Multi-Visual-Inertial System

In this section, we first present the full IMU model (containing scales, axis-misalignment and g-sensitivity) and camera model (containing camera intrinsics, lens distortion and RS readout time) in the MVIS. We then introduce the state vector containing all the calibration parameters for an arbitrary number of IMUs and cameras, followed by the nonlinear least-squares (NLS) formulation.

3.1 IMU Model

An IMU is assumed to consist of two separate frames [9]: gyroscope frame $\{w\}$ and accelerometer frame $\{a\}$. The “inertial” frame $\{I\}$ is chosen to coincide with either $\{w\}$ or $\{a\}$ (see Fig. 1). Similar to the IMU models in [24, 32, 9], the raw angular velocity ${}^w\omega_m$ from the gyroscope and linear acceleration ${}^a\mathbf{a}_m$ from accelerometer is written as:

$${}^w\omega_m = \mathbf{T}_w {}^w\mathbf{R}^I \boldsymbol{\omega} + \mathbf{T}_g {}^I\mathbf{a} + \mathbf{b}_g + \mathbf{n}_g \quad (1)$$

$${}^a\mathbf{a}_m = \mathbf{T}_a {}^a\mathbf{R}^I \mathbf{a} + \mathbf{b}_a + \mathbf{n}_a \quad (2)$$

where \mathbf{T}_w and \mathbf{T}_a denote the scale and axis misalignment for $\{w\}$ and $\{a\}$, respectively. \mathbf{T}_g represents the g-sensitivity. ${}^w\mathbf{R}$ and ${}^a\mathbf{R}$ denote the rotation from the gyroscope and acceleration frame to base “inertial” $\{I\}$, respectively. Note that the translation between the gyroscope and the accelerometer ${}^a\mathbf{p}_w$ has been safely ignored in most VINS algorithms [24, 33, 32, 34], probably

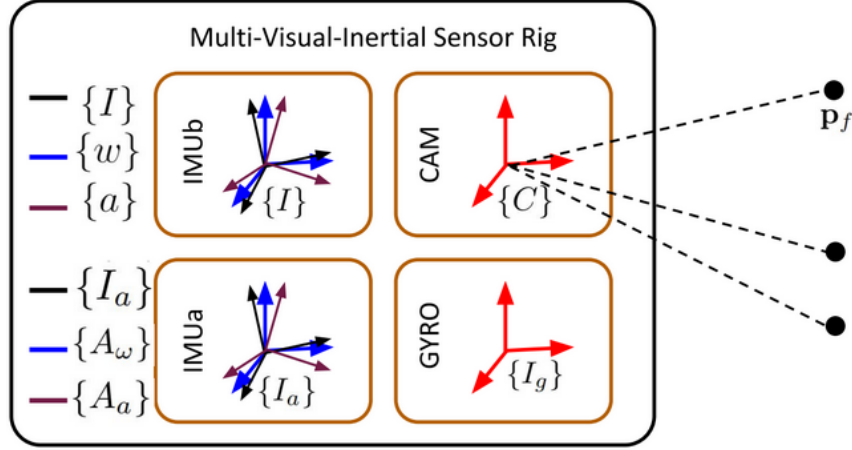


Figure 1: The MVIS sensor frames: base IMU (IMUb) sensor composed of accelerometer frame $\{a\}$ and gyroscope $\{w\}$, base “inertial” frame $\{I\}$ is determined to coincide with gyroscope frame $\{w\}$ or accelerometer frame $\{a\}$, auxiliary IMU (IMUa) $\{I_a\}$, auxiliary gyroscope (GYRO) $\{I_g\}$, and camera (CAM) $\{C\}$ frames. $\{A_w\}$ and $\{A_a\}$ represent the gyroscope and accelerometer frames of the auxiliary IMU. While an IMU can read both angular velocities and linear acceleration, a gyroscope (GYRO) can only read angular velocities. The system observes environmental landmarks \mathbf{p}_f through its cameras. The system can contain arbitrary amounts of sensors.

because it is small enough to be insignificant for MEMS IMUs or the pre-applied factory-calibrated values in the IMU drivers are good enough. Therefore, we safely assume that the origin of the $\{w\}$ frame and $\{a\}$ coincides and ${}^a\mathbf{p}_w$ is not estimated in this paper. We use 6 parameters (indexed column-wise upper/lower triangular matrix) to describe the \mathbf{T}_w and \mathbf{T}_a while \mathbf{T}_g remains a 3×3 full matrix. \mathbf{b}_g and \mathbf{b}_a are the gyroscope and accelerometer biases, which are both modeled as random walks, and \mathbf{n}_g and \mathbf{n}_a are the zero-mean Gaussian noises contaminating the measurements. The corrected angular velocity ${}^I\boldsymbol{\omega}$ and linear acceleration ${}^I\mathbf{a}$ are thus defined as:

$${}^I\boldsymbol{\omega} = {}_w^I\mathbf{R}\mathbf{D}_w ({}^w\boldsymbol{\omega}_m - \mathbf{b}_g - \mathbf{n}_g - \mathbf{T}_g {}^I\mathbf{a}) \quad (3)$$

$${}^I\mathbf{a} = {}_a^I\mathbf{R}\mathbf{D}_a ({}^a\mathbf{a}_m - \mathbf{b}_a - \mathbf{n}_a) \quad (4)$$

where $\mathbf{D}_w = \mathbf{T}_w^{-1}$ and $\mathbf{D}_a = \mathbf{T}_a^{-1}$. In practice, we consider two models in this paper: RPNG model and Kalibr model¹.

- RPNG model: \mathbf{T}_g , ${}_a^I\mathbf{R}$ and \mathbf{D}_* . \mathbf{D}_* is in upper triangular matrix form as:

$$\mathbf{D}_* = \begin{bmatrix} d_{*1} & d_{*2} & d_{*4} \\ 0 & d_{*3} & d_{*5} \\ 0 & 0 & d_{*6} \end{bmatrix} \quad (5)$$

- Kalibr model: \mathbf{T}_g , ${}_w^I\mathbf{R}$ and \mathbf{D}'_* . \mathbf{D}'_* is in lower triangular matrix form as:

$$\mathbf{D}'_* = \begin{bmatrix} d_{*1} & 0 & 0 \\ d_{*2} & d_{*4} & 0 \\ d_{*3} & d_{*5} & d_{*6} \end{bmatrix} \quad (6)$$

Note that the subscript * denotes either w or a . The Kalibr model is used to compare with Kalibr [21] and benefits from assuming the inertial frame to aligned with the accelerometer, since

¹<https://github.com/ethz-asl/kalibr/wiki/Multi-IMU-and-IMU-intrinsic-calibration>

the translation between $\{w\}$ and $\{a\}$ can be always ignored. In the remaining of our analysis the RPNG model will be used as example.

3.2 Camera Model

Cameras follow a pinhole model as in [6, 8]. A 3D point feature, ${}^G\mathbf{p}_f$, is captured by a camera with visual measurement function:

$$\mathbf{z}_C = [u \ v]^\top + \mathbf{n}_C \quad (7)$$

$$\triangleq \mathbf{h}_d(\mathbf{z}_n, \mathbf{x}_{C_{in}}) + \mathbf{n}_C \quad (8)$$

$$\begin{bmatrix} u \\ v \end{bmatrix} = \mathbf{h}_d(\mathbf{z}_n, \mathbf{x}_{C_{in}}) \quad (9)$$

where $\{u, v\}$ is the distorted image pixel coordinate; $\mathbf{z}_n = [u_n \ v_n]^\top$ represents the normalized image pixel; \mathbf{n}_C denotes the measurement noise; $\mathbf{h}_d(\cdot)$ maps the normalized image pixel onto the image plane based on the lens distortion models and camera intrinsic parameters $\mathbf{x}_{C_{in}}$:

$$\mathbf{x}_{C_{in}} = [f_u \ f_v \ c_u \ c_v \ k_1 \ k_2 \ p_1 \ p_2]^\top \quad (10)$$

Specifically, $\mathbf{x}_{C_{in}}$ can represent a pinhole model ($\{f_u, f_v\}$ denotes focal length and $\{c_u, c_v\}$ the center point) with radial-tangential (**radtan**) or equivalent-distant (**equidist**) distortion.

For **radtan** distortion model, k_1 and k_2 represent the radial distortion coefficients while p_1 and p_2 are tangential distortion coefficients. We refer the reader to [35, 6] for details on the **equidist** distortion model. Note that the **radtan** model is used in the following derivations and analysis. With $\mathbf{x}_{C_{in}}$, $\mathbf{h}_d(\cdot)$, the **radtan** model is given by:

$$\begin{bmatrix} u \\ v \end{bmatrix} = \begin{bmatrix} f_u & 0 \\ 0 & f_v \end{bmatrix} \begin{bmatrix} u_d \\ v_d \end{bmatrix} + \begin{bmatrix} c_u \\ c_v \end{bmatrix} \quad (11)$$

$$\begin{bmatrix} u_d \\ v_d \end{bmatrix} = \begin{bmatrix} du_n + 2p_1u_nv_n + p_2(r^2 + 2u_n^2) \\ dv_n + p_1(r^2 + 2v_n^2) + 2p_2u_nv_n \end{bmatrix} \quad (12)$$

where $r^2 = u_n^2 + v_n^2$; $d = 1 + k_1r^2 + k_2r^4$;

GS cameras expose all pixels at a single time instance, while RS cameras expose each row sequentially. As shown by [36], it may lead to large estimation errors if RS effects are not taken into account. Additionally, the camera and IMU measurement timestamps can be incorrect due to processing delays, or different clock references. To address this, we model both the time offset and camera readout time to ensure all measurements are processed in a common clock frame of reference and at the correct corresponding poses. Specifically, t_d denotes the time offset between IMU and camera timeline while t_r denotes the constant RS readout time for the whole image. If t denotes the time when the pixel is captured, the RS measurement function for a normalized image pixel \mathbf{z}_n is given by:

$$\mathbf{z}_n = \mathbf{h}_p({}^{C(t)}\mathbf{p}_f) \triangleq \frac{1}{{}^Cz_f} \begin{bmatrix} {}^Cx_f \\ {}^Cy_f \end{bmatrix} \quad (13)$$

$$\begin{aligned} {}^{C(t)}\mathbf{p}_f &= \mathbf{h}_t({}^G\mathbf{R}, {}^G\mathbf{p}_{I(t)}, {}^I\mathbf{R}, {}^C\mathbf{p}_I, {}^G\mathbf{p}_f) \\ &\triangleq {}^I\mathbf{R}_G^{I(t)}\mathbf{R}({}^G\mathbf{p}_f - {}^G\mathbf{p}_{I(t)}) + {}^C\mathbf{p}_I \end{aligned} \quad (14)$$

where $\{{}_I^C \mathbf{R}, {}_I^C \mathbf{p}_I\}$ represents the rigid transformation between the IMU and camera frame. As usual, $\{{}_I^G \mathbf{R}, {}_I^G \mathbf{p}_{I(t)}\}$ is the IMU global pose corresponding to the camera measurement time t .

If the image pixel \mathbf{z}_C , Eq. (7), is captured in the m -th row (out of total M rows), and t_I is the IMU state time corresponding to the captured image time t_C when the first row of the image is collected, the relationship between t_I , t_C , t_d and t_r are expressed as:

$$t_I = t_C + t_d \quad (15)$$

$$t = t_I + \frac{m}{M} t_r \quad (16)$$

If the readout time $t_r = 0$, then the camera is actually a GS camera and all rows are a function of the same pose.

3.3 State Vector

The proposed MVIS can support any number of IMUs and cameras. For simplicity of presentation, we only consider one representative sensor (one base IMU, one auxiliary IMU, one auxiliary gyroscope and one RS camera) of each types in the state vector. Both simulation and real world experiments use multiple auxiliary IMUs/gyroscopes and cameras.

The state vector of MVIS contains the base IMU states \mathcal{X}_I , the auxiliary IMU states \mathcal{X}_{I_a} and the auxiliary gyroscope states \mathcal{X}_{I_g} from time stamp 1 to k . Additionally, it also contains all the sensor intrinsics \mathcal{X}_{In} , spatiotemporal extrinsics \mathcal{X}_{Ex} , and environmental features \mathcal{X}_F .

$$\mathcal{X} = \left[\mathcal{X}_I^\top \quad \mathcal{X}_{I_a}^\top \quad \mathcal{X}_{I_g}^\top \quad \mathcal{X}_{In}^\top \quad \mathcal{X}_{Ex}^\top \quad \mathcal{X}_F^\top \right]^\top \quad (17)$$

$$\mathcal{X}_I = \left[\mathbf{x}_{I_1}^\top \quad \mathbf{x}_{I_2}^\top \quad \cdots \quad \mathbf{x}_{I_k}^\top \right]^\top \quad (18)$$

$$\mathcal{X}_{I_a} = \left[\mathbf{x}_{I_{a1}}^\top \quad \mathbf{x}_{I_{a2}}^\top \quad \cdots \quad \mathbf{x}_{I_{ak}}^\top \right]^\top \quad (19)$$

$$\mathcal{X}_{I_g} = \left[\mathbf{x}_{I_{g1}}^\top \quad \mathbf{x}_{I_{g2}}^\top \quad \cdots \quad \mathbf{x}_{I_{gk}}^\top \right]^\top \quad (20)$$

where \mathcal{X}_F contains 3D feature positions ${}^G \mathbf{p}_{f_i}$ ($i = 1, \dots, l$):

$$\mathcal{X}_F = [{}^G \mathbf{p}_{f_1}^\top \dots {}^G \mathbf{p}_{f_l}^\top]^\top \quad (21)$$

The sub-states \mathbf{x}_I , \mathbf{x}_{I_a} and \mathbf{x}_{I_g} denote the base IMU state, auxiliary IMU state and auxiliary gyroscope state, respectively. They contain the following:

$$\mathbf{x}_I = [\mathbf{x}_{nav}^\top \mid \mathbf{x}_b^\top]^\top \quad (22)$$

$$\triangleq [{}_I^G \boldsymbol{\theta}^\top \ {}^G \mathbf{p}_I^\top \ {}^G \mathbf{v}_I^\top \mid \mathbf{b}_g^\top \ \mathbf{b}_a^\top]^\top \quad (23)$$

$$\mathbf{x}_{I_a} = [{}^G \mathbf{v}_{I_a}^\top \mid \mathbf{x}_{A_b}^\top]^\top \quad (24)$$

$$\triangleq [{}^G \mathbf{v}_{I_a}^\top \mid \mathbf{b}_{A_g}^\top \ \mathbf{b}_{A_a}^\top]^\top \quad (25)$$

$$\mathbf{x}_{I_g} = \mathbf{b}_{G_g} \quad (26)$$

where \mathbf{x}_I contains IMU navigation state \mathbf{x}_{nav} and bias state \mathbf{x}_b ; ${}_I^G \boldsymbol{\theta}$ (${}_I^G \boldsymbol{\theta}$) is 3D angle-axis vector corresponding to the rotation ${}_I^G \mathbf{R}$ (${}_I^G \mathbf{R}$) from the base (auxiliary) IMU frame to global frame $\{G\}$. Note that ${}_I^G \boldsymbol{\theta} = \log({}_I^G \mathbf{R})$ with $\log(\cdot)$ defined as the log of $\mathcal{SO}(3)$ [37]. ${}^G \mathbf{p}_I$ (${}^G \mathbf{p}_{I_a}$) and ${}^G \mathbf{v}_I$ (${}^G \mathbf{v}_{I_a}$) represent the global position and velocity of base (auxiliary) IMU in $\{G\}$. \mathbf{b}_g and \mathbf{b}_a denote the

Table 1: The full-calibration parameters in the proposed MVIS.

Sensor	Extrinsics	Temporal	Intrinsics	Qty
Base IMU	—	—	\mathbf{x}_{in}	1
Aux IMU	${}^I_{I_a} \mathbf{R}, {}^I \mathbf{p}_{I_a}$	t_{da}	$\mathbf{x}_{A_{in}}$	≥ 1
Aux Gyro	${}^I_{I_g} \mathbf{R}$	t_{dg}	$\mathbf{x}_{G_{in}}$	≥ 1
Camera	${}^I_C \mathbf{R}, {}^I \mathbf{p}_C$	t_d, t_r	$\mathbf{x}_{C_{in}}$	≥ 1

gyroscope and accelerometer bias for base IMU, respectively. \mathbf{b}_{A_g} and \mathbf{b}_{A_a} denote the gyroscope and accelerometer bias for auxiliary IMU, respectively. \mathbf{b}_{G_g} denotes the gyroscope bias for auxiliary gyroscope. We did not keep a full navigation state for auxiliary IMU/gyroscope since the poses can be recovered by the rigid body transform from the base IMU. Note that IMU state \mathbf{x}_I is created based on IMU frame corresponding to the camera image time.

\mathcal{X}_{In} contains base IMU intrinsics \mathbf{x}_{in} , auxiliary IMU intrinsics $\mathbf{x}_{A_{in}}$, auxiliary gyroscope intrinsics $\mathbf{x}_{G_{in}}$ and camera intrinsics $\mathbf{x}_{C_{in}}$:

$$\mathcal{X}_{In} = [\mathbf{x}_{in}^\top \quad \mathbf{x}_{A_{in}}^\top \quad \mathbf{x}_{G_{in}}^\top \quad \mathbf{x}_{C_{in}}^\top]^\top \quad (27)$$

$$\mathbf{x}_{in} = [\mathbf{x}_w^\top \quad \mathbf{x}_a^\top \quad \mathbf{x}_{T_g}^\top \quad {}^I_a \boldsymbol{\theta}^\top]^\top \quad (28)$$

$$\mathbf{x}_{A_{in}} = [\mathbf{x}_{A_w}^\top \quad \mathbf{x}_{A_a}^\top \quad \mathbf{x}_{A_g}^\top \quad {}^I_a \boldsymbol{\theta}^\top]^\top \quad (29)$$

$$\mathbf{x}_{G_{in}} = \mathbf{x}_{G_w} \quad (30)$$

where \mathbf{x}_w (\mathbf{x}_{A_w}), \mathbf{x}_a (\mathbf{x}_{A_a}) contains all the 6 column-wise parameters from \mathbf{D}_w and \mathbf{D}_a for base (auxiliary) IMU, respectively. \mathbf{x}_{T_g} (\mathbf{x}_{A_g}) contains all the 9 parameters for \mathbf{T}_g and \mathbf{T}_{A_g} from base (auxiliary) IMU, respectively. ${}^I_a \boldsymbol{\theta}$ (${}^I_a \boldsymbol{\theta}$) denotes the rotation from the accelerometer frame to the base (auxiliary) IMU frame. \mathbf{x}_{G_w} denotes the 6 column-wise parameters from \mathbf{D}_w for auxiliary gyroscope.

\mathcal{X}_{Ex} contains the spatiotemporal calibrations for base IMU to auxiliary IMU \mathbf{x}_{I_A} , base IMU to auxiliary gyroscope \mathbf{x}_{I_G} and base IMU to camera \mathbf{x}_{I_C} , respectively:

$$\mathcal{X}_{Ex} = [\mathbf{x}_{I_A}^\top \quad \mathbf{x}_{I_G}^\top \quad \mathbf{x}_{I_C}^\top]^\top \quad (31)$$

$$\mathbf{x}_{I_A} = [{}^I_{I_a} \boldsymbol{\theta}^\top \quad {}^I \mathbf{p}_{I_a}^\top \quad t_{da}]^\top \quad (32)$$

$$\mathbf{x}_{I_G} = [{}^I_{I_g} \boldsymbol{\theta}^\top \quad t_{dg}]^\top \quad (33)$$

$$\mathbf{x}_{I_C} = [{}^I_C \boldsymbol{\theta}^\top \quad {}^I \mathbf{p}_C^\top \quad t_d \quad t_r]^\top \quad (34)$$

Note that time offset between auxiliary IMU and base IMU is defined as: $t_{da} = t_a - t_I$, where t_a and t_I represent the auxiliary and base IMU measurement time, respectively. The IMU-Gyroscope time offset t_{dg} and IMU-Camera time offset t_d are defined in a similar way as t_{da} . t_r denotes the whole image reading out time for the RS camera . Note that all the calibration parameters are summarized in Table 1.

3.4 NLS Formulation

Given measurements \mathbf{z}_S from a sensor S , with additive white Gaussian noise \mathbf{n}_S , we have:

$$\mathbf{z}_S = \mathbf{h}_S(\mathbf{x}) + \mathbf{n}_S, \quad \mathbf{n}_S \sim \mathcal{N}(\mathbf{0}, \mathbf{R}_S) \quad (35)$$

where $\mathbf{h}_S(\cdot)$ denotes the nonlinear observation function. Then, we can formulate the NLS problem with state \mathbf{x} as :

$$\min_{\mathbf{x}} \sum \| \mathbf{z}_S - \mathbf{h}_S(\mathbf{x}) \|_{\mathbf{R}_S^{-1}}^2 \quad (36)$$

An initial guess $\hat{\mathbf{x}}^\ominus$ is needed to start the optimization. After computing the incremental state correction $\delta\mathbf{x}$, we can refine the state estimates by $\hat{\mathbf{x}}^\oplus = \hat{\mathbf{x}}^\ominus \boxplus \delta\mathbf{x}$, where \boxplus represents the state manifold update [37]. In summary, we have the following NLS equivalent to maximum likelihood estimation (MLE) under some common assumptions:

$$\min_{\mathbf{x}} \sum \mathbb{C}_I + \sum \mathbb{C}_{I_a} + \sum \mathbb{C}_{I_g} + \sum \mathbb{C}_C \quad (37)$$

where \mathbb{C}_I , \mathbb{C}_{I_a} , \mathbb{C}_{I_g} and \mathbb{C}_C denotes the cost for base IMU, auxiliary IMUs, auxiliary gyroscopes, and cameras, respectively, and will be built explicitly later. The NLS from Eq. (37) can be solved through various nonlinear least squares solvers [e.g. IPOPT [38], g2o solver [39], GTSAM [40], Google Ceres [41]] and yields the optimal IMU states, point features, and full-calibration parameters [see (17)]. In this paper, the GTSAM is selected to implement the algorithms for evaluations since GTSAM can achieve comparable accuracy to other solvers [42], but this should not stop interested readers from applying the above NLS formulation to other solvers.

4 ACI³: Preintegration with Intrinsics

In this section, we extend our analytic combined IMU integration (ACI²) [26] to incorporate IMU intrinsics into preintegration, and propose an efficient IMU integrator that can be leveraged for IMU intrinsic calibration.

The IMU dynamic model is given by [43, 44]:

$${}^G\dot{\mathbf{R}} = {}^G\mathbf{R} \cdot [\mathbf{I}^I\boldsymbol{\omega}] \quad (38)$$

$${}^G\dot{\mathbf{p}}_I = {}^G\mathbf{v}_I \quad (39)$$

$${}^G\dot{\mathbf{v}}_I = {}^G\mathbf{R}^I \mathbf{a} + {}^G\mathbf{g} \quad (40)$$

$${}^I\dot{\mathbf{b}}_g = \mathbf{n}_{wg}, \quad (41)$$

$${}^I\dot{\mathbf{b}}_a = \mathbf{n}_{wa}$$

where ${}^G\mathbf{g} = [0 \ 0 \ -9.81]^\top$, \mathbf{n}_{wg} and \mathbf{n}_{wa} are the white Gaussian noises driving the gyroscope and accelerometer biases. ${}^I\boldsymbol{\omega} = [{}^I\omega_x \ {}^I\omega_y \ {}^I\omega_z]^\top$ and $[\mathbf{I}^I\boldsymbol{\omega}] = \begin{bmatrix} 0 & -{}^I\omega_z & {}^I\omega_y \\ {}^I\omega_z & 0 & -{}^I\omega_x \\ -{}^I\omega_y & {}^I\omega_x & 0 \end{bmatrix}$ represents a skew symmetric matrix [43]. We also denote $\hat{\mathbf{x}}$ as estimate of \mathbf{x} while $\tilde{\mathbf{x}}$ as error states between \mathbf{x} and $\hat{\mathbf{x}}$, i.e., $\tilde{\mathbf{x}} = \mathbf{x} \boxminus \hat{\mathbf{x}}$. As [4, 45], the IMU pose is represented as $\mathcal{SO}(3) \times \mathbb{R}^3$ with error states defined as:

$$\mathbf{R} = \hat{\mathbf{R}} \exp(\delta\boldsymbol{\theta}) \quad (42)$$

$$\mathbf{p} = \hat{\mathbf{p}} + \tilde{\mathbf{p}} \quad (43)$$

where $\exp(\delta\boldsymbol{\theta}) \simeq \mathbf{I}_3 + [\delta\boldsymbol{\theta}]$ and $\delta\boldsymbol{\theta}$ is assumed to be small angles; $\exp(\cdot)$ denotes the exponential operation of $\mathcal{SO}(3)$ [37].

4.1 Pre-integration Terms

Between two sampling times t_k and t_j , we integrate the IMU dynamic model as follows:

$${}_{I_j}^G \mathbf{R} = {}_{I_k}^G \mathbf{R} \cdot \Delta \mathbf{R} \quad (44)$$

$${}^G \mathbf{p}_{I_j} = {}^G \mathbf{p}_{I_k} + {}^G \mathbf{v}_{I_k} \delta t_k + {}_{I_k}^G \mathbf{R} \Delta \mathbf{p} + \frac{1}{2} {}^G \mathbf{g} \delta t_k^2 \quad (45)$$

$${}^G \mathbf{v}_{I_j} = {}^G \mathbf{v}_{I_k} + {}_{I_k}^G \mathbf{R} \Delta \mathbf{v} + {}^G \mathbf{g} \delta t_k \quad (46)$$

$$\mathbf{b}_{g_j} = \mathbf{b}_{g_k} + \Delta \mathbf{b}_g \quad (47)$$

$$\mathbf{b}_{a_j} = \mathbf{b}_{a_k} + \Delta \mathbf{b}_a \quad (48)$$

where $\delta t = t_j - t_k$, while $\Delta \mathbf{R}$, $\Delta \mathbf{p}$, $\Delta \mathbf{v}$, $\Delta \mathbf{b}_g$, and $\Delta \mathbf{b}_a$ are the IMU pre-integration terms from t_k to t_j , described by:

$$\Delta \mathbf{R} \triangleq \exp \left(\int_{t_k}^{t_j} {}_{I_\tau}^G \boldsymbol{\omega} d\tau \right) = \mathbf{h}_R(\mathbf{x}_{I_k}, \mathbf{x}_{I_j}) \quad (49)$$

$$\Delta \mathbf{p} \triangleq \int_{t_k}^{t_j} \int_{t_k}^s {}_{I_\tau}^G \mathbf{R}^T \mathbf{a} d\tau ds = \mathbf{h}_p(\mathbf{x}_{I_k}, \mathbf{x}_{I_j}) \quad (50)$$

$$\Delta \mathbf{v} \triangleq \int_{t_k}^{t_j} {}_{I_\tau}^G \mathbf{R}^T \mathbf{a} d\tau = \mathbf{h}_v(\mathbf{x}_{I_k}, \mathbf{x}_{I_j}) \quad (51)$$

$$\Delta \mathbf{b}_g \triangleq \int_{t_k}^{t_j} \mathbf{n}_{wg} d\tau = \mathbf{b}_{g_j} - \mathbf{b}_{g_k} \quad (52)$$

$$\Delta \mathbf{b}_a \triangleq \int_{t_k}^{t_j} \mathbf{n}_{wg} d\tau = \mathbf{b}_{a_j} - \mathbf{b}_{a_k} \quad (53)$$

where we have defined:

$$\mathbf{h}_R(\mathbf{x}_{I_k}, \mathbf{x}_{I_j}) \triangleq {}_{I_k}^G \mathbf{R}^T {}_{I_j}^G \mathbf{R} \quad (54)$$

$$\mathbf{h}_p(\mathbf{x}_{I_k}, \mathbf{x}_{I_j}) \triangleq {}_{I_k}^G \mathbf{R}^T \left({}^G \mathbf{p}_{I_j} - {}^G \mathbf{p}_{I_k} - {}^G \mathbf{v}_{I_k} \delta t - \frac{1}{2} {}^G \mathbf{g} \delta t^2 \right) \quad (55)$$

$$\mathbf{h}_v(\mathbf{x}_{I_k}, \mathbf{x}_{I_j}) \triangleq {}_{I_k}^G \mathbf{R}^T \left({}^G \mathbf{v}_{I_j} - {}^G \mathbf{v}_{I_k} - {}^G \mathbf{g} \delta t \right) \quad (56)$$

In the following, the proposed ACI³ recursively computes the mean and covariance of these pre-integrated terms (i.e. $\Delta \mathbf{R}$, $\Delta \mathbf{p}$, $\Delta \mathbf{v}$, $\Delta \mathbf{b}_g$ and $\Delta \mathbf{b}_a$) with intrinsics \mathbf{x}_{in} .

4.2 Recursive Formulation

Assuming there are $j - k + 1$ IMU readings between the timestamps k and j , there exists an integer i such that: $k \leq k + i < k + i + 1 \leq j$. $\Delta \mathbf{R}_i$, $\Delta \mathbf{p}_i$, $\Delta \mathbf{v}_i$, $\Delta \mathbf{b}_{gi}$ and $\Delta \mathbf{b}_{ai}$ denote the integration

components using all IMU readings from time t_k to t_{k+i} :

$$\Delta \mathbf{R}_i = \exp\left(\int_{t_k}^{t_{k+i}} I_\tau \boldsymbol{\omega} d\tau\right) \quad (57)$$

$$\Delta \mathbf{p}_i = \int_{t_k}^{t_{k+i}} \int_{t_k}^s I_\tau \mathbf{R}^{I_\tau} \mathbf{a} d\tau ds \quad (58)$$

$$\Delta \mathbf{v}_i = \int_{t_k}^{t_{k+i}} I_\tau \mathbf{R}^{I_\tau} \mathbf{a} d\tau \quad (59)$$

$$\Delta \mathbf{b}_{gi} = \mathbf{b}_{g_{k+i}} - \mathbf{b}_{g_k} \quad (60)$$

$$\Delta \mathbf{b}_{ai} = \mathbf{b}_{a_{k+i}} - \mathbf{b}_{a_k} \quad (61)$$

With that, we compute the pre-integration in the following recursive form:

$$\Delta \mathbf{R}_{i+1} = \Delta \mathbf{R}_i \cdot \mathbf{R}_{i,i+1} \quad (62)$$

$$\Delta \mathbf{p}_{i+1} = \Delta \mathbf{p}_i + \Delta \mathbf{v}_i \delta t_i + \Delta \mathbf{R}_i \cdot \mathbf{p}_{i,i+1} \quad (63)$$

$$\Delta \mathbf{v}_{i+1} = \Delta \mathbf{v}_i + \Delta \mathbf{R}_i \cdot \mathbf{v}_{i,i+1} \quad (64)$$

$$\Delta \mathbf{b}_{gi+1} = \Delta \mathbf{b}_{gi} + \mathbf{b}_{gi,i+1} \quad (65)$$

$$\Delta \mathbf{b}_{ai+1} = \Delta \mathbf{b}_{ai} + \mathbf{b}_{ai,i+1} \quad (66)$$

where the increments are defined as:

$$\mathbf{R}_{i,i+1} \triangleq \int_{t_{k+i}}^{t_{k+i+1}} I_\tau \boldsymbol{\omega} d\tau \quad (67)$$

$$\mathbf{p}_{i,i+1} \triangleq \int_{t_{k+i}}^{t_{k+i+1}} \int_{t_{k+i}}^s I_\tau \mathbf{R}^{I_\tau} \mathbf{a} d\tau ds \quad (68)$$

$$\mathbf{v}_{i,i+1} \triangleq \int_{t_{k+i}}^{t_{k+i+1}} I_\tau \mathbf{R}^{I_\tau} \mathbf{a} d\tau \quad (69)$$

$$\mathbf{b}_{gi,i+1} \triangleq \int_{t_{k+i}}^{t_{k+i+1}} \mathbf{n}_{wg} d\tau \quad (70)$$

$$\mathbf{b}_{ai,i+1} \triangleq \int_{t_{k+i}}^{t_{k+i+1}} \mathbf{n}_{wa} d\tau \quad (71)$$

By applying Eq. (62)-(66) to all the IMU readings from t_k to t_j , we can compute both the mean and covariance of the IMU pre-integration terms (i.e. $\Delta \mathbf{R}$, $\Delta \mathbf{p}$, $\Delta \mathbf{v}$, $\Delta \mathbf{b}_g$ and $\Delta \mathbf{b}_a$), as shown in the following sections.

4.3 Mean Prediction

To simplify the ensuing derivations, we rewrite the IMU readings $\boldsymbol{\omega}_{k+i}$ and \mathbf{a}_{k+i} as:

$$\begin{aligned} \boldsymbol{\omega}_{k+i} &= {}^I_w \mathbf{R} \mathbf{D}_w ({}^w \boldsymbol{\omega}_{m_{k+i}} - \mathbf{T}_g \mathbf{a}_{k+i} - \mathbf{b}_{g_{k+i}} - \mathbf{n}_{g_{k+i}}) \\ &= {}^I_w \mathbf{R} \mathbf{D}_w ({}^w \boldsymbol{\omega}_{m_{k+i}} - \mathbf{b}_{g_{k+i}} - \mathbf{n}_{g_{k+i}} - \mathbf{T}_g \mathbf{a}_{k+i}) \\ &= {}^I_w \mathbf{R} \mathbf{D}_w ({}^w \boldsymbol{\omega}_{m_{k+i}} - \Delta \mathbf{b}_{gi} - \mathbf{b}_{g_k} - \mathbf{n}_{g_{k+i}} - \mathbf{T}_g \mathbf{a}_{k+i}) \\ \mathbf{a}_{k+i} &= {}^I_a \mathbf{R} \mathbf{D}_a ({}^a \mathbf{a}_{m_{k+i}} - \mathbf{b}_{a_{k+i}} - \mathbf{n}_{a_{k+i}}) \\ &= {}^I_a \mathbf{R} \mathbf{D}_a ({}^a \mathbf{a}_{m_{k+i}} - \Delta \mathbf{b}_{ai} - \mathbf{b}_{a_k} - \mathbf{n}_{a_{k+i}}) \end{aligned}$$

Note that the ω_{k+i} and \mathbf{a}_{k+i} are actually function of \mathbf{x}_{in} and \mathbf{x}_{b_k} . The angular velocity and linear acceleration can be written as:

$$\omega_{k+i} = \hat{\omega}_{k+i} + \tilde{\omega}_{k+i} \quad (72)$$

$$\mathbf{a}_{k+i} = \hat{\mathbf{a}}_{k+i} + \tilde{\mathbf{a}}_{k+i} \quad (73)$$

With bias terms defined in Eq. (60) and (61), $\hat{\omega}_{k+i}$ and $\hat{\mathbf{a}}_{k+i}$ are computed as [see Eq. (3) and (4)]:

$$\hat{\omega}_{k+i} = {}_w^I \hat{\mathbf{R}} \hat{\mathbf{D}}_w \left({}^w \omega_{m_{k+i}} - \Delta \hat{\mathbf{b}}_{gi} - \hat{\mathbf{b}}_{g_k} - \hat{\mathbf{T}}_g \hat{\mathbf{a}}_{k+i} \right) \quad (74)$$

$$\hat{\mathbf{a}}_{k+i} = {}_a^I \hat{\mathbf{R}} \hat{\mathbf{D}}_a \left({}^a \mathbf{a}_{m_{k+i}} - \Delta \hat{\mathbf{b}}_{ai} - \hat{\mathbf{b}}_{a_k} \right) \quad (75)$$

Let's then define the error states for the ω_{k+i} and \mathbf{a}_{k+i} as:

$$\begin{aligned} \tilde{\mathbf{a}}_{k+i} &= {}_a^I \mathbf{R} \mathbf{H}_{Da} \tilde{\mathbf{x}}_{Da} - [\hat{\mathbf{a}}_{k+i}] {}_a^I \mathbf{R} \delta \boldsymbol{\theta}_{Ia} - {}_a^I \mathbf{R} \mathbf{D}_a \left(\tilde{\mathbf{b}}_{a_k} + \Delta \tilde{\mathbf{b}}_{ai} + \mathbf{n}_{a_{k+i}} \right) \\ \tilde{\omega}_{k+i} &= {}_w^I \hat{\mathbf{R}} \mathbf{H}_{Dw} \tilde{\mathbf{x}}_{Dw} - {}_w^I \mathbf{R} \mathbf{D}_w \mathbf{T}_{ga} {}_w^I \mathbf{R} \mathbf{H}_{Da} \tilde{\mathbf{x}}_{Da} - [\hat{\omega}_{k+i}] {}_w^I \mathbf{R} \delta \boldsymbol{\theta}_{Iw} + {}_w^I \mathbf{R} \mathbf{D}_w \mathbf{T}_g [\hat{\mathbf{a}}_{k+i}] {}_a^I \mathbf{R} \delta \boldsymbol{\theta}_{Ia} \\ &\quad - {}_w^I \mathbf{R} \mathbf{D}_w \mathbf{H}_{Tg} \tilde{\mathbf{x}}_{Tg} - {}_w^I \mathbf{R} \mathbf{D}_w \left(\tilde{\mathbf{b}}_{g_k} + \Delta \tilde{\mathbf{b}}_{gi} + \mathbf{n}_{g_{k+i}} - \mathbf{T}_{ga} {}_w^I \mathbf{R} \mathbf{D}_a \left(\tilde{\mathbf{b}}_{a_k} + \Delta \tilde{\mathbf{b}}_{ai} + \mathbf{n}_{a_{k+i}} \right) \right) \end{aligned}$$

Hence, we can have:

$$\begin{bmatrix} \tilde{\omega}_{k+i} \\ \tilde{\mathbf{a}}_{k+i} \end{bmatrix} \triangleq \mathbf{H}_b^{wa} \begin{bmatrix} \Delta \tilde{\mathbf{b}}_{gi} \\ \Delta \tilde{\mathbf{b}}_{ai} \end{bmatrix} + \mathbf{H}_{b_k}^{wa} \begin{bmatrix} \tilde{\mathbf{b}}_{g_k} \\ \tilde{\mathbf{b}}_{a_k} \end{bmatrix} + \mathbf{H}_{in}^{wa} \begin{bmatrix} \tilde{\mathbf{x}}_{Dw} \\ \tilde{\mathbf{x}}_{Da} \\ \tilde{\mathbf{x}}_{Tg} \\ \delta \boldsymbol{\theta}_{Iw} \\ \delta \boldsymbol{\theta}_{Ia} \end{bmatrix} + \mathbf{H}_n^{wa} \begin{bmatrix} \mathbf{n}_{g_{k+i}} \\ \mathbf{n}_{a_{k+i}} \end{bmatrix} \quad (76)$$

with:

$$\mathbf{H}_b^{wa} = \begin{bmatrix} {}_w^I \mathbf{R} \mathbf{D}_w & {}_w^I \mathbf{R} \mathbf{D}_w \mathbf{T}_{ga} {}_w^I \mathbf{R} \mathbf{D}_a \\ \mathbf{0}_3 & -{}_a^I \mathbf{R} \mathbf{D}_a \end{bmatrix} \quad (77)$$

$$\mathbf{H}_{b_k}^{wa} = \begin{bmatrix} {}_w^I \mathbf{R} \mathbf{D}_w & {}_w^I \mathbf{R} \mathbf{D}_w \mathbf{T}_{ga} {}_w^I \mathbf{R} \mathbf{D}_a \\ \mathbf{0}_3 & -{}_a^I \mathbf{R} \mathbf{D}_a \end{bmatrix} \quad (78)$$

$$\mathbf{H}_n^{wa} = \begin{bmatrix} {}_w^I \mathbf{R} \mathbf{D}_w & {}_w^I \mathbf{R} \mathbf{D}_w \mathbf{T}_{ga} {}_w^I \mathbf{R} \mathbf{D}_a \\ \mathbf{0}_3 & -{}_a^I \mathbf{R} \mathbf{D}_a \end{bmatrix} \quad (79)$$

$$\mathbf{H}_{in} = [\mathbf{H}_{xw} \quad \mathbf{H}_{xa} \quad \mathbf{H}_{gs} \quad \mathbf{H}_{Iw} \quad \mathbf{H}_{Ia}] \quad (80)$$

$$\mathbf{H}_{xw} = \begin{bmatrix} {}_w^I \hat{\mathbf{R}} \mathbf{H}_{Dw} \\ \mathbf{0}_3 \end{bmatrix} \quad (81)$$

$$\mathbf{H}_{xa} = \begin{bmatrix} {}_w^I \mathbf{R} \mathbf{D}_w \mathbf{T}_{ga} {}_w^I \mathbf{R} \mathbf{H}_{Da} \\ {}_a^I \mathbf{R} \mathbf{H}_{Da} \end{bmatrix} \quad (82)$$

$$\mathbf{H}_{gs} = \begin{bmatrix} {}_w^I \mathbf{R} \mathbf{D}_w \mathbf{H}_{Tg} \\ \mathbf{0}_3 \end{bmatrix} \quad (83)$$

$$\mathbf{H}_{Ia} = \begin{bmatrix} {}_w^I \mathbf{R} \mathbf{D}_w \mathbf{T}_g [\hat{\mathbf{a}}_{k+i}] {}_a^I \mathbf{R} \\ -[\hat{\mathbf{a}}_{k+i}] {}_a^I \mathbf{R} \end{bmatrix} \quad (84)$$

$$\mathbf{H}_{Iw} = \begin{bmatrix} -[\hat{\omega}_{k+i}] {}_w^I \mathbf{R} \\ \mathbf{0}_3 \end{bmatrix} \quad (85)$$

Assuming that $\hat{\omega}_{k+i}$ and $\hat{\mathbf{a}}_{k+i}$ are constant during the IMU sampling interval $[t_{k+i}, t_{k+i+1}]$, we have:

$$\hat{\mathbf{R}}_{i,i+1} = \exp(\hat{\omega}_{k+i}\delta t_i) \quad (86)$$

$$\begin{aligned} \hat{\mathbf{p}}_{i,i+1} &= \int_{t_{k+i}}^{t_{k+i+1}} \int_{t_{k+i}}^s \frac{I_{k+i}}{I_\tau} \hat{\mathbf{R}} d\tau ds \cdot \hat{\mathbf{a}}_{k+i} \\ &\triangleq \boldsymbol{\Xi}_2 \cdot \hat{\mathbf{a}}_{k+i} \end{aligned} \quad (87)$$

$$\begin{aligned} \hat{\mathbf{v}}_{i,i+1} &= \int_{t_{k+i}}^{t_{k+i+1}} \frac{I_{k+i}}{I_\tau} \hat{\mathbf{R}} d\tau \cdot \hat{\mathbf{a}}_{k+i} \\ &\triangleq \boldsymbol{\Xi}_1 \cdot \hat{\mathbf{a}}_{k+i} \end{aligned} \quad (88)$$

$$\hat{\mathbf{b}}_{gi,i+1} = \mathbf{0}_{3 \times 1} \quad (89)$$

$$\hat{\mathbf{b}}_{ai,i+1} = \mathbf{0}_{3 \times 1} \quad (90)$$

where $\boldsymbol{\Xi}_1$ and $\boldsymbol{\Xi}_2$ are defined below.

$$\boldsymbol{\Xi}_1 = \int_{t_{k+i}}^{t_{k+i+1}} \frac{I_{k+i}}{I_\tau} \hat{\mathbf{R}} d\tau \quad (91)$$

$$\boldsymbol{\Xi}_2 = \int_{t_{k+i}}^{t_{k+i+1}} \int_{t_{k+i}}^s \frac{I_{k+i}}{I_\tau} \hat{\mathbf{R}} d\tau ds \quad (92)$$

We thus recursively compute the IMU pre-integration mean:

$$\Delta \hat{\mathbf{R}}_{i+1} = \Delta \hat{\mathbf{R}}_i \cdot \hat{\mathbf{R}}_{i,i+1} \quad (93)$$

$$\Delta \hat{\mathbf{p}}_{i+1} = \Delta \hat{\mathbf{p}}_i + \Delta \hat{\mathbf{v}}_i \delta t_i + \Delta \hat{\mathbf{R}}_i \cdot \hat{\mathbf{p}}_{i,i+1} \quad (94)$$

$$\Delta \mathbf{v}_{i+1} = \Delta \hat{\mathbf{v}}_i + \Delta \hat{\mathbf{R}}_i \cdot \hat{\mathbf{v}}_{i,i+1} \quad (95)$$

$$\Delta \hat{\mathbf{b}}_{gi,i+1} = \Delta \hat{\mathbf{b}}_{gi} + \hat{\mathbf{b}}_{gi,i+1} \quad (96)$$

$$\Delta \hat{\mathbf{b}}_{ai,i+1} = \Delta \hat{\mathbf{b}}_{ai} + \hat{\mathbf{b}}_{ai,i+1} \quad (97)$$

4.4 Covariance Prediction

To compute the covariance of the preintegration measurements, we need to obtain the state transition matrix and noise Jacobians of the recursive formulation by linearizing the three preintegration terms [see Eq. (62)-(64)]. Hence, $\mathbf{R}_{i,i+1}$ from Eq. (62), can be written as:

$$\mathbf{R}_{i,i+1} \simeq \exp(\omega_{k+i}\delta t_i) \quad (98)$$

$$= \exp((\hat{\omega}_{k+i} + \tilde{\omega}_{k+i})\delta t_i) \quad (99)$$

$$= \exp(\hat{\theta}_{i,i+1}) \exp(J_r(\hat{\theta}_{i,i+1})\tilde{\omega}_{k+i}\delta t_i) \quad (100)$$

$\mathbf{p}_{i,i+1}$ from Eq. (63) can be written as:

$$\begin{aligned}
\mathbf{p}_{i,i+1} &= \int_{t_{k+i}}^{t_{k+i+1}} \int_{t_{k+i}}^s \frac{I_{k+i}}{I_\tau} \mathbf{R}^{I_\tau} \mathbf{a} d\tau ds \\
&\simeq \int_{t_{k+i}}^{t_{k+i+1}} \int_{t_{k+i}}^s \exp(\boldsymbol{\omega}_{k+i} \delta\tau) \mathbf{a}_{k+i} d\tau ds \\
&= \int_{t_{k+i}}^{t_{k+i+1}} \int_{t_{k+i}}^s \exp((\hat{\boldsymbol{\omega}}_{k+i} + \tilde{\boldsymbol{\omega}}_{k+i}) \delta\tau) (\hat{\mathbf{a}}_{k+i} + \tilde{\mathbf{a}}_{k+i}) d\tau ds \\
&\simeq \underbrace{\int_{t_{k+i}}^{t_{k+i+1}} \int_{t_{k+i}}^s \exp(\hat{\boldsymbol{\omega}}_{k+i} \delta\tau) \hat{\mathbf{a}}_{k+i} d\tau ds}_{\hat{\mathbf{p}}_{i,i+1}} \\
&\quad - \underbrace{\int_{t_{k+i}}^{t_{k+i+1}} \int_{t_{k+i}}^s \exp(\hat{\boldsymbol{\omega}}_{k+i} \delta\tau) [\hat{\mathbf{a}}_{k+i}] \mathbf{J}_r(\hat{\boldsymbol{\omega}}_{k+i} \delta\tau) \delta\tau d\tau ds}_{\Xi_4} \cdot \tilde{\boldsymbol{\omega}}_{k+i} \\
&\quad + \underbrace{\int_{t_{k+i}}^{t_{k+i+1}} \int_{t_{k+i}}^s \exp(\hat{\boldsymbol{\omega}}_{k+i} \delta\tau) d\tau ds}_{\Xi_2} \cdot \tilde{\mathbf{a}}_{k+i}
\end{aligned}$$

$\mathbf{v}_{i,i+1}$ from Eq. (64) can be written as:

$$\begin{aligned}
\mathbf{v}_{i,i+1} &= \int_{t_{k+i}}^{t_{k+i+1}} \frac{I_{k+i}}{I_\tau} \mathbf{R}^{I_\tau} \mathbf{a} d\tau \\
&\simeq \int_{t_{k+i}}^{t_{k+i+1}} \exp(\boldsymbol{\omega}_{k+i} \delta\tau) \mathbf{a}_{k+i} d\tau \\
&= \int_{t_{k+i}}^{t_{k+i+1}} \exp((\hat{\boldsymbol{\omega}}_{k+i} + \tilde{\boldsymbol{\omega}}_{k+i}) \delta\tau) (\hat{\mathbf{a}}_{k+i} + \tilde{\mathbf{a}}_{k+i}) d\tau \\
&\simeq \underbrace{\int_{t_{k+i}}^{t_{k+i+1}} \exp(\hat{\boldsymbol{\omega}}_{k+i} \delta\tau) \hat{\mathbf{a}}_{k+i} d\tau}_{\hat{\mathbf{v}}_{i,i+1}} \\
&\quad - \underbrace{\int_{t_{k+i}}^{t_{k+i+1}} \exp(\hat{\boldsymbol{\omega}}_{k+i} \delta\tau) [\hat{\mathbf{a}}_{k+i}] \mathbf{J}_r(\hat{\boldsymbol{\omega}}_{k+i} \delta\tau) \delta\tau d\tau}_{\Xi_3} \cdot \tilde{\boldsymbol{\omega}}_{k+i} \\
&\quad + \underbrace{\int_{t_{k+i}}^{t_{k+i+1}} \exp(\hat{\boldsymbol{\omega}}_{k+i} \delta\tau) d\tau}_{\Xi_1} \cdot \tilde{\mathbf{a}}_{k+i}
\end{aligned}$$

In summary, we get:

$$\mathbf{R}_{i,i+1} = \hat{\mathbf{R}}_{i,i+1} \tilde{\mathbf{R}}_{i,i+1} \quad (101)$$

$$= \hat{\mathbf{R}}_{i,i+1} \exp \left(\mathbf{J}_r(\hat{\boldsymbol{\theta}}_{i,i+1}) \tilde{\boldsymbol{\omega}}_{k+i} \delta t_i \right) \quad (102)$$

$$\mathbf{p}_{i,i+1} = \hat{\mathbf{p}}_{i,i+1} + \tilde{\mathbf{p}}_{i,i+1} \quad (103)$$

$$= \hat{\mathbf{p}}_{i,i+1} - \boldsymbol{\Xi}_4 \tilde{\boldsymbol{\omega}}_{k+i} + \boldsymbol{\Xi}_2 \tilde{\mathbf{a}}_{k+i} \quad (104)$$

$$\mathbf{v}_{i,i+1} = \hat{\mathbf{v}}_{i,i+1} + \tilde{\mathbf{v}}_{i,i+1} \quad (105)$$

$$= \hat{\mathbf{v}}_{i,i+1} - \boldsymbol{\Xi}_3 \tilde{\boldsymbol{\omega}}_{k+i} + \boldsymbol{\Xi}_1 \tilde{\mathbf{a}}_{k+i} \quad (106)$$

where $\hat{\boldsymbol{\theta}}_{i,i+1} = \hat{\boldsymbol{\omega}}_{k+i} \delta t_i$ and $\mathbf{J}_r(\hat{\boldsymbol{\theta}}_{i,i+1}) \triangleq \mathbf{J}_r(\hat{\boldsymbol{\omega}}_{k+i} \delta t_i)$ denotes the right Jacobian of $\mathcal{SO}(3)$ [46]. The integrated components $\boldsymbol{\Xi}_3$ and $\boldsymbol{\Xi}_4$ are defined as:

$$\boldsymbol{\Xi}_3 \triangleq \int_{t_{k+i}}^{t_{k+i+1}} \int_{I_\tau}^{I_{k+i}} \mathbf{R}[\hat{\mathbf{a}}_{k+i}] \mathbf{J}_r(\hat{\boldsymbol{\omega}}_{k+i} \delta \tau) \delta \tau \, d\tau \quad (107)$$

$$\boldsymbol{\Xi}_4 \triangleq \int_{t_{k+i}}^{t_{k+i+1}} \int_{I_\tau}^s \int_{t_{k+i}}^{I_{k+i}} \mathbf{R}[\hat{\mathbf{a}}_{k+i}] \mathbf{J}_r(\hat{\boldsymbol{\omega}}_{k+i} \delta \tau) \delta \tau \, d\tau ds \quad (108)$$

Note that $\boldsymbol{\Xi}_i, i = \{1 \dots 4\}$ can be evaluated analytically with detailed derivations in [34] or numerically using Runge–Kutta fourth-order (RK4) method. By summarizing the above derivations, we have:

$$\mathbf{R}_{i,i+1} = \hat{\mathbf{R}}_{i,i+1} \exp \left(\mathbf{J}_r(\hat{\boldsymbol{\theta}}_{i,i+1}) \tilde{\boldsymbol{\omega}}_{k+i} \delta t_i \right) \quad (109)$$

$$\mathbf{p}_{i,i+1} = \hat{\mathbf{p}}_{i,i+1} - \boldsymbol{\Xi}_4 \tilde{\boldsymbol{\omega}}_{k+i} + \boldsymbol{\Xi}_2 \tilde{\mathbf{a}}_{k+i} \quad (110)$$

$$\mathbf{v}_{i,i+1} = \hat{\mathbf{v}}_{i,i+1} - \boldsymbol{\Xi}_3 \tilde{\boldsymbol{\omega}}_{k+i} + \boldsymbol{\Xi}_1 \tilde{\mathbf{a}}_{k+i} \quad (111)$$

The pre-integrated errors states defined from Eq. (57) - (61):

$$\Delta \mathbf{R}_i = \Delta \hat{\mathbf{R}}_i \exp \left(\delta \Delta \boldsymbol{\theta}_i^\top \right) \quad (112)$$

$$\Delta \mathbf{p}_i = \Delta \hat{\mathbf{p}}_i + \Delta \tilde{\mathbf{p}}_i \quad (113)$$

$$\Delta \mathbf{v}_i = \Delta \hat{\mathbf{v}}_i + \Delta \tilde{\mathbf{v}}_i \quad (114)$$

$$\Delta \mathbf{b}_{gi} = \Delta \hat{\mathbf{b}}_{gi} + \Delta \tilde{\mathbf{b}}_{gi} \quad (115)$$

$$\Delta \mathbf{b}_{ai} = \Delta \hat{\mathbf{b}}_{ai} + \Delta \tilde{\mathbf{b}}_{ai} \quad (116)$$

Given that, the linearized IMU pre-integration model becomes:

$$\begin{aligned} \begin{bmatrix} \delta \Delta \boldsymbol{\theta}_{i+1} \\ \Delta \tilde{\mathbf{p}}_{i+1} \\ \Delta \tilde{\mathbf{v}}_{i+1} \\ \Delta \tilde{\mathbf{b}}_{gi+1} \\ \Delta \tilde{\mathbf{b}}_{ai+1} \end{bmatrix} &= \begin{bmatrix} \Phi_{nn} & \mathbf{H}_{wa} \mathbf{H}_b^{wa} \\ \mathbf{0}_{6 \times 9} & \mathbf{I}_6 \end{bmatrix} \begin{bmatrix} \delta \Delta \boldsymbol{\theta}_i \\ \Delta \tilde{\mathbf{p}}_i \\ \Delta \tilde{\mathbf{v}}_i \\ \Delta \tilde{\mathbf{b}}_{gi} \\ \Delta \tilde{\mathbf{b}}_{ai} \end{bmatrix} + \begin{bmatrix} \mathbf{H}_{wa} \mathbf{H}_{b_k}^{wa} \\ \mathbf{0} \end{bmatrix} \begin{bmatrix} \tilde{\mathbf{b}}_{g_k} \\ \tilde{\mathbf{b}}_{a_k} \end{bmatrix} + \begin{bmatrix} \mathbf{H}_{wa} \mathbf{H}_{in}^{wa} \\ \mathbf{0} \end{bmatrix} \begin{bmatrix} \tilde{\mathbf{x}}_{Dw} \\ \tilde{\mathbf{x}}_{Da} \\ \tilde{\mathbf{x}}_{Tg} \\ \delta \boldsymbol{\theta}_{Iw} \\ \delta \boldsymbol{\theta}_{Ia} \end{bmatrix} \\ &\quad + \begin{bmatrix} \mathbf{H}_{wa} \mathbf{H}_n^{wa} & \mathbf{0}_{9 \times 6} \\ \mathbf{0}_{6 \times 6} & \mathbf{I}_6 \delta t_i \end{bmatrix} \begin{bmatrix} \mathbf{n}_{dg} \\ \mathbf{n}_{da} \\ \mathbf{n}_{dwg} \\ \mathbf{n}_{dwa} \end{bmatrix} \end{aligned} \quad (117)$$

If the IMU pre-integration error states are denoted by:

$$\tilde{\mathbf{z}}_{I_i} = \begin{bmatrix} \delta\Delta\theta_i^\top & \Delta\tilde{\mathbf{p}}_i^\top & \Delta\tilde{\mathbf{v}}_i^\top & \Delta\tilde{\mathbf{b}}_{gi}^\top & \Delta\tilde{\mathbf{b}}_{ai}^\top \end{bmatrix}^\top \quad (118)$$

Then, we can simplify Eq. (117) by:

$$\tilde{\mathbf{z}}_{I_{i+1}} = \Phi_{i+1,i}\tilde{\mathbf{z}}_{I_i} + \Phi_b\tilde{\mathbf{x}}_{b_k} + \Phi_{in}\tilde{\mathbf{x}}_{in} + \mathbf{G}_i\mathbf{n}_{dI} \quad (119)$$

where $\Phi_{i+1,i}$, Φ_b , Φ_{in} and \mathbf{G}_i are given as:

$$\Phi_{i+1,i} = \begin{bmatrix} \Phi_{nn} & \mathbf{H}_{wa}\mathbf{H}_b^{wa} \\ \mathbf{0}_{6 \times 9} & \mathbf{I}_6 \end{bmatrix} \quad (120)$$

$$\Phi_{nn} = \begin{bmatrix} \hat{\mathbf{R}}_{i,i+1}^\top & \mathbf{0}_3 & \mathbf{0}_3 \\ -\Delta\hat{\mathbf{R}}_i[\hat{\mathbf{p}}_{i,i+1}] & \mathbf{I}_3 & \mathbf{I}_3\delta t_i \\ -\Delta\hat{\mathbf{R}}_i[\hat{\mathbf{v}}_{i,i+1}] & \mathbf{0}_3 & \mathbf{I}_3 \end{bmatrix} \quad (121)$$

$$\mathbf{H}_{wa} = \begin{bmatrix} \mathbf{J}_r(\theta_{i,i+1})\delta t_i & \mathbf{0}_3 \\ -\Delta\hat{\mathbf{R}}_i\boldsymbol{\Xi}_4 & \Delta\hat{\mathbf{R}}_i\boldsymbol{\Xi}_2 \\ -\Delta\hat{\mathbf{R}}_i\boldsymbol{\Xi}_3 & \Delta\hat{\mathbf{R}}_i\boldsymbol{\Xi}_1 \end{bmatrix} \quad (122)$$

$$\Phi_b = \begin{bmatrix} \mathbf{H}_{wa}\mathbf{H}_{b_k}^{wa} \\ \mathbf{0} \end{bmatrix}, \quad \Phi_{in} = \begin{bmatrix} \mathbf{H}_{wa}\mathbf{H}_{in}^{wa} \\ \mathbf{0} \end{bmatrix} \quad (123)$$

$$\mathbf{G}_i = \begin{bmatrix} \mathbf{H}_{wa}\mathbf{H}_n^{wa} & \mathbf{0}_{9 \times 6} \\ \mathbf{0}_{6 \times 6} & \mathbf{I}_6\delta t_i \end{bmatrix} \quad (124)$$

where \mathbf{H}_{wa} , \mathbf{H}_b^{wa} , \mathbf{H}_{in}^{wa} and \mathbf{H}_n^{wa} can be found from Eq. (76). Finally, the measurement covariance \mathbf{Q}_I follows the recursive form:

$$\mathbf{Q}_{I_{i+1}} = \Phi_{i+1,i}\mathbf{Q}_{I_i}\Phi_{i+1,i}^\top + \mathbf{G}_i\mathbf{Q}_d\mathbf{G}_i^\top \quad (125)$$

where \mathbf{Q}_d denotes the discrete noise (\mathbf{n}_g , \mathbf{n}_a , \mathbf{n}_{bg} and \mathbf{n}_{ba}) from IMU readings. Through recursive evaluation of the above equation, we can recover the pre-integrated IMU measurement covariance between t_k and t_j .

5 Base Inertial Costs

Since IMU intrinsics and biases are needed for IMU integration, $\Delta\mathbf{R}$, $\Delta\mathbf{p}$ and $\Delta\mathbf{v}$ are also functions of \mathbf{x}_{in} and \mathbf{x}_b .

In order to avoid re-integration and re-linearization in iterative solvers when the IMU intrinsics and bias estimates are refined, the IMU pre-integration needs to fix the linearization points not only for \mathbf{x}_{b_k} as in [4], but for \mathbf{x}_{in} .

To this end, we model the pre-integrated IMU measurements between time t_k and t_j as $\mathbf{z}_I \sim \mathcal{N}(\hat{\mathbf{z}}_I, \mathbf{Q}_I)$:

$$\mathbf{z}_I = \begin{bmatrix} \log(\Delta\mathbf{R}) \\ \Delta\mathbf{p} \\ \Delta\mathbf{v} \\ \Delta\mathbf{x}_b \end{bmatrix} = \begin{bmatrix} \log(\Delta\mathbf{R}(\mathbf{x}_{b_k}, \mathbf{x}_{in}, \mathbf{n}_\theta)) \\ \Delta\mathbf{p}(\mathbf{x}_{b_k}, \mathbf{x}_{in}, \mathbf{n}_p) \\ \Delta\mathbf{v}(\mathbf{x}_{b_k}, \mathbf{x}_{in}, \mathbf{n}_v) \\ \mathbf{n}_b \end{bmatrix} \quad (126)$$

where the accumulated noises of IMU measurements are denoted with $\mathbf{n}_I = [\mathbf{n}_\theta^\top \ \mathbf{n}_p^\top \ \mathbf{n}_v^\top \ \mathbf{n}_b^\top]^\top$ and $\mathbf{n}_I \sim \mathcal{N}(\mathbf{0}, \mathbf{Q}_I)$ from Section 4.4. We linearize the above measurements at the current state estimate $\hat{\mathbf{x}}$ as:

$$\Delta \mathbf{R} = \Delta \hat{\mathbf{R}} \exp \left(\frac{\partial \delta \Delta \boldsymbol{\theta}}{\partial \tilde{\mathbf{x}}_{b_k}} \tilde{\mathbf{x}}_{b_k} + \frac{\partial \delta \Delta \boldsymbol{\theta}}{\partial \tilde{\mathbf{x}}_{in}} \tilde{\mathbf{x}}_{in} + \mathbf{n}_\theta \right) \quad (127)$$

$$\Delta \mathbf{p} = \Delta \hat{\mathbf{p}} + \frac{\partial \Delta \tilde{\mathbf{p}}}{\partial \tilde{\mathbf{x}}_{b_k}} \tilde{\mathbf{x}}_{b_k} + \frac{\partial \Delta \tilde{\mathbf{p}}}{\partial \tilde{\mathbf{x}}_{in}} \tilde{\mathbf{x}}_{in} + \mathbf{n}_p \quad (128)$$

$$\Delta \mathbf{v} = \Delta \hat{\mathbf{v}} + \frac{\partial \Delta \tilde{\mathbf{v}}}{\partial \tilde{\mathbf{x}}_{b_k}} \tilde{\mathbf{x}}_{b_k} + \frac{\partial \Delta \tilde{\mathbf{v}}}{\partial \tilde{\mathbf{x}}_{in}} \tilde{\mathbf{x}}_{in} + \mathbf{n}_v \quad (129)$$

$$\Delta \mathbf{x}_b = \mathbf{n}_b \quad (130)$$

Note that the biases or IMU intrinsics Jacobians can be recursively computed. Between time stamp t_k and t_j , we can have integer i such that: with i defined with $k \leq k+i < k+i+1 \leq j$. Hence, we get:

$$\frac{\partial \begin{bmatrix} \delta \Delta \boldsymbol{\theta}_{i+1} \\ \Delta \tilde{\mathbf{p}}_{i+1} \\ \Delta \tilde{\mathbf{v}}_{i+1} \end{bmatrix}}{\partial \tilde{\mathbf{x}}_*} = \Phi_{nn} \frac{\partial \begin{bmatrix} \delta \Delta \boldsymbol{\theta}_i \\ \Delta \tilde{\mathbf{p}}_i \\ \Delta \tilde{\mathbf{v}}_i \end{bmatrix}}{\partial \tilde{\mathbf{x}}_*} + \mathbf{H}_{wa} \mathbf{H}_*^{wa} \quad (131)$$

where $*$ denotes b_k or in . Then, these Jacobians can be rewritten as:

$$\begin{aligned} \frac{\partial \delta \Delta \boldsymbol{\theta}_{i+1}}{\partial \tilde{\mathbf{x}}_*} &= \hat{\mathbf{R}}_{i,i+1}^\top \frac{\partial \delta \Delta \boldsymbol{\theta}_i}{\partial \tilde{\mathbf{x}}_*} + [\mathbf{J}_r(\boldsymbol{\theta}_{i,i+1}) \delta t_i \quad \mathbf{0}_3] \mathbf{H}_*^{wa} \\ \frac{\partial \Delta \tilde{\mathbf{p}}_{i+1}}{\partial \tilde{\mathbf{x}}_*} &= -\Delta \hat{\mathbf{R}}_i [\hat{\mathbf{p}}_{i,i+1}] \frac{\partial \delta \Delta \boldsymbol{\theta}_i}{\partial \tilde{\mathbf{x}}_*} + \frac{\partial \Delta \tilde{\mathbf{p}}_i}{\partial \tilde{\mathbf{x}}_*} + \frac{\partial \Delta \tilde{\mathbf{v}}_i}{\partial \tilde{\mathbf{x}}_*} \delta t_i + [-\Delta \hat{\mathbf{R}}_i \boldsymbol{\Xi}_4 \quad \Delta \hat{\mathbf{R}}_i \boldsymbol{\Xi}_2] \mathbf{H}_*^{wa} \\ \frac{\partial \Delta \tilde{\mathbf{v}}_{i+1}}{\partial \tilde{\mathbf{x}}_*} &= -\Delta \hat{\mathbf{R}}_i [\hat{\mathbf{v}}_{i,i+1}] \frac{\partial \delta \Delta \boldsymbol{\theta}_i}{\partial \tilde{\mathbf{x}}_*} + \frac{\partial \Delta \tilde{\mathbf{v}}_i}{\partial \tilde{\mathbf{x}}_*} + \Delta \hat{\mathbf{R}}_i [-\boldsymbol{\Xi}_3 \quad \boldsymbol{\Xi}_1] \mathbf{H}_*^{wa} \end{aligned}$$

We would like to fix linearization points for the bias states and IMU intrinsics states with initial guesses to avoid the re-integration of the IMU measurements during iterative solving. If we use $\hat{\mathbf{x}}^{(0)}$ denote the initial estimates while $\tilde{\mathbf{x}}^{(0)}$ denote the corresponding initial error states, then we have:

$$\mathbf{x} = \hat{\mathbf{x}} + \tilde{\mathbf{x}} = \hat{\mathbf{x}}^{(0)} + \tilde{\mathbf{x}}^{(0)} \quad (132)$$

$$\Rightarrow \tilde{\mathbf{x}}^{(0)} = \hat{\mathbf{x}} - \hat{\mathbf{x}}^{(0)} + \tilde{\mathbf{x}} \triangleq \Delta \hat{\mathbf{x}} + \tilde{\mathbf{x}} \quad (133)$$

The IMU measurements can be linearized with the initial estimates $\hat{\mathbf{x}}^{(0)}$ as:

$$\Delta \mathbf{R} = \Delta \hat{\mathbf{R}}^{(0)} \exp \left(\frac{\partial \delta \Delta \boldsymbol{\theta}}{\partial \tilde{\mathbf{x}}_{b_k}} \tilde{\mathbf{x}}_{b_k}^{(0)} + \frac{\partial \delta \Delta \boldsymbol{\theta}}{\partial \tilde{\mathbf{x}}_{in}} \tilde{\mathbf{x}}_{in}^{(0)} + \mathbf{n}_\theta \right) \quad (134)$$

$$\begin{aligned} \Delta \mathbf{p} &= \Delta \hat{\mathbf{p}}^{(0)} + \frac{\partial \Delta \tilde{\mathbf{p}}}{\partial \tilde{\mathbf{x}}_{b_k}} \tilde{\mathbf{x}}_{b_k}^{(0)} + \frac{\partial \Delta \tilde{\mathbf{p}}}{\partial \tilde{\mathbf{x}}_{in}} \tilde{\mathbf{x}}_{in}^{(0)} + \mathbf{n}_p \\ &= \mathbf{h}_p(\mathbf{x}_{I_k}, \mathbf{x}_{I_j}) \end{aligned} \quad (135)$$

$$\begin{aligned} \Delta \mathbf{v} &= \Delta \hat{\mathbf{v}}^{(0)} + \frac{\partial \Delta \tilde{\mathbf{v}}}{\partial \tilde{\mathbf{x}}_{b_k}} \tilde{\mathbf{x}}_{b_k}^0 + \frac{\partial \Delta \tilde{\mathbf{v}}}{\partial \tilde{\mathbf{x}}_{in}} \tilde{\mathbf{x}}_{in}^0 + \mathbf{n}_v \\ &= \mathbf{h}_v(\mathbf{x}_{I_k}, \mathbf{x}_{I_j}) \end{aligned} \quad (136)$$

By applying Eq. (133) to Eq. (134)-(136), the pre-integrated IMU measurement with initial biases and initial IMU intrinsic estimates can be rewritten as:

$$\begin{aligned}\Delta\hat{\mathbf{R}}^{(0)} &= \mathbf{h}_R(\mathbf{x}_{I_k}, \mathbf{x}_{I_j}) \cdot \exp\left(-\frac{\partial\delta\Delta\theta}{\partial\tilde{\mathbf{x}}_{b_k}}(\Delta\hat{\mathbf{x}}_{b_k} + \tilde{\mathbf{x}}_{b_k}) - \frac{\partial\delta\Delta\theta}{\partial\tilde{\mathbf{x}}_{in}}(\Delta\hat{\mathbf{x}}_{in} + \tilde{\mathbf{x}}_{in}) - \mathbf{n}_\theta\right) \\ \Delta\hat{\mathbf{p}}^{(0)} &= \mathbf{h}_p(\mathbf{x}_{I_k}, \mathbf{x}_{I_j}) - \frac{\partial\Delta\tilde{\mathbf{p}}}{\partial\tilde{\mathbf{x}}_{b_k}}(\Delta\hat{\mathbf{x}}_{b_k} + \tilde{\mathbf{x}}_{b_k}) - \frac{\partial\Delta\tilde{\mathbf{p}}}{\partial\tilde{\mathbf{x}}_{in}}(\Delta\hat{\mathbf{x}}_{in} + \tilde{\mathbf{x}}_{in}) - \mathbf{n}_p \\ \Delta\hat{\mathbf{v}}^{(0)} &= \mathbf{h}_v(\mathbf{x}_{I_k}, \mathbf{x}_{I_j}) - \frac{\partial\Delta\tilde{\mathbf{v}}}{\partial\tilde{\mathbf{x}}_{b_k}}(\Delta\hat{\mathbf{x}}_{b_k} + \tilde{\mathbf{x}}_{b_k}) - \frac{\partial\Delta\tilde{\mathbf{v}}}{\partial\tilde{\mathbf{x}}_{in}}(\Delta\hat{\mathbf{x}}_{in} + \tilde{\mathbf{x}}_{in}) - \mathbf{n}_v\end{aligned}$$

We define $\boldsymbol{\theta}_{corr}$, \mathbf{p}_{corr} and \mathbf{v}_{corr} as the orientation, position and velocity correction terms due to the linearization point changes of \mathbf{x}_{b_k} and \mathbf{x}_{in} :

$$\boldsymbol{\theta}_{corr} = \frac{\partial\delta\Delta\theta}{\partial\tilde{\mathbf{x}}_{b_k}}\Delta\hat{\mathbf{x}}_{b_k} + \frac{\partial\delta\Delta\theta}{\partial\tilde{\mathbf{x}}_{in}}\Delta\hat{\mathbf{x}}_{in} \quad (137)$$

$$\mathbf{p}_{corr} \triangleq \frac{\partial\Delta\tilde{\mathbf{p}}}{\partial\tilde{\mathbf{x}}_{b_k}}\Delta\hat{\mathbf{x}}_{b_k} + \frac{\partial\Delta\tilde{\mathbf{p}}}{\partial\tilde{\mathbf{x}}_{in}}\Delta\hat{\mathbf{x}}_{in} \quad (138)$$

$$\mathbf{v}_{corr} \triangleq \frac{\partial\Delta\tilde{\mathbf{v}}}{\partial\tilde{\mathbf{x}}_{b_k}}\Delta\hat{\mathbf{x}}_{b_k} + \frac{\partial\Delta\tilde{\mathbf{v}}}{\partial\tilde{\mathbf{x}}_{in}}\Delta\hat{\mathbf{x}}_{in} \quad (139)$$

Finally, the base IMU preintegration measurements is formulated in Eq. (140).

$$\underbrace{\begin{bmatrix} \log(\Delta\hat{\mathbf{R}}^{(0)}) \\ \Delta\hat{\mathbf{p}}^{(0)} \\ \Delta\hat{\mathbf{v}}^{(0)} \\ \mathbf{0}_{6 \times 1} \end{bmatrix}}_{\mathbf{z}'_I} = \underbrace{\begin{bmatrix} \log\left(\mathbf{h}_R(\mathbf{x}_{I_k}, \mathbf{x}_{I_j}) \exp\left(-\frac{\partial\delta\Delta\theta}{\partial\tilde{\mathbf{x}}_{b_k}}\tilde{\mathbf{x}}_{b_k} - \frac{\partial\delta\Delta\theta}{\partial\tilde{\mathbf{x}}_{in}}\tilde{\mathbf{x}}_{in} - \boldsymbol{\theta}_{corr}\right) \exp(-\mathbf{n}'_\theta)\right) \\ \mathbf{h}_p(\mathbf{x}_{I_k}, \mathbf{x}_{I_j}) - \frac{\partial\Delta\tilde{\mathbf{p}}}{\partial\tilde{\mathbf{x}}_{b_k}}\tilde{\mathbf{x}}_{b_k} - \frac{\partial\Delta\tilde{\mathbf{p}}}{\partial\tilde{\mathbf{x}}_{in}}\tilde{\mathbf{x}}_{in} - \mathbf{p}_{corr} - \mathbf{n}_p \\ \mathbf{h}_v(\mathbf{x}_{I_k}, \mathbf{x}_{I_j}) - \frac{\partial\Delta\tilde{\mathbf{v}}}{\partial\tilde{\mathbf{x}}_{b_k}}\tilde{\mathbf{x}}_{b_k} - \frac{\partial\Delta\tilde{\mathbf{v}}}{\partial\tilde{\mathbf{x}}_{in}}\tilde{\mathbf{x}}_{in} - \mathbf{v}_{corr} - \mathbf{n}_v \\ \mathbf{x}_{b_j} - \mathbf{x}_{b_k} - \mathbf{n}_b \end{bmatrix}}_{\mathbf{h}_I(\mathbf{x}_{I_k}, \mathbf{x}_{I_j}, \mathbf{x}_{in}, \mathbf{n}'_I)} \quad (140)$$

The new IMU measurement noise \mathbf{n}'_I is computed as:

$$\mathbf{n}'_I \triangleq \begin{bmatrix} \mathbf{n}'_\theta \\ \mathbf{n}_p \\ \mathbf{n}_v \\ \mathbf{n}_b \end{bmatrix} = \underbrace{\begin{bmatrix} \mathbf{J}_r(-\boldsymbol{\theta}_{corr}) & \mathbf{0}_{3 \times 12} \\ \mathbf{0}_{12 \times 3} & \mathbf{I}_{12} \end{bmatrix}}_{\mathbf{H}_{n'}} \begin{bmatrix} \mathbf{n}_\theta \\ \mathbf{n}_p \\ \mathbf{n}_v \\ \mathbf{n}_b \end{bmatrix} \triangleq \mathbf{H}_{n'} \mathbf{n}_I \quad (141)$$

with covariance $\mathbf{n}'_I \sim \mathcal{N}(\mathbf{0}, \mathbf{Q}'_I)$ and $\mathbf{Q}'_I = \mathbf{H}_{n'} \mathbf{Q}_I \mathbf{H}_{n'}^\top$. As compared to the conventional IMU pre-integration [4] and general pre-integration [28] with only mean correction, we have both the mean and covariance corrections when linearization points change for biases and IMU intrinsics. In addition, we also model cross correlations between IMU navigation state and bias state, which are missing from [4] and [28]. Finally, the corresponding base IMU pre-integration cost is:

$$C_I \triangleq \|\mathbf{z}'_I \boxminus \mathbf{h}(\mathbf{x}_{I_k}, \mathbf{x}_{I_j}, \mathbf{x}_{in})\|_{(\mathbf{Q}'_I)^{-1}}^2 \quad (142)$$

6 Auxiliary Inertial Costs

Leveraging the base IMU pre-integration measurements [see Eq. (140)], we now show how to derive the costs for the auxiliary IMU and gyroscope by using the rigid body constraints between the base and auxiliary IMUs/gyroscopes.

6.1 Auxiliary IMU Cost

As the auxiliary IMUs are considered to be temporally asynchronous with the base IMU, we employ pose interpolation to convert the associate the base IMU state with the auxiliary IMU state at the start and end of the integration period. The rigid body constraint between the auxiliary and base IMU with interpolation terms is given by:

$$\begin{bmatrix} {}^G_{I_a} \mathbf{R} & {}^G \mathbf{p}_{I_a} \\ \mathbf{0}_{1 \times 3} & 1 \end{bmatrix} \triangleq \begin{bmatrix} {}^G_{I_{in}} \mathbf{R} & {}^G \mathbf{p}_{I_{in}} \\ \mathbf{0}_{1 \times 3} & 1 \end{bmatrix} \begin{bmatrix} {}^I_{I_a} \mathbf{R} & {}^I \mathbf{p}_{I_a} \\ \mathbf{0}_{1 \times 3} & 1 \end{bmatrix} \quad (143)$$

where $\{{}^G_{I_{in}} \mathbf{R}, {}^G \mathbf{p}_{I_{in}}\}$ is the interpolated pose computed with constant linear velocity ${}^G \mathbf{v}_I$ and constant angular velocity ${}^I \boldsymbol{\omega}$:

$$\begin{bmatrix} {}^G_{I_{in}} \mathbf{R} & {}^G \mathbf{p}_{I_{in}} \\ \mathbf{0}_{1 \times 3} & 1 \end{bmatrix} = \begin{bmatrix} {}^G_I \mathbf{R} & {}^G \mathbf{p}_I \\ \mathbf{0}_{1 \times 3} & 1 \end{bmatrix} \begin{bmatrix} \exp({}^I \boldsymbol{\omega} t_d) & {}^G \mathbf{v}_I t_d \\ \mathbf{0}_{1 \times 3} & 1 \end{bmatrix}$$

The auxiliary IMU pose $\{{}^G_{I_a} \mathbf{R}, {}^G \mathbf{p}_{I_a}\}$ can be found with the base IMU pose $\{{}^G_I \mathbf{R}, {}^G \mathbf{p}_I\}$ as:

$${}^G_{I_a} \mathbf{R} = {}^G_I \mathbf{R} \exp({}^I \boldsymbol{\omega} t_d) {}^I_{I_a} \mathbf{R} \quad (144)$$

$${}^G \mathbf{p}_{I_a} = {}^G_I \mathbf{R} {}^G \mathbf{v}_I t_d + {}^G \mathbf{p}_I + {}^G_I \mathbf{R} \exp({}^I \boldsymbol{\omega} t_d) {}^I \mathbf{p}_{I_a} \quad (145)$$

Note that ${}^I \boldsymbol{\omega}$ denotes the angular velocity from the base IMU. Since ${}^I \boldsymbol{\omega}$ is not in the state vector, we need to use the current best estimate of the ${}^I \hat{\boldsymbol{\omega}}$.

There is no need to keep auxiliary IMU pose in the state vector, because the auxiliary IMU pose can be expressed by the base IMU state \mathbf{x}_I and extrinsics \mathbf{x}_{I_A} . The auxiliary IMU state, Eq. (24), only contains the auxiliary IMU velocity and biases. We need to reformulate the pre-integration Eq. (54)-(56) for the auxiliary IMU cost with the Eq. (144)-(145) rigid body constraints. Following Eq. (140), with some abuse of the notations for the auxiliary IMU pre-integrated measurements \mathbf{z}'_{I_a} and noises \mathbf{n}'_{I_a} , we can define auxiliary IMU residual as Eq. (146).

$$\underbrace{\begin{bmatrix} \log(\Delta \hat{\mathbf{R}}^{(0)}) \\ \Delta \hat{\mathbf{p}}^{(0)} \\ \Delta \hat{\mathbf{v}}^{(0)} \\ \mathbf{0}_{6 \times 1} \end{bmatrix}}_{\mathbf{z}'_{I_a}} = \underbrace{\begin{bmatrix} \log \left(\mathbf{h}_R(\cdot) \exp \left(-\frac{\partial \delta \Delta \theta}{\partial \tilde{\mathbf{x}}_{A_{bk}}} \tilde{\mathbf{x}}_{A_{bk}} - \frac{\partial \delta \Delta \theta}{\partial \tilde{\mathbf{x}}_{A_{in}}} \tilde{\mathbf{x}}_{A_{in}} - \boldsymbol{\theta}_{A_{corr}} \right) \exp(-\mathbf{n}'_\theta) \right) \\ \mathbf{h}_p(\cdot) - \frac{\partial \Delta \tilde{\mathbf{p}}}{\partial \tilde{\mathbf{x}}_{A_{bk}}} \tilde{\mathbf{x}}_{A_{bk}} - \frac{\partial \Delta \tilde{\mathbf{p}}}{\partial \tilde{\mathbf{x}}_{A_{in}}} \tilde{\mathbf{x}}_{A_{in}} - \mathbf{p}_{A_{corr}} - \mathbf{n}_p \\ \mathbf{h}_v(\cdot) - \frac{\partial \Delta \tilde{\mathbf{v}}}{\partial \tilde{\mathbf{x}}_{A_{bk}}} \tilde{\mathbf{x}}_{A_{bk}} - \frac{\partial \Delta \tilde{\mathbf{v}}}{\partial \tilde{\mathbf{x}}_{A_{in}}} \tilde{\mathbf{x}}_{A_{in}} - \mathbf{v}_{A_{corr}} - \mathbf{n}_v \\ \mathbf{x}_{A_{bj}} - \mathbf{x}_{A_{bk}} - \mathbf{n}_b \end{bmatrix}}_{\mathbf{h}_A(\mathbf{x}, \mathbf{n}'_{I_a})} \quad (146)$$

We have defined $\mathbf{h}_R(\cdot)$, $\mathbf{h}_p(\cdot)$ and $\mathbf{h}_v(\cdot)$ for the auxiliary IMU:

$$\begin{aligned} \mathbf{h}_R(\cdot) &\triangleq {}^G_{I_{a_k}} \mathbf{R}^\top {}^G_{I_{a_j}} \mathbf{R} \\ &\triangleq ({}^G_{I_k} \mathbf{R} \exp({}^I_k \boldsymbol{\omega} t_d) {}^I_{I_a} \mathbf{R})^\top {}^G_{I_j} \mathbf{R} \exp({}^I_j \boldsymbol{\omega} t_d) {}^I_{I_a} \mathbf{R} \\ &\triangleq \mathbf{h}_R(\mathbf{x}_{I_k}, \mathbf{x}_{I_j}, \mathbf{x}_{I_A}) \\ \mathbf{h}_p(\cdot) &\triangleq {}^G_{I_{a_k}} \mathbf{R}^\top \left({}^G \mathbf{p}_{I_{a_j}} - {}^G \mathbf{p}_{I_{a_k}} - {}^G \mathbf{v}_{I_{a_k}} \delta t - \frac{1}{2} {}^G \mathbf{g} \delta t^2 \right) \\ &\triangleq \mathbf{h}_p(\mathbf{x}_{I_k}, \mathbf{x}_{I_j}, \mathbf{x}_{I_{a_k}}, \mathbf{x}_{I_A}) \\ \mathbf{h}_v(\cdot) &\triangleq {}^G_{I_{a_k}} \mathbf{R}^\top \left({}^G \mathbf{v}_{I_{a_j}} - {}^G \mathbf{v}_{I_{a_k}} - {}^G \mathbf{g} \delta t \right) \\ &\triangleq \mathbf{h}_v(\mathbf{x}_{I_k}, \mathbf{x}_{I_{a_k}}, \mathbf{x}_{I_{a_j}}, \mathbf{x}_{I_A}) \end{aligned}$$

Following Eq. (137)-(139), the linearization correction terms of orientation $\boldsymbol{\theta}_{A_{corr}}$, position $\mathbf{p}_{A_{corr}}$ and velocity $\mathbf{v}_{A_{corr}}$ for the auxiliary IMU are given by:

$$\boldsymbol{\theta}_{A_{corr}} = \frac{\partial \delta \Delta \boldsymbol{\theta}}{\partial \tilde{\mathbf{x}}_{A_{b_k}}} \Delta \hat{\mathbf{x}}_{A_{b_k}} + \frac{\partial \delta \Delta \boldsymbol{\theta}}{\partial \tilde{\mathbf{x}}_{A_{in}}} \Delta \hat{\mathbf{x}}_{A_{in}} \quad (147)$$

$$\mathbf{p}_{A_{corr}} = \frac{\partial \Delta \tilde{\mathbf{p}}}{\partial \tilde{\mathbf{x}}_{A_{b_k}}} \Delta \hat{\mathbf{x}}_{A_{b_k}} + \frac{\partial \Delta \tilde{\mathbf{p}}}{\partial \tilde{\mathbf{x}}_{A_{in}}} \Delta \hat{\mathbf{x}}_{A_{in}} \quad (148)$$

$$\mathbf{v}_{A_{corr}} = \frac{\partial \Delta \tilde{\mathbf{v}}}{\partial \tilde{\mathbf{x}}_{A_{b_k}}} \Delta \hat{\mathbf{x}}_{A_{b_k}} + \frac{\partial \Delta \tilde{\mathbf{v}}}{\partial \tilde{\mathbf{x}}_{A_{in}}} \Delta \hat{\mathbf{x}}_{A_{in}} \quad (149)$$

Finally, the corresponding auxiliary IMU cost is given by:

$$\mathbb{C}_{I_a} \triangleq \|\mathbf{z}'_{I_a} \boxminus \mathbf{h}(\mathbf{x}, \mathbf{n}'_{I_a})\|_{(\mathbf{Q}'_{I_a})^{-1}}^2 \quad (150)$$

6.2 Auxiliary Gyroscope Cost

Similarly, the auxiliary gyroscope cost can be derived as the integration of angular velocity and gyroscope biases. The gyroscope state is defined as gyroscope biases, the intrinsics \mathbf{x}_{G_w} and the extrinsics \mathbf{x}_{I_G} . The rotation constraint when considering a time offset is written as:

$${}_{I_g}^G \mathbf{R} = {}_I^G \mathbf{R} \exp({}^I \boldsymbol{\omega} t_{dg}) {}_{I_g}^I \mathbf{R} \quad (151)$$

Reusing the notation $\mathbf{h}_R(\cdot)$, see Eq. (54), we get the gyroscope rotation function as :

$$\begin{aligned} \mathbf{h}_R(\cdot) &\triangleq {}_{I_{g_k}}^G \mathbf{R} {}_{I_{g_j}}^G \mathbf{R}^\top \\ &\triangleq \left({}_{I_k}^G \mathbf{R} \exp({}^{I_k} \boldsymbol{\omega} t_{dg}) {}_{I_g}^I \mathbf{R} \right)^\top {}_{I_j}^G \mathbf{R} \exp({}^{I_j} \boldsymbol{\omega} t_{dg}) {}_{I_g}^I \mathbf{R} \\ &\triangleq \mathbf{h}_R(\mathbf{x}_{I_k}, \mathbf{x}_{I_j}, \mathbf{x}_{I_G}) \end{aligned}$$

where we still use the current best estimate for the ${}^I \boldsymbol{\omega}$. The pre-integrated auxiliary gyroscope measurements and noises is defined in Eq. (152).

$$\underbrace{\begin{bmatrix} \log(\Delta \hat{\mathbf{R}}^{(0)}) \\ \mathbf{0}_{3 \times 1} \end{bmatrix}}_{\mathbf{z}'_{I_g}} = \underbrace{\begin{bmatrix} \log \left(\mathbf{h}_R(\cdot) \exp \left(-\frac{\partial \delta \Delta \boldsymbol{\theta}}{\partial \tilde{\mathbf{b}}_{G_{gk}}} \tilde{\mathbf{b}}_{G_{gk}} - \frac{\partial \delta \Delta \boldsymbol{\theta}}{\partial \tilde{\mathbf{x}}_{G_{in}}} \tilde{\mathbf{x}}_{G_{in}} - \boldsymbol{\theta}_{G_{corr}} \right) \exp(-\mathbf{n}'_{\boldsymbol{\theta}}) \right) \\ \mathbf{b}_{G_{gj}} - \mathbf{b}_{G_{gk}} - \mathbf{n}_g \end{bmatrix}}_{\mathbf{h}(\mathbf{x}, \mathbf{n}'_{I_g})} \quad (152)$$

The linearization correction term is defined as:

$$\boldsymbol{\theta}_{G_{corr}} = \frac{\partial \delta \Delta \boldsymbol{\theta}}{\partial \tilde{\mathbf{b}}_{G_{gk}}} \Delta \hat{\mathbf{b}}_{G_{gk}} + \frac{\partial \delta \Delta \boldsymbol{\theta}}{\partial \tilde{\mathbf{x}}_{G_{in}}} \Delta \hat{\mathbf{x}}_{G_{in}} \quad (153)$$

Finally, the auxiliary gyroscope cost is given by:

$$\mathbb{C}_{I_g} \triangleq \|\mathbf{z}'_{I_g} \boxminus \mathbf{h}(\mathbf{x}, \mathbf{n}'_{I_g})\|_{(\mathbf{Q}'_{I_g})^{-1}}^2 \quad (154)$$

6.3 Auxiliary Inertial Sensor Initialization

An initial linearization point of the auxiliary inertial states is required to perform optimization. This can be done by leveraging the initial linearization point of the base IMU. Specifically, we initialize the IMU state \mathbf{x}_{Ia} , which contains the velocity ${}^G\mathbf{v}_{Ia}$ and biases (\mathbf{b}_{A_g} and \mathbf{b}_{A_a}) of the auxiliary IMU, as follows:

- The initial velocity of the auxiliary IMU is computed based on the rigid body constraints:

$${}^G\mathbf{v}_{Ia} = {}^G\mathbf{v}_I + {}_I^G\mathbf{R} [{}_{Ia}^I \mathbf{R}^{Ia} \boldsymbol{\omega}]^I \mathbf{p}_{Ia} \quad (155)$$

- For $\hat{\mathbf{b}}_{A_{g_k}}$, we integrate the angular velocity measurements with zero bias for auxiliary IMU to get $\Delta\mathbf{R}_a$. Then the following linear system can be solved:

$$\frac{\partial \delta \Delta \boldsymbol{\theta}}{\partial \tilde{\mathbf{b}}_{A_{g_k}}} \cdot \hat{\mathbf{b}}_{A_{g_k}} = \log \left(\Delta \mathbf{R}_a^T {}_{I_{a_k}}^G \mathbf{R}^T {}_{I_{a_{k+1}}}^G \mathbf{R} \right) \quad (156)$$

where ${}_{I_{a_k}}^G \mathbf{R}$ and ${}_{I_{a_{k+1}}}^G \mathbf{R}$ denote the orientation of the auxiliary IMU which can be computed from base IMU orientation with IMU-IMU extrinsics.

- For $\hat{\mathbf{b}}_{A_{a_k}}$, the accelerometer bias is initialized to $\mathbf{0}_{3 \times 1}$.

7 Visual Costs

We build the complete camera measurement function $\mathbf{h}_C(\cdot)$ by incorporating the distortion function $\mathbf{h}_d(\cdot)$ [see Eq. (7)], the projection function $\mathbf{h}_p(\cdot)$ [see Eq. (13)] and the transformation function $\mathbf{h}_t(\cdot)$ [see Eq. (14)] [6, 8]:

$$\mathbf{z}_C = \mathbf{h}_C(\mathbf{x}) + \mathbf{n}_C \quad (157)$$

$$= \mathbf{h}_d(\mathbf{z}_n, \mathbf{x}_{C_{in}}) + \mathbf{n}_C \quad (158)$$

$$= \mathbf{h}_d(\mathbf{h}_p({}^C \mathbf{p}_f), \mathbf{x}_{C_{in}}) + \mathbf{n}_C \quad (159)$$

$$= \mathbf{h}_d(\mathbf{h}_p(\mathbf{h}_t({}^G \mathbf{p}_{C(t)} \mathbf{R}, {}^G \mathbf{p}_{C(t)}, {}^G \mathbf{p}_f)), \mathbf{x}_{C_{in}}) + \mathbf{n}_C \quad (160)$$

We need to linearize the camera model for update, which is given by:

$$\tilde{\mathbf{z}}_C \simeq \mathbf{H}_C \tilde{\mathbf{x}} + \mathbf{n}_C \quad (161)$$

where $\tilde{\mathbf{z}}_C \triangleq \mathbf{z}_C - \mathbf{h}_C(\hat{\mathbf{x}})$ and $\mathbf{H}_C \triangleq \frac{\partial \tilde{\mathbf{z}}_C}{\partial \tilde{\mathbf{x}}}$. Using the chain rule, we get the following Jacobian matrix:

$$\begin{aligned} \mathbf{H}_C &= \begin{bmatrix} \frac{\partial \tilde{\mathbf{z}}_C}{\partial \tilde{\mathbf{x}}_I} & \frac{\partial \tilde{\mathbf{z}}_C}{\partial \tilde{\mathbf{x}}_{I_C}} & \frac{\partial \tilde{\mathbf{z}}_C}{\partial \tilde{\mathbf{x}}_{C_{in}}} & \frac{\partial \tilde{\mathbf{z}}_C}{\partial \tilde{\mathbf{x}}_f} \end{bmatrix} \\ &= \begin{bmatrix} \mathbf{H}_{\mathbf{p}_f} \frac{\partial {}^C \tilde{\mathbf{p}}_f}{\partial \tilde{\mathbf{x}}_I} & \mathbf{H}_{\mathbf{p}_f} \frac{\partial {}^C \tilde{\mathbf{p}}_f}{\partial \tilde{\mathbf{x}}_{I_C}} & \mathbf{H}_{\mathbf{p}_f} \frac{\partial \tilde{\mathbf{z}}_C}{\partial \tilde{\mathbf{x}}_{C_{in}}} & \mathbf{H}_{\mathbf{p}_f} \frac{\partial {}^C \tilde{\mathbf{p}}_f}{\partial \tilde{\mathbf{x}}_f} \end{bmatrix} \end{aligned} \quad (162)$$

where $\mathbf{H}_{\mathbf{p}_f} = \frac{\partial \tilde{\mathbf{z}}_C}{\partial \tilde{\mathbf{z}}_n} \frac{\partial \tilde{\mathbf{z}}_n}{\partial {}^C \tilde{\mathbf{p}}_f}$. We show how to use `radtan` distortion model to compute $\frac{\partial {}^C \tilde{\mathbf{p}}_f}{\partial \tilde{\mathbf{x}}_I}$, $\frac{\partial {}^C \tilde{\mathbf{p}}_f}{\partial \tilde{\mathbf{x}}_{I_C}}$, $\frac{\partial \tilde{\mathbf{z}}_C}{\partial \tilde{\mathbf{x}}_{C_{in}}}$, $\frac{\partial {}^C \tilde{\mathbf{p}}_f}{\partial \tilde{\mathbf{x}}_f}$ and $\mathbf{H}_{\mathbf{p}_f}$. The camera intrinsic Jacobians $\mathbf{H}_{Cin} = \frac{\partial \tilde{\mathbf{z}}_C}{\partial \tilde{\mathbf{x}}_{C_{in}}}$ can be written as:

$$\mathbf{H}_{Cin} = \begin{bmatrix} \frac{\partial \tilde{\mathbf{z}}_C}{\partial [\tilde{f}_u \ \tilde{f}_v \ \tilde{c}_u \ \tilde{c}_v]^\top} & \frac{\partial \tilde{\mathbf{z}}_C}{\partial [\tilde{k}_1 \ \tilde{k}_2 \ \tilde{p}_1 \ \tilde{p}_2]^\top} \end{bmatrix} \quad (163)$$

$$\frac{\partial \tilde{\mathbf{z}}_C}{\partial [\tilde{f}_u \ \tilde{f}_v \ \tilde{c}_u \ \tilde{c}_v]^\top} = \begin{bmatrix} u_d & 0 & 1 & 0 \\ 0 & v_d & 0 & 1 \end{bmatrix} \quad (164)$$

$$\frac{\partial \tilde{\mathbf{z}}_C}{\partial [\tilde{k}_1 \ \tilde{k}_2 \ \tilde{p}_1 \ \tilde{p}_2]^\top} = \begin{bmatrix} f_u u_n r^2 & f_u u_n r^4 & 2 f_u u_n v_n & f_u (r^2 + 2 u_n^2) \\ f_v v_n r^2 & f_v v_n r^4 & f_v (r^2 + 2 v_n^2) & 2 f_v u_n v_n \end{bmatrix} \quad (165)$$

We continue to compute $\frac{\partial \tilde{\mathbf{z}}_C}{\partial \tilde{\mathbf{z}}_n}$ and $\frac{\partial \tilde{\mathbf{z}}_n}{\partial {}^C \tilde{\mathbf{p}}_f}$ for $\mathbf{H}_{\mathbf{p}_f}$ within Eq. (162) as:

$$\frac{\partial \tilde{\mathbf{z}}_C}{\partial \tilde{\mathbf{z}}_n} = \begin{bmatrix} h_{11} & h_{12} \\ h_{21} & h_{22} \end{bmatrix} \quad (166)$$

$$h_{11} = f_u(d + 2k_1 u_n^2 + 4k_2 u_n^2 r^2 + 2p_1 v_n + 6p_2 u_n)$$

$$h_{12} = f_u(2k_1 u_n v_n + 4k_2 u_n v_n r^2 + 2p_1 u_n + 2p_2 v_n)$$

$$h_{21} = f_v(2k_1 u_n v_n + 4k_2 u_n v_n r^2 + 2p_1 u_n + 2p_2 v_n)$$

$$h_{22} = f_v(d + 2k_1 v_n^2 + 4k_2 v_n^2 r^2 + 6p_1 v_n + 2p_2 u_n)$$

$$\frac{\partial \tilde{\mathbf{z}}_C}{\partial {}^C \tilde{\mathbf{p}}_f} = \frac{1}{{}^C z_f^2} \begin{bmatrix} {}^C z_f & 0 & -{}^C x_f \\ 0 & {}^C z_f & -{}^C y_f \end{bmatrix} \quad (167)$$

The Jacobians of ${}^C \mathbf{p}_f$ regarding to the IMU state \mathbf{x}_I are written as:

$$\frac{\partial {}^C \tilde{\mathbf{p}}_f}{\partial \tilde{\mathbf{x}}_I} = \left[\frac{\partial {}^C \tilde{\mathbf{p}}_f}{\partial \tilde{\mathbf{x}}_n} \quad \frac{\partial {}^C \tilde{\mathbf{p}}_f}{\partial \tilde{\mathbf{x}}_b} \quad \frac{\partial {}^C \tilde{\mathbf{p}}_f}{\partial \tilde{\mathbf{x}}_{in}} \right] \quad (168)$$

$$\frac{\partial {}^C \tilde{\mathbf{p}}_f}{\partial \tilde{\mathbf{x}}_n} = {}_I^C \hat{\mathbf{R}}_G^I \hat{\mathbf{R}} [({}^G \hat{\mathbf{p}}_f - {}^G \hat{\mathbf{p}}_I)] {}_I^G \hat{\mathbf{R}}^I \quad (169)$$

$$\frac{\partial {}^C \tilde{\mathbf{p}}_f}{\partial \tilde{\mathbf{x}}_b} = \mathbf{0}_{3 \times 6}, \quad \frac{\partial {}^C \tilde{\mathbf{p}}_f}{\partial \tilde{\mathbf{x}}_{in}} = \mathbf{0}_{3 \times 24} \quad (170)$$

The Jacobians of ${}^C \mathbf{p}_f$ regarding to the IMU-camera spatial-temporal calibration state \mathbf{x}_{I_C} are written as:

$$\frac{\partial {}^C \tilde{\mathbf{p}}_f}{\partial \tilde{\mathbf{x}}_{I_C}} = \left[\frac{\partial {}^C \tilde{\mathbf{p}}_f}{\partial \delta \theta_{I_C}} \quad \frac{\partial {}^C \tilde{\mathbf{p}}_f}{\partial {}^C \tilde{\mathbf{p}}_I} \quad \frac{\partial {}^C \tilde{\mathbf{p}}_f}{\partial \tilde{t}_d} \quad \frac{\partial {}^C \tilde{\mathbf{p}}_f}{\partial \tilde{t}_r} \right] \quad (171)$$

$$\frac{\partial {}^C \tilde{\mathbf{p}}_f}{\partial \delta \theta_{I_C}} = [{}_I^C \hat{\mathbf{R}}_G^I \hat{\mathbf{R}} ({}^G \hat{\mathbf{p}}_f - {}^G \hat{\mathbf{p}}_I)] \quad (172)$$

$$\frac{\partial {}^C \tilde{\mathbf{p}}_f}{\partial {}^C \tilde{\mathbf{p}}_I} = \mathbf{I}_3 \quad (173)$$

$$\frac{\partial {}^C \tilde{\mathbf{p}}_f}{\partial \tilde{t}_d} = {}_I^C \hat{\mathbf{R}}_G^I \hat{\mathbf{R}} \left([({}^G \hat{\mathbf{p}}_f - {}^G \hat{\mathbf{p}}_I)] {}_I^G \hat{\mathbf{R}}^I \hat{\omega} - {}^G \hat{\mathbf{v}}_I \right) \quad (174)$$

$$\frac{\partial {}^C \tilde{\mathbf{p}}_f}{\partial \tilde{t}_r} = \frac{m}{M} \frac{\partial {}^C \tilde{\mathbf{p}}_f}{\partial \tilde{t}_d} \quad (175)$$

Note that when computing the Jacobians for t_d and t_r , we are using the following linearization:

$${}_{I(t)}^G \mathbf{R} \simeq {}_{I(\tilde{t})}^G \hat{\mathbf{R}} \exp(\delta \boldsymbol{\theta}_I) \exp\left({}^I \hat{\boldsymbol{\omega}} \tilde{t}_d + \frac{m}{M} {}^I \hat{\boldsymbol{\omega}} \tilde{t}_r\right) \quad (176)$$

$${}^G \mathbf{p}_{I(t)} \simeq {}^G \hat{\mathbf{p}}_{I(\tilde{t})} + {}^G \tilde{\mathbf{p}}_I + {}^G \hat{\mathbf{v}}_I \tilde{t}_d + \frac{m}{M} {}^G \hat{\mathbf{v}}_I \tilde{t}_r \quad (177)$$

The Jacobians of ${}^C \mathbf{p}_f$ regarding to the feature state \mathbf{x}_f is written as:

$$\frac{\partial {}^C \tilde{\mathbf{p}}_f}{\partial \tilde{\mathbf{x}}_f} = \frac{\partial {}^C \tilde{\mathbf{p}}_f}{\partial \delta {}^G \tilde{\mathbf{p}}_f} = {}_I^C \hat{\mathbf{R}} {}_G^I \hat{\mathbf{R}} \quad (178)$$

Hence, the visual cost can be formulated:

$$\mathbb{C}_C \triangleq \| \mathbf{z}_C - \mathbf{h}_C(\mathbf{x}) \|_{\mathbf{Q}_C^{-1}}^2 \quad (179)$$

We leverage pose interpolation to model the time offset and RS calibration. For example, if the feature measurement is in the m -th row with total M rows in an image, we can find two bounding poses k and $k+1$ based on the measurement time t . The corresponding time t is between two IMU poses, $t_k \leq t \leq t_{k+1}$. We can then find the *virtual* IMU pose $\{{}^G_I \mathbf{R}, {}^G \mathbf{p}_{I(t)}\}$ between poses at k and $k+1$:

$$\lambda = (t_I + t_d + \frac{m}{M} t_r - t_k) / (t_{k+1} - t_k) \quad (180)$$

$${}_{I(t)}^G \mathbf{R} = {}_{I_k}^G \mathbf{R} \exp\left(\lambda \log\left({}_{I_k}^G \mathbf{R} {}_{I_{k+1}}^G \mathbf{R}^\top\right)\right) \quad (181)$$

$${}^G \mathbf{p}_{I(t)} = (1 - \lambda) {}^G \mathbf{p}_{I_k} + \lambda {}^G \mathbf{p}_{I_{k+1}} \quad (182)$$

8 Observability Analysis

Observability analysis plays an important role in state estimation for VINS [47, 48]. This analysis allows for determining the minimum measurements needed to determine the state and identify degenerate motions which may degrade system performance by introducing additional unobservable directions for certain parameters [49, 50, 51, 34]. As MVIS continues to gain popularity, the observability analysis for such a system with full calibration parameters, especially IMU-IMU spatiotemporal calibration, is needed to better understand the foundational properties of the underlying system.

8.1 Reduced State Vector

Although the proposed MVIS supports arbitrary number of auxiliary inertial sensors and cameras, for simplicity and without loss of generality, we use a typical system consisting of only one base IMU, one auxiliary IMU, one auxiliary gyroscope and one RS camera as unique sensors for the following observability analysis [52, 53, 9].

To simplify the ensuing derivation, we re-order the state vector and assume that the base IMU, auxiliary inertial sensors are all kept as full states (i.e. including the full auxiliary inertial state). All the states will be propagated forward with time, while the rigid body constraints and visual measurements will be used to update these states. Specifically, the state vector includes all the necessary parameters for the observability analysis as:

$$\mathbf{x} = [\mathbf{x}_B^\top \ \mathbf{x}_A^\top \ \mathbf{x}_G^\top \ \mathbf{x}_{calib}^\top \ {}^G \mathbf{p}_f^\top]^\top \quad (183)$$

$$\triangleq [\mathbf{x}_I^\top \ \mathbf{x}_{in}^\top \ \mathbf{x}_{I_a}^\top \ \mathbf{x}_{A_{in}}^\top \ \mathbf{x}_{I_g}^\top \ \mathbf{x}_{G_{in}}^\top \ \mathbf{x}_{Ex}^\top \ \mathbf{x}_{C_{in}}^\top \ {}^G \mathbf{p}_f^\top]^\top \quad (184)$$

Note that the auxiliary IMU and gyroscope states are:

$$\mathbf{x}_{I_a} = \begin{bmatrix} {}^G\boldsymbol{\theta}^\top & {}^G\mathbf{p}_{I_a}^\top & {}^G\mathbf{v}_{I_a}^\top & \mathbf{b}_{A_g}^\top & \mathbf{b}_{A_a}^\top \end{bmatrix}^\top \quad (185)$$

$$\mathbf{x}_{I_g} = \begin{bmatrix} {}^G\boldsymbol{\theta}^\top & \mathbf{b}_{G_g}^\top \end{bmatrix}^\top \quad (186)$$

After propagation, the visual measurements and rigid body constraints between inertial sensors are used to update the states with:

$$\mathbf{z} = \begin{bmatrix} \mathbf{z}_C \\ \mathbf{z}_A \\ \mathbf{z}_G \end{bmatrix} \quad (187)$$

where \mathbf{z}_C denotes the visual cost [see Eq. (157)]. By dropping the time step k for simplicity, \mathbf{z}_A and \mathbf{z}_G represent the rigid body pose constraints between auxiliary and base inertial sensors:

$$\mathbf{z}_A = \begin{bmatrix} \log({}^G\mathbf{R}_{I_a}^\top {}^G\mathbf{R}_I^I \mathbf{R}) \\ {}^G\mathbf{p}_{I_a} - {}^G\mathbf{p}_I - {}^G\mathbf{R}^I \mathbf{p}_{I_a} \end{bmatrix} \quad (188)$$

$$\mathbf{z}_G = \log({}^G\mathbf{R}_{I_g}^\top {}^G\mathbf{R}_{I_g}^I \mathbf{R}) \quad (189)$$

8.2 Linearized Observability Analysis

The overall state transition matrix can be written as:

$$\Phi = \text{Diag}\{\Phi_B, \Phi_A, \Phi_G, \Phi_{calib}, \Phi_F\} \quad (190)$$

$$= \begin{bmatrix} \Phi_B & \mathbf{0} & \mathbf{0} & \mathbf{0} & \mathbf{0} \\ \mathbf{0} & \Phi_A & \mathbf{0} & \mathbf{0} & \mathbf{0} \\ \mathbf{0} & \mathbf{0} & \Phi_G & \mathbf{0} & \mathbf{0} \\ \mathbf{0} & \mathbf{0} & \mathbf{0} & \Phi_{calib} & \mathbf{0} \\ \mathbf{0} & \mathbf{0} & \mathbf{0} & \mathbf{0} & \Phi_F \end{bmatrix} \quad (191)$$

The detailed derivations for Φ_B , Φ_A , Φ_G , Φ_{calib} and Φ_F can be found as:

$$\Phi_B = \begin{bmatrix} \Phi_I & \Phi_{in} \\ \mathbf{0} & \mathbf{I} \end{bmatrix}, \quad \Phi_A = \begin{bmatrix} \Phi_{I_a} & \Phi_{A_{in}} \\ \mathbf{0} & \mathbf{I} \end{bmatrix} \quad (192)$$

$$\Phi_G = \begin{bmatrix} \Phi_{I_g} & \Phi_{G_{in}} \\ \mathbf{0} & \mathbf{I} \end{bmatrix}, \quad \Phi_{calib} = \mathbf{I}, \quad \Phi_F = \mathbf{I} \quad (193)$$

The state transition of Φ_B and Φ_A have the same structure. We can grab the gyroscope part of Φ_B to get Φ_G . Therefore, only Φ_B is shown in this paper for clarity. The Φ_I is:

$$\Phi_I = \begin{bmatrix} \Phi_{11} & \mathbf{0}_3 & \mathbf{0}_3 & \Phi_{14} & \Phi_{15} \\ \Phi_{21} & \mathbf{I}_3 & \mathbf{I}_3 \delta t & \Phi_{24} & \Phi_{25} \\ \Phi_{31} & \mathbf{0}_3 & \mathbf{I}_3 & \Phi_{34} & \Phi_{35} \\ \mathbf{0}_3 & \mathbf{0}_3 & \mathbf{0}_3 & \mathbf{I}_3 & \mathbf{0}_3 \\ \mathbf{0}_3 & \mathbf{0}_3 & \mathbf{0}_3 & \mathbf{0}_3 & \mathbf{I}_3 \end{bmatrix} \quad (194)$$

where we have:

$$\begin{aligned}
\Phi_{11} &= {}_{I_k}^{I_{k+1}} \hat{\mathbf{R}} \\
\Phi_{21} &= -[{}^G \hat{\mathbf{p}}_{I_{k+1}} - {}^G \hat{\mathbf{p}}_{I_k} - {}^G \hat{\mathbf{v}}_{I_k} \delta t_k - \frac{1}{2} {}^G \mathbf{g} \delta t_k^2] {}_{I_k}^G \hat{\mathbf{R}} \\
\Phi_{31} &= -[{}^G \hat{\mathbf{v}}_{I_{k+1}} - {}^G \hat{\mathbf{v}}_{I_k} - {}^G \mathbf{g} \delta t_k] {}_{I_k}^G \hat{\mathbf{R}} \\
\Phi_{14} &= -\mathbf{J}_r \delta t_k {}_w^I \hat{\mathbf{R}} \hat{\mathbf{D}}_w \\
\Phi_{24} &= {}_{I_k}^G \hat{\mathbf{R}} \Xi_{4w}^I \hat{\mathbf{R}} \hat{\mathbf{D}}_w \\
\Phi_{34} &= {}_{I_k}^G \hat{\mathbf{R}} \Xi_{3w}^I \hat{\mathbf{R}} \hat{\mathbf{D}}_w \\
\Phi_{15} &= \mathbf{J}_r \delta t_k {}_w^I \hat{\mathbf{R}} \hat{\mathbf{D}}_w \hat{\mathbf{T}}_g {}_a^I \hat{\mathbf{R}} \hat{\mathbf{D}}_a \\
\Phi_{25} &= -{}_{I_k}^G \hat{\mathbf{R}} \left(\Xi_{4w}^I \hat{\mathbf{R}} \hat{\mathbf{D}}_w \hat{\mathbf{T}}_g + \Xi_2 \right) {}_a^I \hat{\mathbf{R}} \hat{\mathbf{D}}_a \\
\Phi_{35} &= -{}_{I_k}^G \hat{\mathbf{R}} \left(\Xi_{3w}^I \hat{\mathbf{R}} \hat{\mathbf{D}}_w \hat{\mathbf{T}}_g + \Xi_1 \right) {}_a^I \hat{\mathbf{R}} \hat{\mathbf{D}}_a
\end{aligned}$$

Note that $\mathbf{J}_r \triangleq \mathbf{J}_r(\hat{\theta}_{k,k+1})$. The Φ_{in} is:

$$\Phi_{in} = \begin{bmatrix} \Phi_{in11} & \Phi_{in12} & \Phi_{in13} & \Phi_{in14} \\ \Phi_{in21} & \Phi_{in22} & \Phi_{in23} & \Phi_{in24} \\ \Phi_{in31} & \Phi_{in23} & \Phi_{in33} & \Phi_{in34} \\ \mathbf{0}_3 & \mathbf{0}_3 & \mathbf{0}_3 & \mathbf{0}_3 \\ \mathbf{0}_3 & \mathbf{0}_3 & \mathbf{0}_3 & \mathbf{0}_3 \end{bmatrix} \quad (195)$$

where we have:

$$\begin{aligned}
\Phi_{in11} &= \mathbf{J}_r \delta t_k {}_w^I \hat{\mathbf{R}} \mathbf{H}_{D_w} \\
\Phi_{in21} &= -{}_{I_k}^G \hat{\mathbf{R}} \Xi_{4w}^I \hat{\mathbf{R}} \mathbf{H}_{D_w} \\
\Phi_{in31} &= -{}_{I_k}^G \hat{\mathbf{R}} \Xi_{3w}^I \hat{\mathbf{R}} \mathbf{H}_{D_w} \\
\Phi_{in12} &= -\mathbf{J}_r \delta t_k {}_w^I \hat{\mathbf{R}} \hat{\mathbf{D}}_w \hat{\mathbf{T}}_g {}_a^I \hat{\mathbf{R}} \mathbf{H}_{D_a} \\
\Phi_{in22} &= {}_{I_k}^G \hat{\mathbf{R}} \left(\Xi_2 + \Xi_{4w}^I \hat{\mathbf{R}} \hat{\mathbf{D}}_w \hat{\mathbf{T}}_g \right) {}_a^I \hat{\mathbf{R}} \mathbf{H}_{D_a} \\
\Phi_{in32} &= {}_{I_k}^G \hat{\mathbf{R}} \left(\Xi_1 + \Xi_{3w}^I \hat{\mathbf{R}} \hat{\mathbf{D}}_w \hat{\mathbf{T}}_g \right) {}_a^I \hat{\mathbf{R}} \mathbf{H}_{D_a} \\
\Phi_{in13} &= -\mathbf{J}_r \delta t_k {}_w^I \hat{\mathbf{R}} \hat{\mathbf{D}}_w \mathbf{H}_{T_g} \\
\Phi_{in23} &= {}_{I_k}^G \hat{\mathbf{R}} \Xi_{4w}^I \hat{\mathbf{R}} \hat{\mathbf{D}}_w \mathbf{H}_{T_g} \\
\Phi_{in33} &= {}_{I_k}^G \hat{\mathbf{R}} \Xi_{3w}^I \hat{\mathbf{R}} \hat{\mathbf{D}}_w \mathbf{H}_{T_g} \\
\Phi_{in14} &= \mathbf{J}_r \delta t_k {}_w^I \hat{\mathbf{R}} \hat{\mathbf{D}}_w \hat{\mathbf{T}}_g [{}^I \hat{\mathbf{a}}]_a^I \hat{\mathbf{R}} \\
\Phi_{in24} &= -{}_{I_k}^G \hat{\mathbf{R}} \left(\Xi_2 + \Xi_{4w}^I \hat{\mathbf{R}} \hat{\mathbf{D}}_w \hat{\mathbf{T}}_g \right) [{}^I \hat{\mathbf{a}}]_a^I \hat{\mathbf{R}} \\
\Phi_{in34} &= -{}_{I_k}^G \hat{\mathbf{R}} \left(\Xi_1 + \Xi_{3w}^I \hat{\mathbf{R}} \hat{\mathbf{D}}_w \hat{\mathbf{T}}_g \right) [{}^I \hat{\mathbf{a}}]_a^I \hat{\mathbf{R}}
\end{aligned}$$

The corresponding linearization Jacobians for Eq. (187) are:

$$\frac{\partial \tilde{\mathbf{z}}}{\partial \tilde{\mathbf{x}}} = \begin{bmatrix} \frac{\partial \tilde{\mathbf{z}}_C}{\partial \tilde{\mathbf{x}}} \\ \frac{\partial \tilde{\mathbf{z}}_A}{\partial \tilde{\mathbf{x}}} \\ \frac{\partial \tilde{\mathbf{z}}_G}{\partial \tilde{\mathbf{x}}} \end{bmatrix} = \begin{bmatrix} \mathbf{H}_{CB} & \mathbf{0} & \mathbf{0} & \mathbf{H}_{CC} & \mathbf{H}_{CF} \\ \mathbf{H}_{AB} & \mathbf{H}_{AA} & \mathbf{0} & \mathbf{H}_{AC} & \mathbf{0} \\ \mathbf{H}_{GB} & \mathbf{0} & \mathbf{H}_{GG} & \mathbf{H}_{GC} & \mathbf{0} \end{bmatrix} \quad (196)$$

where \mathbf{H}_{ZX} denotes the Jacobians of measurement Z regarding to state parameter X and are defined as: Jacobians of camera measurements are computed as:

$$\begin{aligned}
\mathbf{H}_{CB} &= \mathbf{H}_{\mathbf{p}_f C}^T \hat{\mathbf{R}}_I^T G \hat{\mathbf{R}}^\top [[G \mathbf{p}_f - G \mathbf{p}_I]_I^T \hat{\mathbf{R}} \quad -\mathbf{I}_3 \quad \mathbf{0}_{3 \times 30}] \\
\mathbf{H}_{CC} &= [\mathbf{H}_{CC_{Ex}} \quad \mathbf{H}_{CC_{in}}] \\
\mathbf{H}_{CF} &= \mathbf{H}_{\mathbf{p}_f C}^T \hat{\mathbf{R}}_I^T G \hat{\mathbf{R}} \\
\mathbf{H}_{CC_{Ex}} &= \mathbf{H}_{\mathbf{p}_f C}^T \hat{\mathbf{R}}_I^T G \hat{\mathbf{R}}^\top [\mathbf{H}_{CC1} \quad \mathbf{H}_{CC2} \quad \mathbf{H}_{CC3} \quad \mathbf{H}_{CC4} \quad \mathbf{H}_{CC5} \quad \mathbf{H}_{CC6}] \\
\mathbf{H}_{CC1} &= \mathbf{0}_{3 \times 7} \\
\mathbf{H}_{CC2} &= \mathbf{0}_{3 \times 4} \\
\mathbf{H}_{CC3} &= [G \mathbf{p}_f - G \mathbf{p}_I - G \mathbf{R}^I \hat{\mathbf{p}}_C] \\
\mathbf{H}_{CC4} &= -I^G \hat{\mathbf{R}} \\
\mathbf{H}_{CC5} &= G \mathbf{v}_I - [G \mathbf{p}_f - G \mathbf{p}_I]_I^T \hat{\mathbf{R}}^I \boldsymbol{\omega} \\
\mathbf{H}_{CC6} &= \frac{m}{M} \mathbf{H}_{CC5} \\
\mathbf{H}_{CC_{in}} &= \frac{\partial \tilde{\mathbf{z}}_C}{\partial \tilde{\mathbf{x}}_{C_{in}}}
\end{aligned}$$

The measurement Jacobians for auxiliary IMU constraints are computed as:

$$\begin{aligned}
\mathbf{H}_{AB} &= \begin{bmatrix} I_a \hat{\mathbf{R}} & \mathbf{0}_3 & \mathbf{0}_3 & \mathbf{0}_3 & \mathbf{0}_3 & \mathbf{0}_{3 \times 21} \\ I^G \hat{\mathbf{R}} [I \hat{\mathbf{p}}_{I_a}] & -\mathbf{I}_3 & \mathbf{0}_3 & \mathbf{0}_3 & \mathbf{0}_3 & \mathbf{0}_{3 \times 21} \end{bmatrix} \\
\mathbf{H}_{AA} &= \begin{bmatrix} -\mathbf{I}_3 & \mathbf{0}_3 & \mathbf{0}_3 & \mathbf{0}_3 & \mathbf{0}_3 & \mathbf{0}_{3 \times 21} \\ \mathbf{0}_3 & \mathbf{I}_3 & \mathbf{0}_3 & \mathbf{0}_3 & \mathbf{0}_3 & \mathbf{0}_{3 \times 21} \end{bmatrix} \\
\mathbf{H}_{AC} &= \begin{bmatrix} \mathbf{I}_3 & \mathbf{0}_3 & -I_a \boldsymbol{\omega} & \mathbf{0}_{3 \times 20} \\ \mathbf{0}_3 & -I^G \hat{\mathbf{R}} & G \mathbf{v}_I + I^G \hat{\mathbf{R}} [I \boldsymbol{\omega}]^T \mathbf{p}_{I_a} & \mathbf{0}_{3 \times 20} \end{bmatrix}
\end{aligned}$$

The measurement Jacobians for auxiliary gyroscope constraints are computed as:

$$\begin{aligned}
\mathbf{H}_{GB} &= \begin{bmatrix} I_g \hat{\mathbf{R}} & \mathbf{0}_3 & \mathbf{0}_3 & \mathbf{0}_3 & \mathbf{0}_3 & \mathbf{0}_{3 \times 6} \end{bmatrix} \\
\mathbf{H}_{GG} &= [-\mathbf{I}_3 \quad \mathbf{0}_3] \\
\mathbf{H}_{GC} &= [\mathbf{0}_{3 \times 7} \quad \mathbf{I}_3 \quad -I_g \hat{\boldsymbol{\omega}} \quad \mathbf{0}_{3 \times 8} \quad \mathbf{0}_{3 \times 8}]
\end{aligned}$$

The k -th row of the observability matrix can be written as:

$$\mathbf{M}_k = \begin{bmatrix} \frac{\partial \tilde{\mathbf{z}}_C}{\partial \tilde{\mathbf{x}}} \\ \frac{\partial \tilde{\mathbf{z}}_A}{\partial \tilde{\mathbf{x}}} \\ \frac{\partial \tilde{\mathbf{z}}_G}{\partial \tilde{\mathbf{x}}} \end{bmatrix} \Phi \tag{197}$$

$$\begin{aligned}
&= \begin{bmatrix} \mathbf{M}_{CB} & \mathbf{0} & \mathbf{0} & \mathbf{M}_{CC} & \mathbf{M}_{CF} \\ \mathbf{M}_{AB} & \mathbf{M}_{AA} & \mathbf{0} & \mathbf{M}_{AC} & \mathbf{0} \\ \mathbf{M}_{GB} & \mathbf{0} & \mathbf{M}_{GG} & \mathbf{M}_{GC} & \mathbf{0} \end{bmatrix} \\
&= \begin{bmatrix} \mathbf{H}_{CB} \Phi_B & \mathbf{0} & \mathbf{0} & \mathbf{H}_{CC} \Phi_C & \mathbf{H}_{CF} \Phi_F \\ \mathbf{H}_{AB} \Phi_B & \mathbf{H}_{AA} \Phi_A & \mathbf{0} & \mathbf{H}_{AC} \Phi_C & \mathbf{0} \\ \mathbf{H}_{GB} \Phi_B & \mathbf{0} & \mathbf{H}_{GG} \Phi_G & \mathbf{H}_{GC} \Phi_C & \mathbf{0} \end{bmatrix} \tag{198}
\end{aligned}$$

By closely inspecting the observability matrix, we have the following Lemma:

Table 2: Degenerate motions with related unobservable parameters for auxiliary IMU and gyroscope.

Motion Types	Auxiliary IMU	Auxiliary Gyroscope
No Rotation	${}^I \mathbf{p}_{I_a}$	${}^I_{I_g} \mathbf{R}$ and t_{d_g}
One-axis Rotation	${}^I \mathbf{p}_{I_a}$ along rot. axis	${}^I_{I_g} \mathbf{R}$ along rot. axis
Constant ${}^I \boldsymbol{\omega}$	${}^I \mathbf{p}_{I_a}$ along rot. axis	${}^I_{I_g} \mathbf{R}$ along rot. axis, t_{d_g}
Constant ${}^I \boldsymbol{\omega}$ and ${}^G \mathbf{v}_I$	${}^I \mathbf{p}_{I_a}$ along rot. axis, t_{d_a}	${}^I_{I_g} \mathbf{R}$ along rot. axis, t_{d_g}
Constant ${}^I \boldsymbol{\omega}$ and ${}^I \mathbf{v}$	${}^I \mathbf{p}_{I_a}$ along rot. axis	${}^I_{I_g} \mathbf{R}$ along rot. axis, t_{d_g}

Lemma 1. *The proposed MVIS has four unobservable directions corresponding to the global yaw rotation and the global translation:*

$$\mathbf{N} = \begin{bmatrix} {}^{I_1} \mathbf{R}^G \mathbf{g} & \mathbf{0}_3 \\ [{}^G \mathbf{p}_{I_1}]^G \mathbf{g} & \mathbf{I}_3 \\ [{}^G \mathbf{v}_{I_1}]^G \mathbf{g} & \mathbf{0}_3 \\ \mathbf{0}_{27 \times 1} & \mathbf{0}_{27 \times 3} \\ {}^{I_{a1}} \mathbf{R}^G \mathbf{g} & \mathbf{0}_3 \\ [{}^G \mathbf{p}_{I_{a1}} - {}^G \mathbf{p}_{I_1}]^G \mathbf{g} & \mathbf{I}_3 \\ [{}^G \mathbf{v}_{I_{a1}} - {}^G \mathbf{v}_{I_1}]^G \mathbf{g} & \mathbf{0}_3 \\ \mathbf{0}_{27 \times 1} & \mathbf{0}_{27 \times 3} \\ {}^{I_{g1}} \mathbf{R}^G \mathbf{g} & \mathbf{0}_3 \\ \mathbf{0}_{36 \times 1} & \mathbf{0}_{36 \times 3} \\ [{}^G \mathbf{p}_f]^G \mathbf{g} & \mathbf{I}_3 \end{bmatrix} \quad (199)$$

These four unobservable directions are similar to the 4 classical unobservable directions for a monocular VINS system [52]. From this lemma, we can conclude that the system observability will not be improved by simply adding more inertial sensors (IMU or gyroscopes). It should also be pointed out that the velocity of IMU state will become unobservable if no visual measurements to static landmarks are available. Hence, without cameras, naively adding auxiliary IMUs will not significantly improve the system localization accuracy due to lack of global constraints to the base IMU velocity. It can be observed that the calibration parameters, including \mathbf{x}_{in} , $\mathbf{x}_{A_{in}}$, $\mathbf{x}_{G_{in}}$ and \mathbf{x}_{Ex} , are highly related to the sensor motion. Under fully excited motions, these parameters are observable, which can be seen from our simulation results in Section 10.1.

9 Degenerate Motion Analysis

While the degenerate motions for the IMU-camera spatiotemporal parameters, IMU intrinsics and camera intrinsics have been studied [50, 34, 9], in this paper, we for the first time study the degenerate motions for the IMU-IMU/Gyroscope spatiotemporal calibration of MVIS.

9.1 Spatiotemporal Calibration of Auxiliary Inertial Sensors

In particular, we have identified the degenerate motions for the spatiotemporal calibration between the auxiliary inertial sensors and the base IMU, as summarized in Table 2, which will be explained in detail below.

9.1.1 No Rotation

If the MVIS undergoes 3D motion but without rotation, the translation ${}^I\mathbf{p}_{I_a}$ between the auxiliary and base IMUs, the rotation ${}^I_{I_g}\mathbf{R}$ and time offset between the auxiliary gyroscope and the base IMU, will be unobservable. The unobservable directions \mathbf{N}_{NR} are given by:

$$\mathbf{N}_{NR} = \begin{bmatrix} \mathbf{0}_{39 \times 3} & \mathbf{0}_{39 \times 3} & \mathbf{0}_{39 \times 1} \\ \mathbf{I}_3 & \mathbf{0}_3 & \mathbf{0}_{3 \times 1} \\ \mathbf{0}_{30 \times 3} & \mathbf{0}_{30 \times 3} & \mathbf{0}_{30 \times 1} \\ \mathbf{0}_3 & \mathbf{I}_3 & \mathbf{0}_{3 \times 1} \\ \mathbf{0}_{12 \times 3} & \mathbf{0}_{12 \times 3} & \mathbf{0}_{12 \times 1} \\ {}^{I_1}_{G}\mathbf{R} & \mathbf{0}_3 & \mathbf{0}_{3 \times 1} \\ \mathbf{0}_{1 \times 3} & \mathbf{0}_{1 \times 3} & 0 \\ \mathbf{0}_3 & \mathbf{I}_3 & \mathbf{0}_{3 \times 1} \\ \mathbf{0}_{1 \times 3} & \mathbf{0}_{1 \times 3} & 1 \\ \mathbf{0}_{19 \times 3} & \mathbf{0}_{19 \times 3} & \mathbf{0}_{19 \times 1} \end{bmatrix} \quad (200)$$

9.1.2 One-Axis Rotation

If the system undergoes 3D motion but with only one-axis rotation (which is common for aerial and ground vehicles), the translation ${}^I\mathbf{p}_{I_a}$ between the auxiliary and base IMUs, the rotation ${}^I_{I_g}\mathbf{R}$ between the auxiliary gyroscope and the base IMU will be unobservable, along with the rotation axis \mathbf{k} . Specifically the additional unobservable directions are given by:

$$\mathbf{N}_{OA} = \begin{bmatrix} \mathbf{0}_{39 \times 1} & \mathbf{0}_{39 \times 1} \\ {}^{G}\mathbf{R} {}^{I_1}\mathbf{k} & \mathbf{0}_{3 \times 1} \\ \mathbf{0}_{30 \times 1} & \mathbf{0}_{30 \times 1} \\ \mathbf{0}_{3 \times 1} & {}^{I_g}\mathbf{k} \\ \mathbf{0}_{12 \times 1} & \mathbf{0}_{12 \times 1} \\ {}^{I_0}\mathbf{k} & \mathbf{0}_{3 \times 1} \\ 0 & 0 \\ \mathbf{0}_{3 \times 1} & {}^{I_g}\mathbf{k} \\ 0 & 0 \\ \mathbf{0}_{19 \times 1} & \mathbf{0}_{19 \times 1} \end{bmatrix} \quad (201)$$

Note that we, for the first time, explicitly found that one-axis rotation will cause the rotation calibration between the auxiliary gyroscope and base IMU to become unobservable. We verify this finding with simulations in Section 10.2.

9.1.3 Constant Local Angular Velocity

If the MVIS undergoes constant local angular velocity with random 3D translation for the base IMU, the translation ${}^I\mathbf{p}_{I_a}$ between the base and auxiliary IMUs is still unobservable along the rotation axis. In addition, the rotation ${}^I_{I_a}\mathbf{R}$ and the time offset t_{I_g} between the base IMU and the auxiliary gyroscope become unobservable.

9.1.4 Constant Local Angular and Global Linear Velocity

If the MVIS undergoes constant ${}^I\boldsymbol{\omega}$ and constant ${}^G\mathbf{v}_I$ for base IMU, the translation and time offsets between the base and auxiliary IMUs, the rotation and time offset between the base IMU and the auxiliary gyroscope become unobservable.

Table 3: Summary of basic degenerate motions for auxiliary inertial intrinsics calibration. Any combinations of these unit motion primitives are degenerate. Note that d_{A*} is column-wise element from \mathbf{D}_{A*} , with d_{Gw} is column-wise element from \mathbf{D}_{Gw} . $t_{Agi}, i = 1 \dots 9$ are the elements from \mathbf{T}_{Ag} for g-sensitivity.

Motion Types	Nullspace Dim.	Unobservable Parameters
constant $A_w\omega_1$	1	$d_{A_{w1}}$
constant $A_w\omega_2$	2	$d_{A_{w2}}, d_{A_{w3}}$
constant $A_w\omega_3$	3	$d_{A_{w4}}, d_{A_{w5}}, d_{A_{w6}}$
constant $A_a a_1$	3	$d_{A_{a1}}$, pitch and yaw of $I_a \mathbf{R}$
constant $A_a a_2$	3	$d_{A_{a2}}, d_{A_{a3}}$, roll of $I_a \mathbf{R}$
constant $A_a a_3$	3	$d_{A_{a4}}, d_{A_{a5}}, d_{A_{a6}}$
constant $I_a a_1$	1	$t_{A_{g1}}, t_{A_{g2}}, t_{A_{g3}}$
constant $I_a a_2$	2	$t_{A_{g4}}, t_{A_{g5}}, t_{A_{g6}}$
constant $I_a a_3$	3	$t_{A_{g7}}, t_{A_{g8}}, t_{A_{g9}}$
constant $G_w\omega_1$	1	$d_{G_{w1}}$
constant $G_w\omega_2$	2	$d_{G_{w2}}, d_{G_{w3}}$
constant $G_w\omega_3$	3	$d_{G_{w4}}, d_{G_{w5}}, d_{G_{w6}}$

9.1.5 Constant Local Angular and Linear Velocity

When the $I\boldsymbol{\omega}$ and $I\mathbf{v}$ are constant for the base IMU, the time offset t_d between the base IMU and camera, as well as the time offset t_{dg} between the base IMU and the gyroscope are both unobservable. However, the time offset t_{da} between the base and auxiliary IMUs is still observable (see Fig. 6), which is unexpected. This is due to the fact that the local constant velocity assumption will be invalid for the auxiliary IMU if the base IMU is undergoing constant local linear and angular velocity. The local angular velocity and acceleration of the auxiliary IMU can be represented as:

$$I_a \boldsymbol{\omega} = I_a \mathbf{R}^I \boldsymbol{\omega} \quad (202)$$

$$I_a \mathbf{a} = I_a \mathbf{R} (I \mathbf{a} + [I \boldsymbol{\alpha}]^I \mathbf{p}_{Ia} + [I \boldsymbol{\omega}]^I \mathbf{p}_{Ia}) \quad (203)$$

where $I \boldsymbol{\alpha}$ refers to the angular acceleration of the base IMU. If the base IMU undergoes constant local linear and angular velocity motion, the angular velocity of the auxiliary IMU $I_a \boldsymbol{\omega}$ is also constant [see Eq. (202)]. The $I \mathbf{a}$ and $I \boldsymbol{\alpha}$ of the base IMU should be zeros. Hence, Eq. (203) yields:

$$I_a \mathbf{a} = I_a \mathbf{R} ([I \boldsymbol{\omega}] [I \boldsymbol{\omega}]^I \mathbf{p}_{Ia}) \quad (204)$$

If $I \boldsymbol{\omega}$ is constant but not zero, the local linear acceleration $I_a \mathbf{a}$ should not be zero. This breaks the local constant linear velocity assumption for the auxiliary IMU. Furthermore, we find that the norm of $I_a \mathbf{v}$ is constant:

$$I_a \mathbf{v} = I_a \mathbf{R} (I \mathbf{v} + [I \boldsymbol{\omega}]^I \mathbf{p}_{Ia}) \quad (205)$$

But the non-zero acceleration $I_a \mathbf{a}$ will cause the bearing change of local velocity, which makes the time offset between the base and auxiliary IMUs observable. This is further verified through our simulation results (see Fig. 6).

9.2 Intrinsics for Auxiliary Inertial Sensors

In our previous work [34, 9], the degenerate motions of IMU intrinsics for monocular VINS have been studied. In this work, we have found that the degenerate motion primitives in [9] still hold for the auxiliary IMU intrinsics with our inertial model choice (see Table 3). Note that fully excited motions are needed in order to make all intrinsic parameters observable for the auxiliary IMUs/gyroscopes.

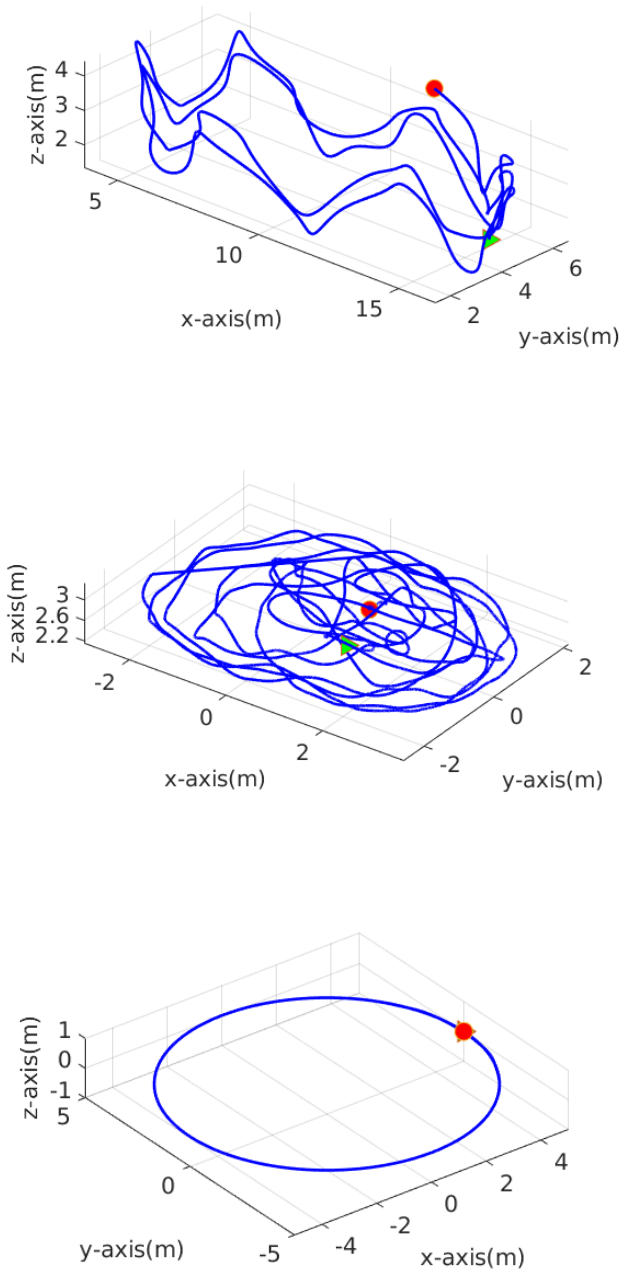


Figure 2: Simulated trajectories. Top: *calib_3d* with fully excited 3D motion, total length: 89.4 m; Middle: *tum_room* with 1 axis rotation and 3D translation, total length: 134.5 m; Bottom: *circle_planar* with circular planar motion (constant z and only yaw rotation), total length: 157.1 m. The green triangle and red circle denote the beginning and ending of these trajectories, respectively.

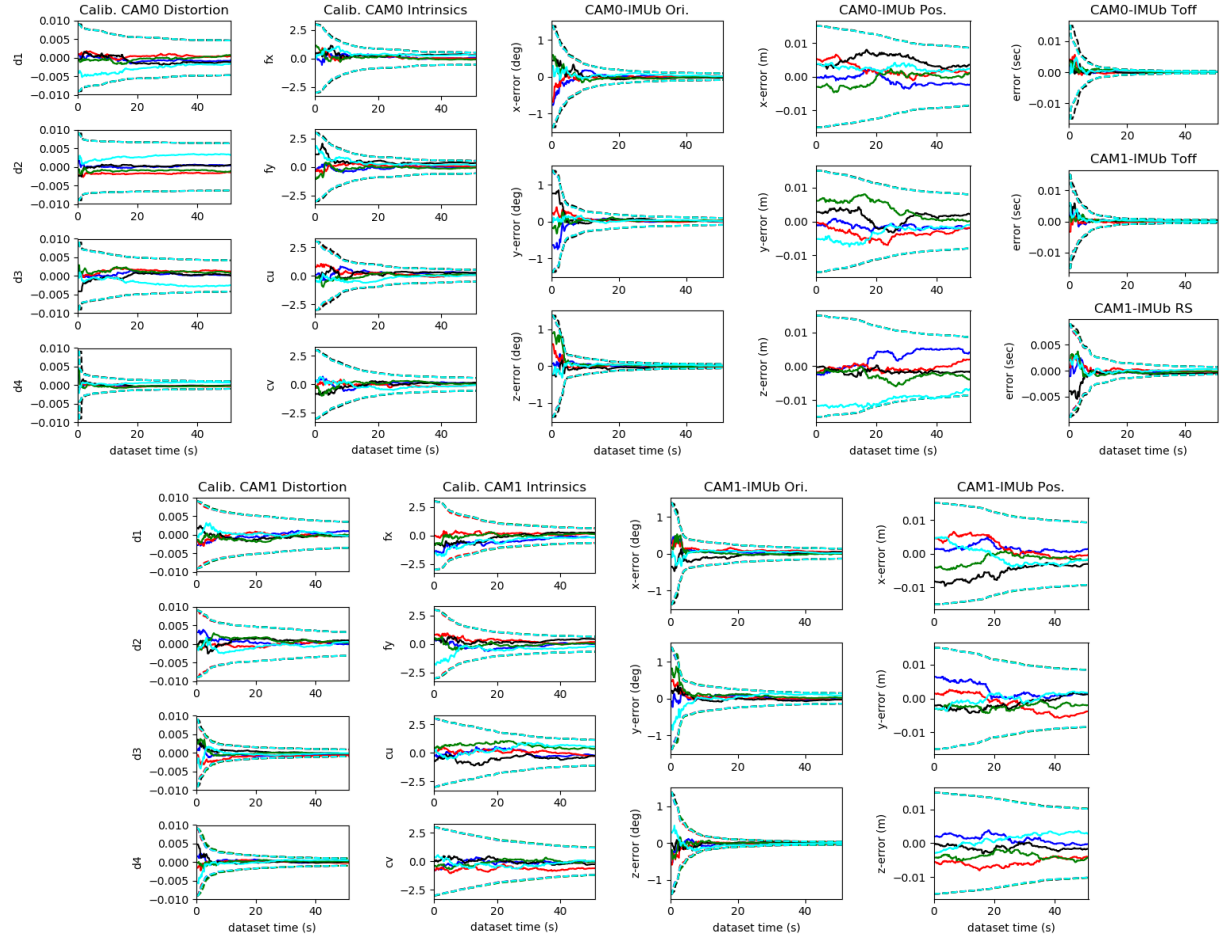


Figure 3: Simulation results for *fully-excited motion*. All the cameras (CAM0 and CAM1) related parameters converge nicely. 3σ bounds (dashed line) and estimation errors (solid line) are plotted for five different runs (shown in different colors) with different initial calibration perturbations.

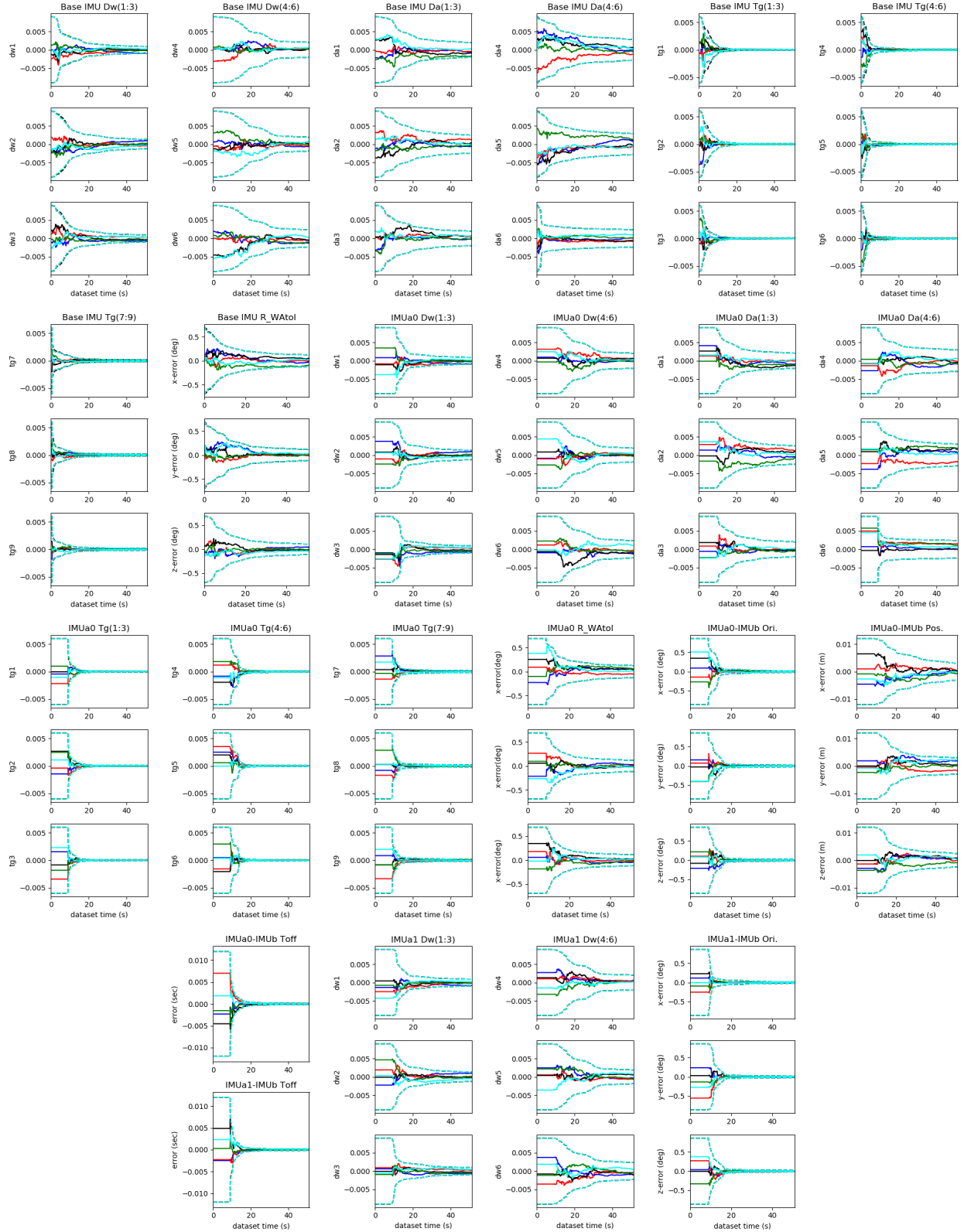


Figure 4: Simulation results for *fully-excited motion*. All the base IMU (**IMUb**) and auxiliary IMUs (**IMUa0**, **IMUa1**) related parameters converge nicely. 3σ bounds (dashed line) and estimation errors (solid line) are plotted for five different runs (shown in different colors) with different initial calibration perturbations.

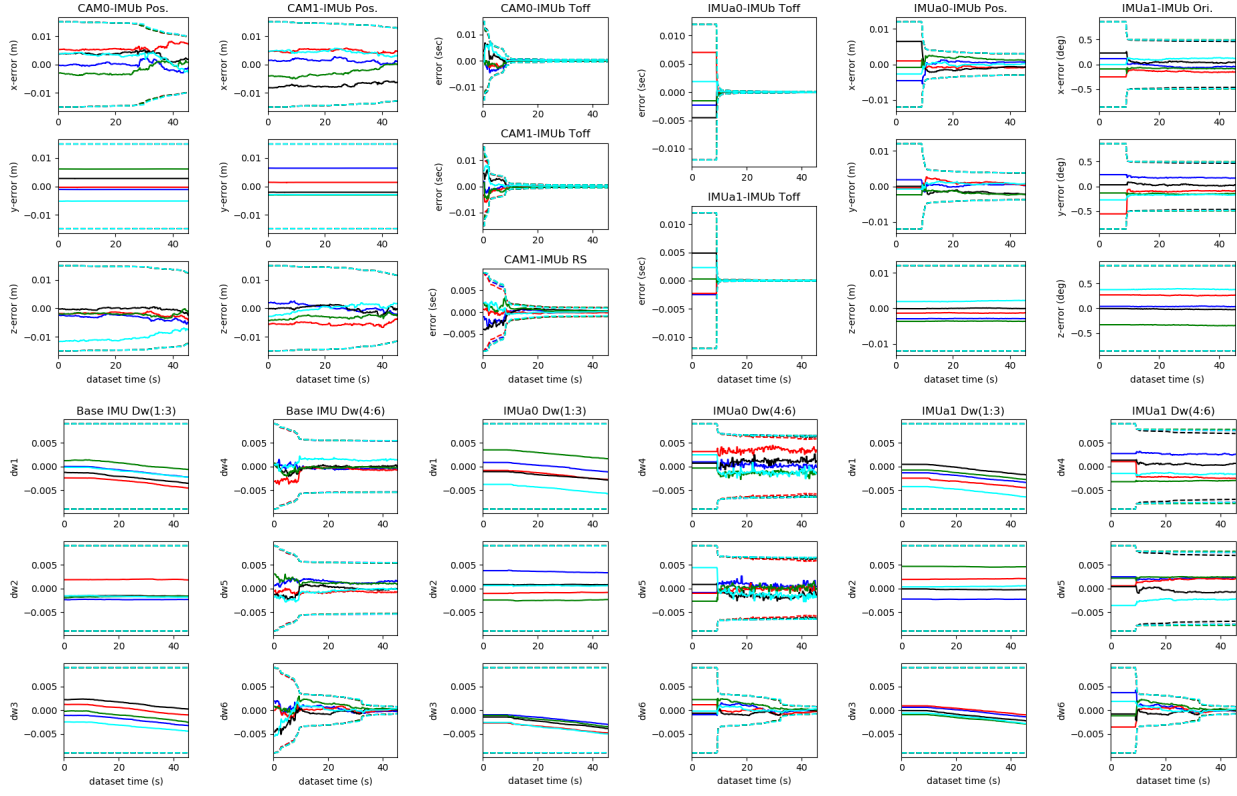


Figure 5: Simulation results for *One-axis motion*. The translation of **CAM0-IMUb** (y component) and **IMUa0-IMUb** (z component), the rotation of **IMUa1-IMUb** (z component), the d_{w1} , d_{w2} and d_{w3} of **IMUb**, **IMUa0** and **IMUa1** show inability to converge (sigma bound does not decrease due to no information gain). 3σ bounds (dashed line) and estimation errors (solid line) are plotted for five different runs (shown in different colors) with different initial calibration perturbations.

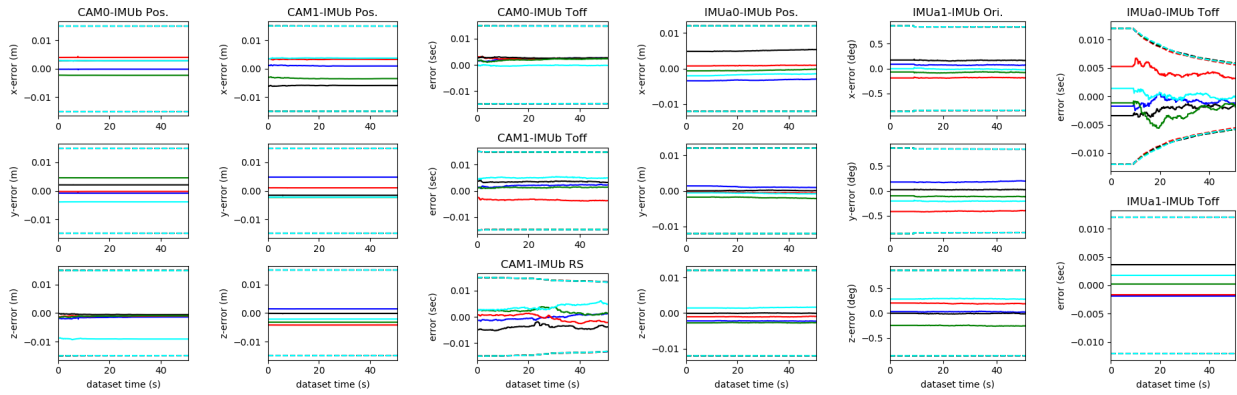


Figure 6: Simulation results for *Circular-planar motion*. The translation of **CAM0-IMUb**, **CAM1-IMUb**, **IMUa0-IMUb**, the rotation of **IMUa1-IMUb**, the time offset of **CAM0-IMUb**, **CAM1-IMUb** and **IMUa1-IMUb** all show inability to converge (sigma bound does not decrease due to no information gain). Note that the RS readout time of **CAM1** and the time offset of **IMUa0-IMUb** converge slower due to less motion excitation. 3σ bounds (dashed line) and estimation errors (solid line) are plotted for five different runs (shown in different colors) with different initial calibration perturbations.

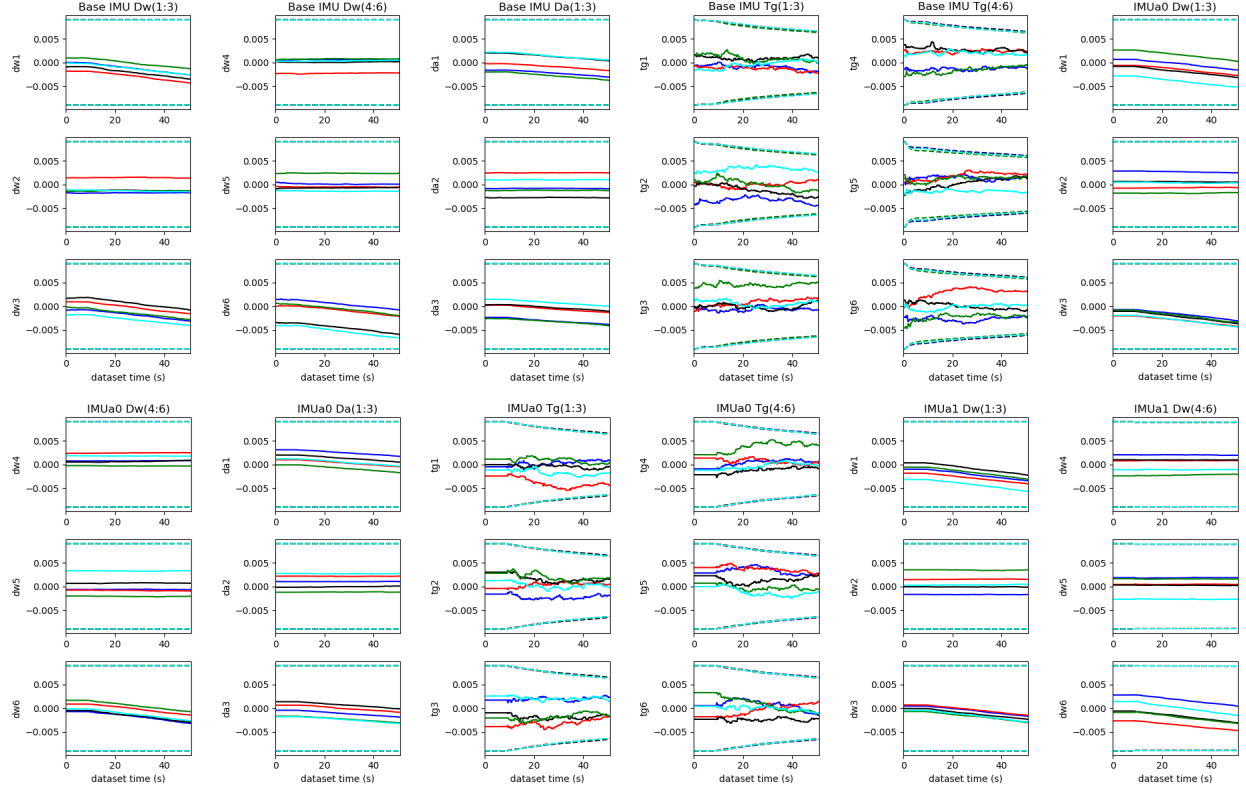


Figure 7: Simulation results for *Circular-planar motion*. The gyroscope and acceleration related parameters (\mathbf{D}_w , \mathbf{D}_a and \mathbf{T}_g) for both base and auxiliary IMUs do not converge or converge much slower than the case of fully-excited motions. 3σ bounds (dashed line) and estimation errors (solid line) are plotted for five different runs (shown in different colors) with different initial calibration perturbations.

Table 4: Simulation parameters and prior standard deviations that perturbations of measurements and initial states were drawn from.

Parameter	Value	Parameter	Value
IMU Dw	0.003	IMU Da	0.003
Rot. atoI (rad)	0.003	IMU Tg	0.001
Gyro. Noise ($\text{rad s}^{-1} \sqrt{\text{Hz}^{-1}}$)	1.696e-04	Gyro. Bias ($\text{rad s}^{-2} \sqrt{\text{Hz}^{-1}}$)	1.939e-05
Accel. Noise ($\text{m s}^{-2} \sqrt{\text{Hz}^{-1}}$)	2.000e-3	Accel. Bias ($\text{m s}^{-3} \sqrt{\text{Hz}^{-1}}$)	3.000e-3
Focal Len. (px/m)	1.0	Cam. Center (px)	1.0
d1 and d2	0.002	d3 and d4	0.002
Rot. CtoI (Hz)	0.004	Pos. IinC (m)	0.008
Pixel Proj. (px)	1	Cam-IMU Timeoff (s)	0.008
IMU-IMU Timeoff (s)	0.003	Gyro-IMU Timeoff (s)	0.003
Rot. AItobi (rad)	0.003	Pos. IainIb (m)	0.005
Cam Freq. (Hz)	10/10	IMU Freq. (Hz)	250/300/200

10 Simulation Results

The simulator, which is provided within the OpenVINS project [6] along with the multi-IMU and RS extension from [8] and IMU intrinsic extension [9], is leveraged to provide synthetic measurements with perfect groundtruth for verification of the proposed MVIS under different motion conditions. In the simulation, one base IMU **IMUb**, one auxiliary IMU **IMUa0**, one auxiliary gyroscope **IMUa1**, one global shutter (GS) camera **CAM0** and one rolling shutter (RS) camera **CAM1** are simulated. Note that both cameras are simulated with 10hz frame rates. The basic configuration of the simulator is listed in Table 4. The three trajectories used for the simulation Fig. 2 are as follows:

- Fully-excited motion (left of Fig. 2): All axes of the accelerometer and gyroscope are fully excited with a general 3D handheld trajectory.
- One-axis motion (middle of Fig. 2): The sensor suite moves in 3D space but with only yaw rotation. The trajectory is modified based on *tum_room1* from [33].
- Circular-planar motion (right of Fig. 2): The sensor suite moves in x-y plane with constant local angular and linear velocities.

Specifically, we first build a B-spline with trajectory keyframes of the base IMU trajectory. Then, we can compute the acceleration of base IMU by calculating double derivatives for the position component of the B-spline at specified time stamp. We leverage rigid body constraints between base and auxiliary IMU to simulate the auxiliary IMU readings. The base IMU acceleration can be transferred to the auxiliary IMU frame with the groundtruth angular velocity and acceleration, which are also computed from derivatives of base IMU B-spline. The angular velocity of the auxiliary IMU can be simply computed with angular velocity from base IMU and the rigid rotation between base IMU and auxiliary IMU. Then white Gaussian noises are added to the auxiliary IMU readings based on Eq. (1) and (2).

To simulate RS visual bearing measurements, we follow the same logic in [54, 8, 9]. Static environmental features are first generated along the trajectory at random depths and bearings. Then, for a given imaging time, we project each feature in view into the current image frame using the true camera intrinsic and distortion model and find the corresponding observation row. Given

this projected row and image time, we can find the pose at which that RS row should have been exposed. We can then re-project this feature into the new pose and iterate until the projected row does not change (which typically requires 2-3 iterations). We now have a feature measurement which occurs at the correct pose given its RS row. This measurement is then corrupted with white noise. The imaging timestamp corresponding to the starting row is then shifted by the true IMU-Camera time offset t_d to simulate cross-sensor delay. In the following simulations, the RPNG IMU model [see Section 3.1] is used to be aligned with the analysis.

10.1 Fully-Excited Motion

We first evaluate the proposed system on a general 3D handheld trajectory, see Fig. 2, which fully excites all 6 axes of the sensor platform. To save space, only selected parameters are presented, but all parameters are perturbed and estimated during our simulation runs. The camera related results are shown in Fig. 3 while the IMU related results are shown in Fig. 4. For each figure, there are five different runs with different initial state perturbations.

It is clear that all parameters are able to converge towards the true value within the first 20-40 seconds of the trajectory, which verifies our conclusion that all the calibration parameters for MVIS are observable given fully-excited motions. These results also verify that the proposed MVIS indeed is able to perform calibration of all parameters for visual and inertial sensors.

10.2 Degenerate One-Axis Motion

We now perform a simulation where the trajectory only exhibits one-axis rotation about the global z-axis to verify our identified degenerate motion, see Fig. 2. Shown in Fig. 5, multiple parameters are unable to converge with either estimation errors or estimation uncertainties (3σ bounds). This matches the parameters which we have identified as unobservable under this motion. We can see that the 3 parameters d_{w1} , d_{w2} and d_{w3} for both the base IMU IMUb , auxiliary IMU IMUa0 , and auxiliary gyroscope IMUa1 are unable to be calibrated. Additionally, the y component for the rigid position between the camera to base IMU (CAM0-IMUb Pos.) cannot converge at all. The z component for the position of the auxiliary IMU to base IMU (IMUa0-IMUb Pos.) is unable to be calibrated as expected. Note that the y component of ${}^I\mathbf{p}_C$ and the z component of ${}^I\mathbf{p}_{I_a}$ are all along the rotation axis which is degenerate.

Furthermore, it can be seen that we are unable to calibrate a portion of the relative rotation between the base IMU and auxiliary gyroscope (IMUa1-IMUb Ori.) due to one-axis rotation, which can be calibrated nicely in the fully-excited motion case. This further confirms our degenerate motion analysis summarized in Table 2.

10.3 Degenerate Circular-Planar Motion

We also perform a simulation where the sensors follow a circular-planar motion shown in Fig. 2. This is a typical example motion of constant angular and linear velocity. The translation and the time offset of CAM0-IMUb , CAM1-IMUb , the translation of IMUa0-IMUb and the orientation of IMUa1-IMUb are not observable. Shown in Fig. 6, their 3σ bounds and estimate errors are kept as almost straight lines and do not converge at all. These results further verifies our identified degenerate motions shown in Table 2.

The time offset between auxiliary gyroscope and based IMU (IMUa1-IMUb Toff) also are unable to be calibrated, while the time offset between auxiliary IMU to base IMU (IMUa0-IMUb Toff) is still observable. This can be seen by the estimation errors converging in Fig. 6 and thus verifies our

degenerate motion analysis in Section 9.1.5. Note that the rolling shutter readout time of the CAM1 converges quite slowly, given that the sensor motion is not fully excited.

The calibration results for IMU related intrinsics are shown in Fig. 7. It is clear that the gyroscope related parameters \mathbf{D}_w and the accelerometer related parameters \mathbf{D}_a do not converge at all. The convergence of g-sensitivity \mathbf{T}_g also becomes much worse compared to fully excited motion in Fig. 4 which results from fully-excited motions.

11 Experimental Results

The proposed self-calibration system is further evaluated using our own visual-inertial sensor rig (VI-Rig) as shown in Fig. 8. Specifically, it contains a MS-GX-25, MS-GX-35, Xsens MTi 100, FLIR blackfly camera, RealSense T265 tracking camera (which contains an integrated BMI055 IMU along with a fisheye stereo global shutter camera), and 640x480 ELP-960P2CAM-V90-VC USB 2.0 RS-stereo camera. We perform three sets of experiments².

- Fully-excited motion with 4 IMUs + 3 GS Cameras.
- Fully-excited motion with 4 IMUs + 2 GS Cameras + 2 RS Cameras.
- Planar motion with 4 IMUs + 2 GS cameras.

In these experiments, we evaluate the intrinsic calibration with Kalibr model [see Section 3.1], in order to facilitate a direct comparison to Kalibr—the calibration toolbox [21]. We also investigate if the joint calibration performance changes with different number of IMU/Camera sets. In addition, planar motion, one of the most commonly seen degenerate motions, is also investigated to show its effects on calibration. The results further verify our degeneration motion analysis and has significant practical implications on practitioners performing calibration on constrained autonomous platforms (e.g. aerial or ground vehicles).

The boxplots are used to demonstrate the calibration results for the proposed MVIS and Kalibr. When drawing the boxplots for the translation part of extrinsics, the camera intrinsics and time offsets, we use the average estimates of the MVIS with all available sensors as reference value and then compute the error of each estimate from Kalibr or MVIS to this reference. When drawing the boxplots for the orientation extrinsic, we select the first estimate of MVIS with all available sensors for reference value. The middle line of each boxplot indicates the average errors while the red star + indicates outliers. IMU intrinsics are computed relative to the “ideal” inertial model, with identity for all matrices except for g-sensitivity, which is set as all zeros.

11.1 4 IMUs + 3 GS Cameras

All the four IMUs, FLIR blackfly camera and the GS stereo camera from RealSense T265 are used for this evaluation. All cameras used in this experiments are not rolling shutter to ensure fair comparison against the baseline Kalibr [21] which only supports IMU-Camera calibration with global shutter cameras. Total 10 datasets were collected with an AprilTag board, on which both the proposed system and the Kalibr calibration toolbox were run to evaluate the calibration accuracy and repeatability statistics on all calibration parameters. During data collection, all 6-axis motion of the VI-Rig were excited to avoid degenerate motions for calibration parameters.

²Datasets are available at <https://openmvis.com/>.

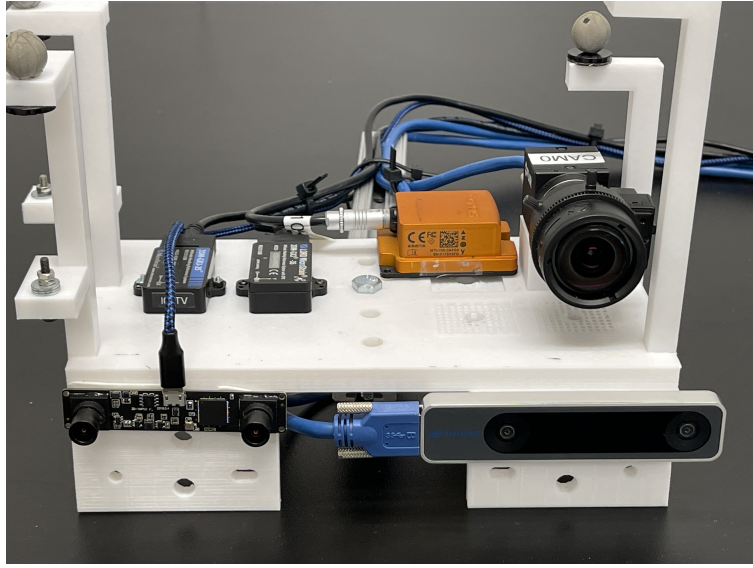


Figure 8: The self-assembled sensor rigs in real-world experiments, containing one Microstrain GX-25, one Microstrain GX-35, one MTI Xsens IMU, one BalckFly camera, one IntelRealsense T265 tracking camera (with a GS fisheye stereo camera and an BMI055 IMU inside) and one ELP stereo RS camera.

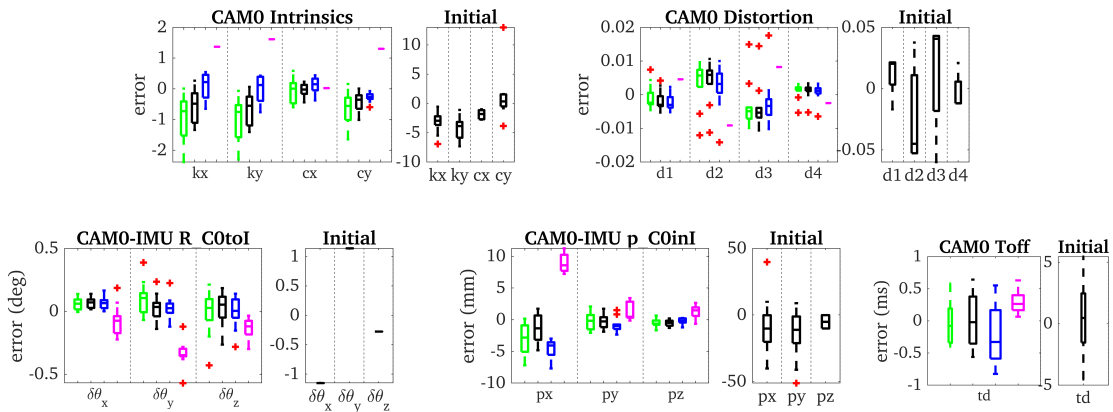


Figure 9: Calibration Results for CAM0 and four IMUs related parameters over 10 datasets collected with Intel Realsense T265 (GS), FLIR Blackfly camera (GS) and four IMUs. The proposed MVIS was run with one (green), two (black), and three (blue) of the cameras. The baseline Kalibr (magenta) was run on all three cameras and all four IMUs. Note that the calibration convergence of camera intrinsics and camera to IMU translation are improved if more cameras are used.

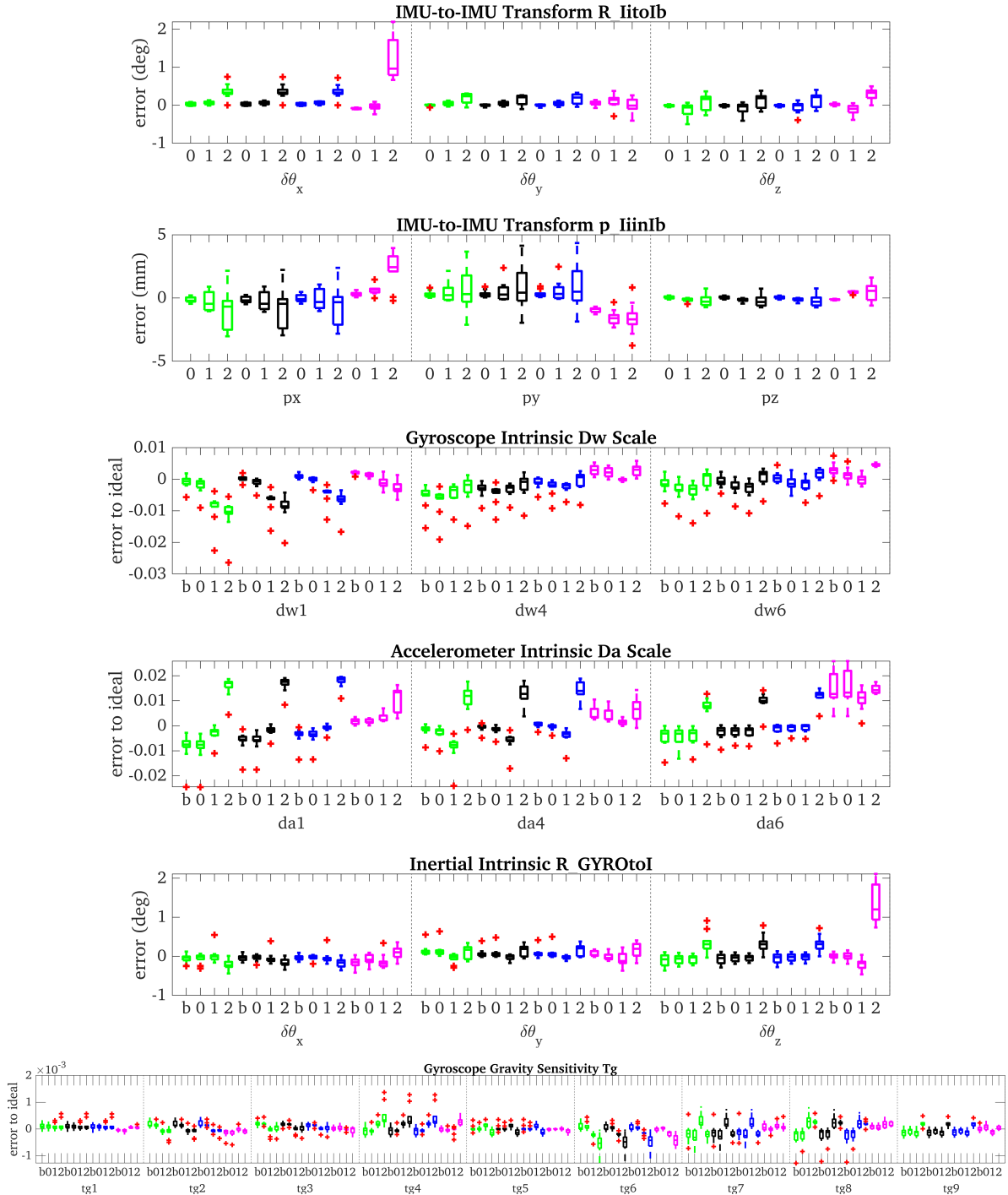


Figure 10: Calibration Results for CAM0 and four IMUs related parameters over 10 datasets collected with Intel Realsense T265 (GS), FLIR Blackfly camera (GS) and four IMUs. The proposed MVIS was run with one (green), two (black), and three (blue) of the cameras. The baseline Kalibr (magenta) was run on all three cameras and all four IMUs. The x-axis of figures denotes the base IMU (IMUb) as b and auxiliary IMU (IMUa0-IMUa2) as 0, 1 and 2 respectively. Note that the calibration convergence of IMU intrinsics are improved if more cameras are used.

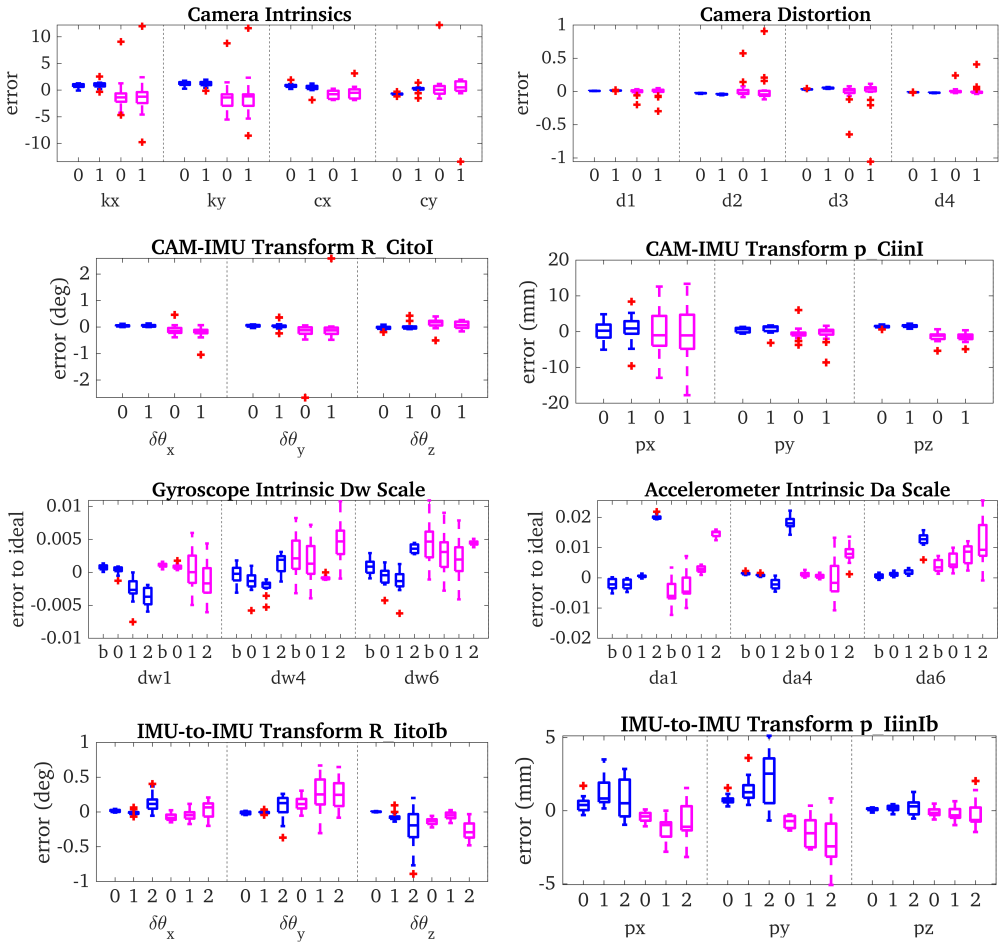


Figure 11: Calibration results over 15 different datasets collected with Intel Realsense T265 (GS), ELP-960P2CAM-V90-VC USB 2.0 (RS, 640x480) and four IMUs. The proposed MVIS (blue, using all the sensors) and Kalibr baseline (magenta, using only T265 cameras with all the IMUs) statistics are reported. The top two x-axis denote the two global shutter cameras (CAM0, CAM1) as 0 and 1, respectively; The bottom two x-axis denotes the base IMU (IMUb) as \mathbf{b} , and auxiliary IMUs (IMUa0, IMUa1 and IMUa2) as 0, 1 and 2, respectively.

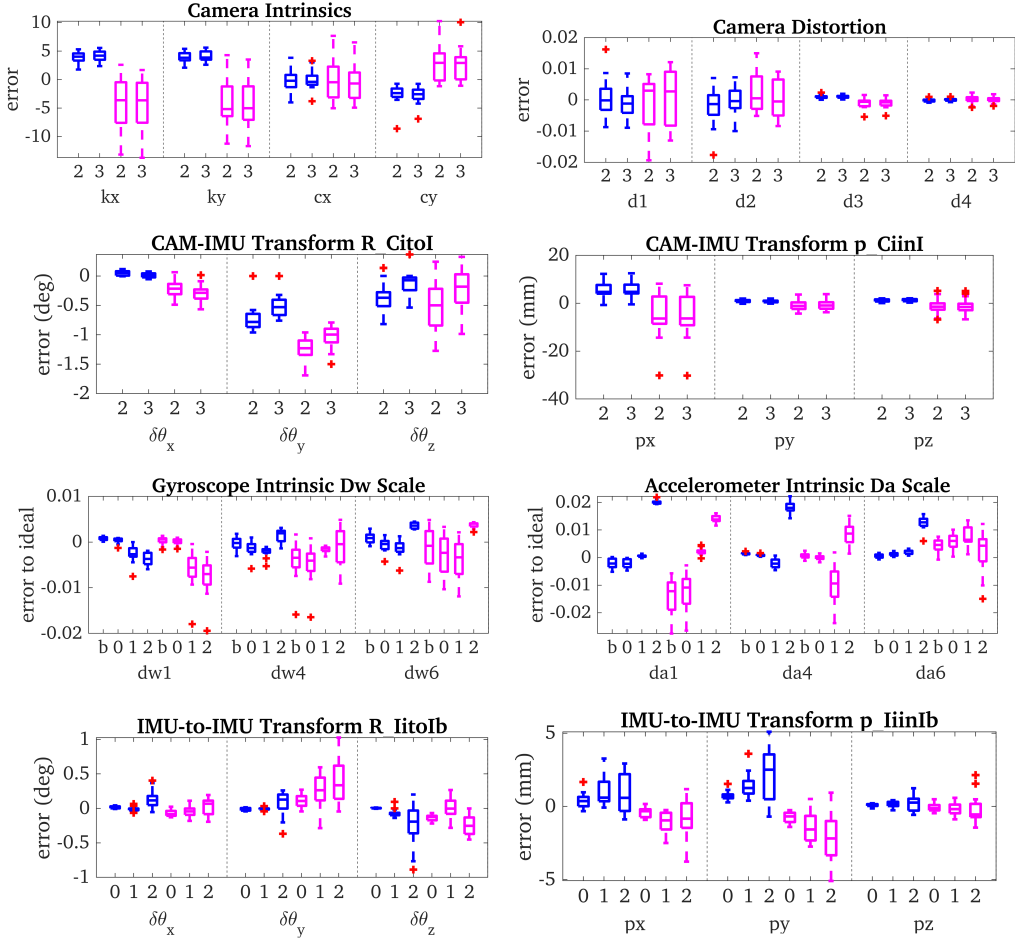


Figure 12: Calibration results over 15 different datasets collected with Intel Realsense T265 (GS), ELP-960P2CAM-V90-VC USB 2.0 (RS, 640x480) and four IMUs. The proposed MVIS (blue, using all the sensors) and Kalibr rolling shutter baseline (magenta, using only the RS cameras with all IMUs) statistics are reported. The top two x-axis denote the two rolling shutter cameras (CAM2, CAM3) as 2 and 3, respectively; The bottom two x-axis denotes the base IMU (IMUb) as b, and auxiliary IMUs (IMUa0, IMUa1 and IMUa2) as 0, 1 and 2.

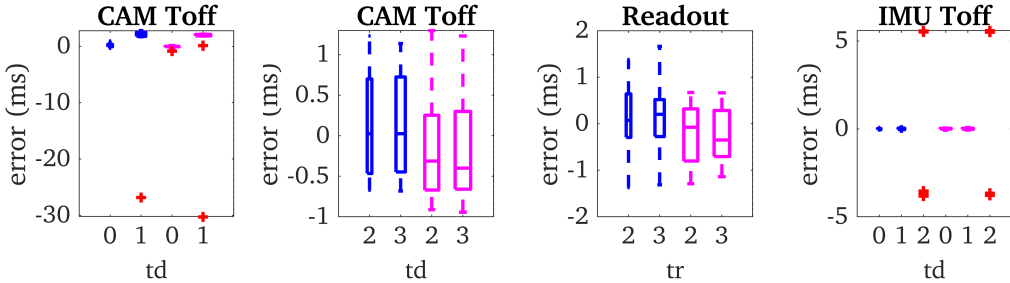


Figure 13: Temporal calibration results over 15 different datasets with Intel Realsense T265 (GS), ELP-960P2CAM-V90-VC USB 2.0 (RS, 640x480) and four IMUs. The proposed MVIS (blue) and Kalibr rolling shutter baseline (magenta) statistics are reported. The x-axis of the left 3 figures denotes the two global shutter camera CAM0, CAM1, two rolling shutter camera CAM2, CAM3. The x-axis of the right figure denotes the time offsets between the base IMU (IMUb), and auxiliary IMUs (IMUa0, IMUa1, IMUa2).

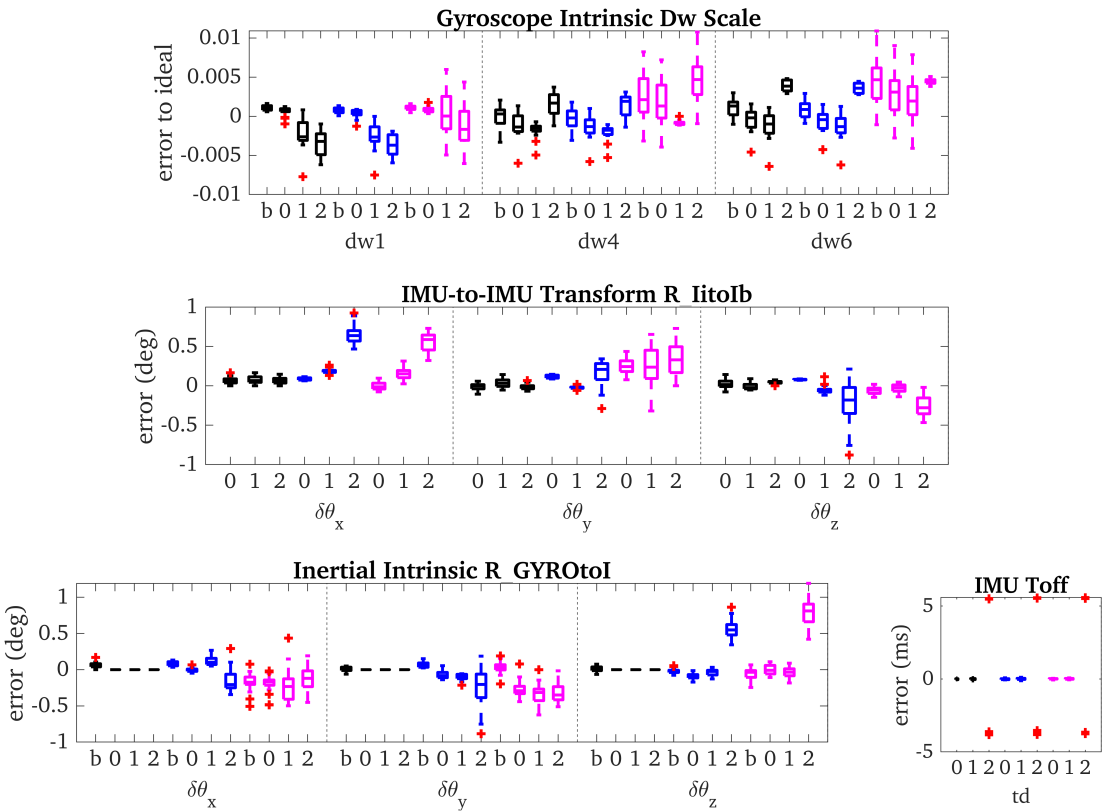


Figure 14: Calibration results over 15 different datasets with Intel Realsense T265 and four IMUs. The proposed MVIS with a base IMU and only gyroscopes of the 3 auxiliary IMUs (black), MVIS with a base IMU and 3 auxiliary IMUs (blue) and Kalibr baseline (magenta) statistics are reported. The x-axis denotes the base IMU (**IMUb**) and auxiliary IMUs (**IMUa0**, **IMUa1**, **IMUa2**) for all algorithms.

11.1.1 Calibration with Different Number of Cameras

When running Kalibr, all the IMUs and cameras are used to achieve the best calibration results from Kalibr. When running our proposed MVIS, we use all the four IMUs with 1/2/3 camera, respectively. In this way, we can evaluate how the number of used cameras affect the calibration performance.

The final converged estimates of the calibration parameters from both systems on these 10 datasets can be shown in the box plots in Fig. 9 and 10. The proposed MVIS was run with one (green), two (black), and three (blue) of the cameras. The baseline Kalibr (magenta) was run on all three cameras. The x-axis of Fig. 10 row denotes the base IMU (GX-25 IMUb) as b and auxiliary IMU (GX-35 IMUa0, Xsens IMUa1, T265 IMU IMUa2) as 0, 1 and 2 respectively. Note that the camera intrinsics are required to be fixed for Kalibr when performing IMU-Camera calibration. Hence there is only one value for each camera intrinsics for Kalibr in Fig. 9.

The range of the boxplot in the figure indicates the convergence repeatability of calibration parameters. The proposed MVIS needs an initial guess for the calibration parameters to start the optimization and the initial guess distribution are shown in the first row of Fig. 9 for the proposed method. The initial guess for d_2 of CAM0 distortion model is within ± 0.5 while the final estimated values are between 0 and 0.1. The initial guess for time offset for CAM0-IMUb is within ± 5 ms, while the final converged values from the proposed MVIS are most cases around ± 0.5 ms. These results show that the calibration parameters can converge robustly with the proposed MVIS.

It can be observed from Fig. 9 and 10 that the calibration estimation convergence of IMU/camera intrinsics and CAM0-IMUb translation are better in blue color than those in green or black colors, which indicate that more cameras can be used to improve overall calibration convergence. This is probably due to improved visual feature estimates from longer feature tracks or wider field-of-view due to multi-view constraints when more cameras are used in the experiment.

11.1.2 Comparison with Kalibr

By comparing the mean values of each boxplot in Fig. 9 and 10, it can be seen that the MVIS can achieve comparable calibration results to Kalibr, which verifies the calibration accuracy of the proposed MVIS.

11.1.3 Comparing IMU Intrinsic Quality

By evaluating the IMU calibration results across the four IMUs of IMUb, IMUa0, IMUa1 and IMUa2 (denoted as b , 0, 1, 2 in the second and third row in Fig. 10) used in the experiments, we clearly see that IMUa2, a relatively low-cost BMI055 IMU, demonstrates larger scale correction for gyroscope and accelerometer than other three high-end IMUs (GX-25 IMUb, GX-35 IMUa0 and Xsens IMUa1). This is expected as the IMUb, IMUa0 and IMUa1 are supposed to have more stable and sophisticated factory calibration than IMUa2. This result, aligned with our previous work for single-IMU-camera calibration [9], further validates the proposed MVIS can generate reasonable and accurate calibration for IMUs.

Note that we have also implemented both numerical and analytical Jacobians for the proposed MVIS. The numerical and analytical Jacobians can achieve similar accuracy results but with 10-14% running time saving when using analytical Jacobians.

11.2 4 IMUs + 2 GS Cameras + 2 RS Cameras

All the four IMUs, GS stereo camera from RealSense T265 and ELP RS stereo camera are used in this evaluation. Both GS and RS cameras are used in this experiment to show that our proposed MVIS supports full-parameter joint calibration with GS and RS cameras, while Kalibr does not support joint calibration of IMU and RS cameras, nor GS and RS cameras. Total 15 datasets were collected with an AprilTag board, on which both the proposed MVIS and the Kalibr calibration toolbox were run to report calibration accuracy and repeatability statistics. During data collection, all 6-axis motion of the VI-Rig were excited to avoid degenerate motions for calibration parameters.

11.2.1 Calibration for IMU and GS/RS

During evaluation, all the GS/RS cameras and IMUs are used for the proposed MVIS. Since Kalibr does not support hybrid calibration of GS and RS cameras, we first run Kalibr with all four IMUs and only GS stereo camera from RealSense T265 (**CAM0&CAM1**). The results with boxplots are presented in Fig. 11. Then, we run Kalibr with all four IMUs and ELP RS stereo camera (**CAM2&CAM3**) using a Kalibr extension [25]. The results are presented in Fig. 12. Note that in the evaluations, the left&right cameras from the stereo of RealSense T265 are denoted as **CAM0&CAM1**, while the left&right cameras from ELP RS stereo are denoted as **CAM2&CAM3**. In this experiment, we did camera calibration for each collected dataset with Kalibr. Therefore, we can have the statistics for the camera intrinsic estimates in Fig. 11 and 12, from which, we can see that the mean estimates of both the IMU and camera related parameters are similar for both the proposed MVIS and Kalibr.

The boxplot ranges of camera and IMU related parameters from the proposed MVIS are much smaller than those of the Kalibr, which shows that MVIS is able to achieve much better estimation convergence and repeatability than Kalibr, especially for the case of using ELP RS cameras. This result verifies that the proposed MVIS can handle the joint calibration of IMU-GS/RS cameras, which is missing from Kalibr. In this experiment, MVIS used both GS/RS cameras while the Kalibr is evaluated on only GS or only RS cameras. Hence, this experiment further proves that the joint calibration of multiple sensors (i.e. cameras) does improve the calibration accuracy and repeatability.

It is interesting to see that the IMU calibration results (the scales for \mathbf{D}_w and \mathbf{D}_a) between these two experiments (Fig. 10 in Section 11.1 and Fig. 11 or Fig. 12 in Section 11.2) are very similar. This further validates the stability of the proposed MVIS.

11.2.2 Evaluation of Multiple Gyroscopes Calibration

We further evaluate the proposed MVIS with multiple auxiliary gyroscopes. With the same 15 datasets, all cameras, base IMU (GX-25 IMUb) and the gyroscopes of three auxiliary IMUs (GX-35 IMUa0, Xsens IMUa1 and T265 IMU IMUa2) are used for evaluation with MVIS. The calibration results of MVIS with these auxiliary gyroscopes (in black), compared to the MVIS (in blue) and Kalibr (in magenta) with full auxiliary IMUs, are shown in Fig. 14. Note that the auxiliary gyroscope does not contain ${}^I_w\mathbf{R}$. Hence, we set ${}^I_w\mathbf{R} = \mathbf{I}_3$ as default.

It is clear from the results that MVIS with multiple auxiliary gyroscopes still can achieve almost the same estimates for gyroscope scales and time offsets as MVIS and Kalibr with full auxiliary IMUs.

At the same time, we can also see that the calibration of rotation between auxiliary gyroscope and base IMU (the second row of Fig. 14) from MVIS with multiple gyroscopes, is slightly worse than that of MVIS and Kalibr with full IMUs, especially for IMUa2. This might be due to the fact

that accelerometer measurement can benefit the extrinsic calibration between IMUs. We also want to point out that the rotation calibration difference is smaller than 0.5° , which is not significant.

11.2.3 Temporal Calibration

The temporal calibration, including time offsets and rolling shutter readout time, are presented in Fig. 13, which shows the results using base IMU and all the full auxiliary IMUs. The 0, 1, 2 and 3 from the **CAM Toff** and **Readout** refers to CAM0 - CAM3. From Fig. 13, it is clear that the time offset calibration is almost the same for the proposed MVIS and the Kalibr. The readout time calibration errors are all within 2 ms.

From the results, we can also find out that the triggering time offset of the RealSence T265 is not stable. As can be seen from the left of Fig. 13, there are outliers as large as 30 ms between the base IMU **IMUb** and the right camera of T265. Similarly, the time offset of the IMU from T265 (**IMUa2**) to base IMU (**IMUb**) is also slightly unstable from the estimates of MVIS and Kalibr, as outliers (red crosses) in right of Fig. 13 are obvious. Note that the 0, 1 and 2 in the plot of **IMU Toff** from right of Fig. 13 denote the time offsets of **IMUa0**, **IMUa1** and **IMUa2** to **IMUb**, respectively.

As shown in the right of Fig. 13, the time offset between based IMU **IMUb** and the auxiliary IMU **IMUa2** (BMI055 from T265) also has 10 ms offsets (from near -5 ms to 5 ms). This is probably due to the build-in drivers of this relatively low-cost sensor (T265). This figure shows that the estimate results from Kalibr (magenta) and the proposed MVIS (blue) can identify the temporal calibration problems of T265, which validates that the proposed MVIS can be used to identify the temporal instability of T265 and provide reliable calibration results.

11.3 Planar Motion with 4 IMUs + 2 GS Cameras

We further verify the degenerate motions with a dataset collected under planar motion. All four IMUs and the GS stereo camera from RealSense T265 are used for data collection. When collecting data, the VI-Rig is put on a chair with wheels and moved about the room in planar motion. The proposed MVIS is run on this dataset 4 times with different perturbations to the initial values of IMU-IMU translations.

Under planar motion, the rotation axis, roughly along the local z-axis for the base IMU, is fixed for the VI-Rig. Hence, the IMU-IMU translation along the rotation axis and the d_{w1} , d_{w2} , d_{w3} from \mathbf{D}_w should be unobservable. The calibration results for these parameters can be clearly seen in Fig. 15 and they diverge erroneously during optimization.

As a comparison, we use the same sensor rig and same perturbations to IMU-IMU translation to run the proposed MVIS under fully-excited motions. The calibration results are shown in Fig. 16. It is clear that all these calibration parameters in Fig. 16, when fully-excited motions are given, can converge nicely compared to Fig. 15.

11.4 Discussion on Estimation Convergence

From the extensive simulations and real world experiments, we find that the convergence of the proposed MVIS with full-parameter calibration can be affected in several aspects. Firstly, based on our analysis, we need fully excited motions (3D rotation and 3D translation) for all the sensors to make sure all the related calibration parameters can converge (see Section 10.1, 11.1 and 11.2). If the MVIS undergoes any degenerate motions listed in Section 9, some calibration parameters' estimates are unlikely to converge (see Section 10.2, 10.3 and 11.3).

Given fully excited motions, the initial guess and prior information for these calibration parameters are also crucial for estimator convergence. As we mentioned in previous sections, the IMU

intrinsics are most cases not large in values. Hence, they are initialized with ideal intrinsic values. The camera intrinsic and distortion parameters are usually initialized based on the camera calibration using OpenCV [35] or Kalibr [21]. But the proposed MVIS can handle inaccurate camera intrinsics as shown in Fig. 9. For the IMU-IMU/Camera extrinsics, the initial orientation part is decided manually while the translation part is hand measured. This can be improved by using trajectory alignment of visual trajectories and IMU integrated trajectory segments. The temporal related parameters are most cases initialized through orientation alignment.

The more sensors are used, the more calibration parameters will be kept in the state vector for the proposed MVIS. This will pose challenges to convergence of the proposed MVIS when estimating all the related calibrations at once, especially when the initial guesses for these calibrations are not of good quality. To address it, we add the cost terms from auxiliary sensors gradually, after base inertial sensor related parameters converge. Throughout our experiments, we first only optimize the base IMU and the cameras related costs until the landmark feature estimates converge. After that, the auxiliary IMUs/gyroscopes cost terms will be added to the NLS for solving their related calibration parameters. Actually, from our experiences on the data collected using VI-Rig, 5-10s of the data with fully-excited motions are good enough for the estimates of landmarks to converge.

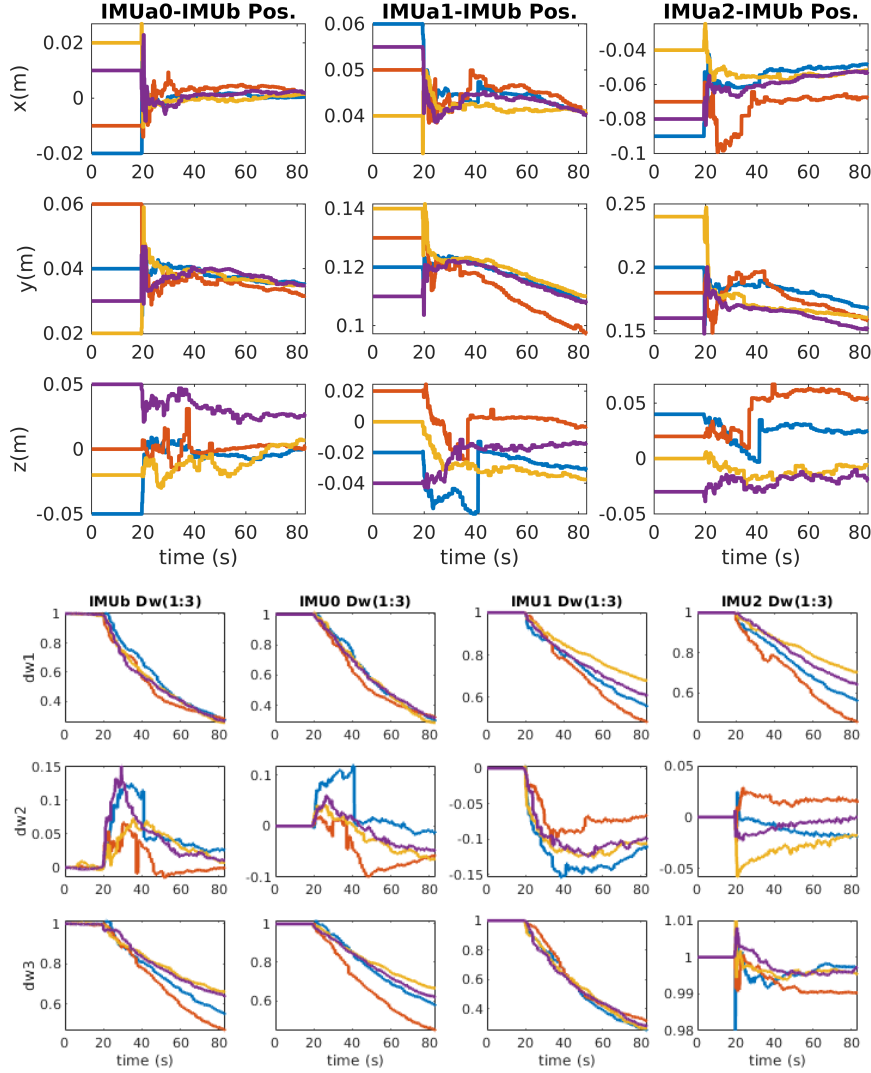


Figure 15: Calibration results for one planar motion dataset collected with Intel Realsense T265 and four IMUs. The translation of IMUb-IMUa_0 , IMUb-IMUa_1 , IMUb-IMUa_2 , the \mathbf{D}_w of IMUb , IMUa_0 , IMUa_1 and IMUa_2 cannot converge under planar motions, which verifies our observability analysis. Different colors represent different initial perturbations to the IMU-IMU translations.

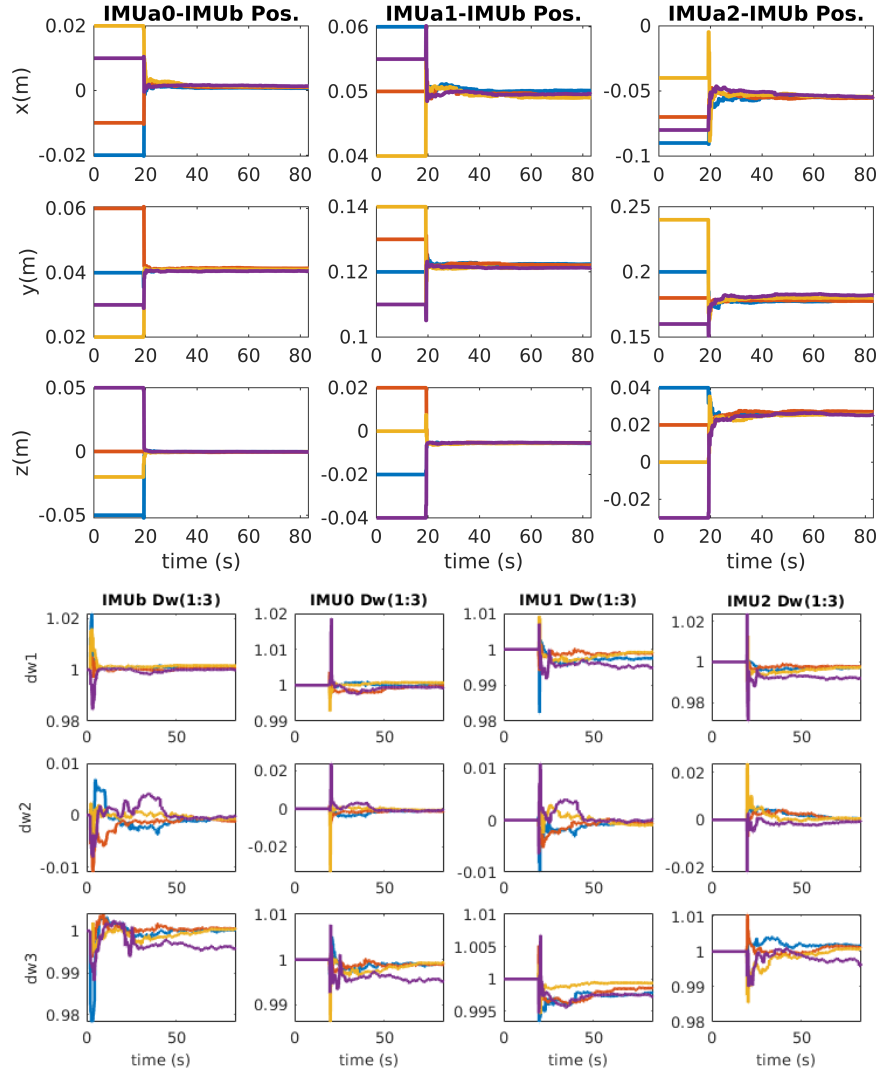


Figure 16: Calibration results for one fully-excited motion dataset collected with Intel Realsense T265 and four IMUs. The translation of IMUb-IMUa0, IMUb-IMUa1, IMUb-IMUa2, the D_w of IMUb, IMUa0, IMUa1 and IMUa2 converge nicely compared to planar motion case. Different colors represent different initial perturbations to the IMU-IMU translations.

Appendix A: Degenerate Motion For Inertial Intrinsics

The degenerate motions for base IMU, auxiliary IMU and auxiliary Gyro are similar. Hence, for simplicity, we save the notation for frame reference and explain the degenerate motion for base IMU as an example.

A.0.1: ${}^w w_1$ constant

If ${}^w w_1$ is constant, d_{a11} will be unobservable with unobservable directions as:

$$\mathbf{N}_{w1} = [\mathbf{0}_{1 \times 9} \quad (\hat{\mathbf{D}}_w^{-1} \mathbf{e}_1)^\top {}^w w_1 \quad \mathbf{0}_{1 \times 3} \quad 1 \quad \mathbf{0}_{1 \times 91}]^\top \quad (206)$$

A.0.2: ${}^w w_2$ constant

If ${}^w w_2$ is constant, d_{a12} and d_{a22} will be unobservable with unobservable directions as:

$$\mathbf{N}_{w2} = \begin{bmatrix} \mathbf{0}_{1 \times 9} & (\hat{\mathbf{D}}_w^{-1} \mathbf{e}_1)^\top {}^w w_2 & \mathbf{0}_{1 \times 4} & 1 & \mathbf{0}_{1 \times 90} \\ \mathbf{0}_{1 \times 9} & (\hat{\mathbf{D}}_w^{-1} \mathbf{e}_2)^\top {}^w w_2 & \mathbf{0}_{1 \times 5} & 1 & \mathbf{0}_{1 \times 89} \end{bmatrix}^\top \quad (207)$$

A.0.3: ${}^w w_3$ constant

If ${}^w w_3$ is constant, d_{a13} , d_{a23} and d_{a33} are unobservable with unobservable directions as:

$$\mathbf{N}_{w3} = \begin{bmatrix} \mathbf{0}_{1 \times 9} & (\hat{\mathbf{D}}_w^{-1} \mathbf{e}_1)^\top {}^w w_3 & \mathbf{0}_{1 \times 6} & 1 & \mathbf{0}_{1 \times 88} \\ \mathbf{0}_{1 \times 9} & (\hat{\mathbf{D}}_w^{-1} \mathbf{e}_2)^\top {}^w w_3 & \mathbf{0}_{1 \times 7} & 1 & \mathbf{0}_{1 \times 87} \\ \mathbf{0}_{1 \times 9} & (\hat{\mathbf{D}}_w^{-1} \mathbf{e}_3)^\top {}^w w_3 & \mathbf{0}_{1 \times 8} & 1 & \mathbf{0}_{1 \times 86} \end{bmatrix}^\top \quad (208)$$

A.0.4: ${}^a a_1$ constant

If ${}^a a_1$ is constant, d_{a11} , pitch and yaw of ${}^I \mathbf{R}$ are unobservable with unobservable directions as:

$$\mathbf{N}_{a1} = \begin{bmatrix} \mathbf{0}_{12 \times 1} & \mathbf{0}_{12 \times 1} & \mathbf{0}_{12 \times 1} \\ \hat{\mathbf{D}}_a^{-1} \mathbf{e}_1 {}^a a_1 & \hat{\mathbf{D}}_a^{-1} \mathbf{e}_2 \hat{d}_{a11} {}^a a_1 & \hat{\mathbf{D}}_a^{-1} \mathbf{e}_3 \hat{d}_{a11} \hat{d}_{a22} {}^a a_1 \\ \mathbf{0}_{6 \times 1} & \mathbf{0}_{6 \times 1} & \mathbf{0}_{6 \times 1} \\ 1 & 0 & 0 \\ 0 & \hat{d}_{a22} & 0 \\ 0 & -\hat{d}_{a12} & 0 \\ 0 & \hat{d}_{a23} & -\hat{d}_{a33} \hat{d}_{a22} \\ 0 & -\hat{d}_{a13} & \hat{d}_{a12} \hat{d}_{a33} \\ 0 & 0 & \hat{d}_{a13} \hat{d}_{a22} - \hat{d}_{a12} \hat{d}_{a23} \\ \mathbf{0}_{3 \times 1} & {}^I \hat{\mathbf{R}} \mathbf{e}_3 & {}^I \hat{\mathbf{R}} (\mathbf{e}_1 \hat{d}_{a12} + \mathbf{e}_2 \hat{d}_{a22}) \\ \mathbf{0}_{77 \times 1} & \mathbf{0}_{77 \times 1} & \mathbf{0}_{77 \times 1} \end{bmatrix}$$

A.0.5: ${}^a a_2$ constant

If ${}^a a_2$ is constant, d_{a12} , d_{a22} and roll of ${}^I \mathbf{R}$ are unobservable with unobservable directions as:

$$\mathbf{N}_{a2} = \begin{bmatrix} \mathbf{0}_{12 \times 1} & \mathbf{0}_{12 \times 1} & \mathbf{0}_{12 \times 1} \\ \hat{\mathbf{D}}_a^{-1} \mathbf{e}_1 {}^a a_2 & \hat{\mathbf{D}}_a^{-1} \mathbf{e}_2 {}^a a_2 & \hat{\mathbf{D}}_a^{-1} \mathbf{e}_3 \hat{d}_{a22} {}^a a_2 \\ \mathbf{0}_{6 \times 1} & \mathbf{0}_{6 \times 1} & \mathbf{0}_{6 \times 1} \\ 0 & 0 & 0 \\ 1 & 0 & 0 \\ 0 & 1 & 0 \\ 0 & 0 & 0 \\ 0 & 0 & \hat{d}_{a33} \\ 0 & 0 & -\hat{d}_{a23} \\ \mathbf{0}_{3 \times 1} & \mathbf{0}_{3 \times 1} & {}^I_a \hat{\mathbf{R}} \mathbf{e}_1 \\ \mathbf{0}_{77 \times 1} & \mathbf{0}_{77 \times 1} & \mathbf{0}_{77 \times 1} \end{bmatrix} \quad (209)$$

A.0.6: ${}^a a_3$ constant

If ${}^a a_3$ is constant, d_{a13} , d_{a23} and d_{a33} are unobservable with unobservable directions as:

$$\mathbf{N}_{a3} = \begin{bmatrix} \mathbf{0}_{1 \times 12} & (\hat{\mathbf{D}}_a^{-1} \mathbf{e}_1)^\top {}^a a_3 & \mathbf{0}_{1 \times 9} & 1 & \mathbf{0}_{1 \times 82} \\ \mathbf{0}_{1 \times 12} & (\hat{\mathbf{D}}_a^{-1} \mathbf{e}_2)^\top {}^a a_3 & \mathbf{0}_{1 \times 10} & 1 & \mathbf{0}_{1 \times 81} \\ \mathbf{0}_{1 \times 12} & (\hat{\mathbf{D}}_a^{-1} \mathbf{e}_3)^\top {}^a a_3 & \mathbf{0}_{1 \times 11} & 1 & \mathbf{0}_{1 \times 80} \end{bmatrix}^\top \quad (210)$$

References

- [1] Guoquan Huang. “Visual-Inertial Navigation: A Concise Review”. In: *Proc. International Conference on Robotics and Automation*. Montreal, Canada, May 2019.
- [2] Anastasios I Mourikis and Stergios I Roumeliotis. “A multi-state constraint Kalman filter for vision-aided inertial navigation”. In: *Proceedings 2007 IEEE International Conference on Robotics and Automation*. IEEE. 2007, pp. 3565–3572.
- [3] Michael Bloesch, Sammy Omari, Marco Hutter, and Roland Siegwart. “Robust visual inertial odometry using a direct EKF-based approach”. In: *2015 IEEE/RSJ international conference on intelligent robots and systems (IROS)*. IEEE. 2015, pp. 298–304.
- [4] Christian Forster, Luca Carlone, Frank Dellaert, and Davide Scaramuzza. “On-Manifold Preintegration for Real-Time Visual–Inertial Odometry”. In: *IEEE Transactions on Robotics* 33.1 (2016), pp. 1–21.
- [5] Tong Qin, Peiliang Li, and Shaojie Shen. “Vins-mono: A robust and versatile monocular visual-inertial state estimator”. In: *IEEE Transactions on Robotics* 34.4 (2018), pp. 1004–1020.
- [6] Patrick Geneva, Kevin Eckenhoff, Woosik Lee, Yulin Yang, and Guoquan Huang. “OpenVINS: A Research Platform for Visual-Inertial Estimation”. In: *Proc. of the IEEE International Conference on Robotics and Automation*. Paris, France, 2020. URL: https://github.com/rpng/open_vins.
- [7] Mrinal K Paul, Kejian Wu, Joel A Hesch, Esha D Nerurkar, and Stergios I Roumeliotis. “A comparative analysis of tightly-coupled monocular, binocular, and stereo VINS”. In: *2017 IEEE International Conference on Robotics and Automation (ICRA)*. IEEE. 2017, pp. 165–172.
- [8] Kevin Eckenhoff, Patrick Geneva, and Guoquan Huang. “MIMC-VINS: A Versatile and Resilient Multi-IMU Multi-Camera Visual-Inertial Navigation System”. In: *IEEE Transactions on Robotics* (Feb. 2021).
- [9] Yulin Yang, Patrick Geneva, Xingxing Zuo, and Guoquan Huang. “Online Self-Calibration for Visual-Inertial Navigation: Models, Analysis, and Degeneracy”. In: *IEEE Transactions on Robotics* (2023), pp. 1–20. DOI: [10.1109/TR0.2023.3275878](https://doi.org/10.1109/TR0.2023.3275878).
- [10] Stefan Leutenegger, Simon Lynen, Michael Bosse, Roland Siegwart, and Paul Furgale. “Keyframe-based visual–inertial odometry using nonlinear optimization”. In: *The International Journal of Robotics Research* 34.3 (2015), pp. 314–334.
- [11] Vladyslav Usenko, Jakob Engel, Jörg Stückler, and Daniel Cremers. “Direct visual-inertial odometry with stereo cameras”. In: *2016 IEEE International Conference on Robotics and Automation (ICRA)*. IEEE. 2016, pp. 1885–1892.
- [12] Ke Sun, Kartik Mohta, Bernd Pfommer, Michael Watterson, Sikang Liu, Yash Mulgaonkar, Camillo J Taylor, and Vijay Kumar. “Robust stereo visual inertial odometry for fast autonomous flight”. In: *IEEE Robotics and Automation Letters* 3.2 (2018), pp. 965–972.
- [13] Juichung Kuo, Manasi Muglikar, Zichao Zhang, and Davide Scaramuzza. “Redesigning SLAM for arbitrary multi-camera systems”. In: *2020 IEEE International Conference on Robotics and Automation (ICRA)*. IEEE. 2020, pp. 2116–2122.

- [14] Carlos Campos, Richard Elvira, Juan J Gómez Rodríguez, José MM Montiel, and Juan D Tardós. “ORB-SLAM3: An Accurate Open-Source Library for Visual, Visual–Inertial, and Multimap SLAM”. In: *IEEE Transactions on Robotics* (2021).
- [15] Bo Fu, Fuzhang Han, Yue Wang, Yanmei Jiao, Xiaqing Ding, Qimeng Tan, Lei Chen, Minhang Wang, and Rong Xiong. “High Precision Multi-Camera Assisted Camera-IMU Calibration: Theory and Method”. In: *IEEE Transactions on Instrumentation and Measurement* (2021).
- [16] Dongshin Kim, Seunghak Shin, and In So Kweon. “On-line initialization and extrinsic calibration of an inertial navigation system with a relative preintegration method on manifold”. In: *IEEE Transactions on Automation Science and Engineering* 15.3 (2017), pp. 1272–1285.
- [17] Kevin Eckenhoff, Patrick Geneva, and Guoquan Huang. “Sensor-Failure-Resilient Multi-IMU Visual-Inertial Navigation”. In: *Proc. International Conference on Robotics and Automation*. Montreal, Canada, May 2019.
- [18] Ming Zhang, Xiangyu Xu, Yiming Chen, and Mingyang Li. “A lightweight and accurate localization algorithm using multiple inertial measurement units”. In: *IEEE Robotics and Automation Letters* 5.2 (2020), pp. 1508–1515.
- [19] Yibin Wu, Jian Kuang, and Xiaoji Niu. “Wheel-INS2: Multiple MEMS IMU-Based Dead Reckoning System With Different Configurations for Wheeled Robots”. In: *IEEE Transactions on Intelligent Transportation Systems* 24.3 (2023), pp. 3064–3077. DOI: [10.1109/TITS.2022.3220508](https://doi.org/10.1109/TITS.2022.3220508).
- [20] Marsel Faizullin and Gonzalo Ferrer. “Best Axes Composition extended: Multiple gyroscopes and accelerometers data fusion to reduce systematic error”. In: *Robotics and Autonomous Systems* 160 (2023), p. 104316. ISSN: 0921-8890. DOI: <https://doi.org/10.1016/j.robot.2022.104316>. URL: <https://www.sciencedirect.com/science/article/pii/S0921889022002056>.
- [21] Paul Furgale, Joern Rehder, and Roland Siegwart. “Unified temporal and spatial calibration for multi-sensor systems”. In: *2013 IEEE/RSJ International Conference on Intelligent Robots and Systems*. IEEE. 2013, pp. 1280–1286.
- [22] Joern Rehder, Janosch Nikolic, Thomas Schneider, Timo Hinzmann, and Roland Siegwart. “Extending kalibr: Calibrating the extrinsics of multiple IMUs and of individual axes”. In: *2016 IEEE International Conference on Robotics and Automation (ICRA)*. IEEE. 2016, pp. 4304–4311.
- [23] Xiangyang Zhi, Jiawei Hou, Yiren Lu, Laurent Kneip, and Sören Schwertfeger. “Multical: Spatiotemporal Calibration for Multiple IMUs, Cameras and LiDARs”. In: *2022 IEEE/RSJ International Conference on Intelligent Robots and Systems (IROS)*. 2022, pp. 2446–2453. DOI: [10.1109/IROS47612.2022.9982031](https://doi.org/10.1109/IROS47612.2022.9982031).
- [24] Mingyang Li, Hongsheng Yu, Xing Zheng, and Anastasios I Mourikis. “High-fidelity sensor modeling and self-calibration in vision-aided inertial navigation”. In: *2014 IEEE International Conference on Robotics and Automation (ICRA)*. IEEE. 2014, pp. 409–416.
- [25] Jianzhu Huai, Yuan Zhuang, Yukai Lin, Grzegorz Jozkow, Qicheng Yuan, and Dong Chen. “Continuous-Time Spatiotemporal Calibration of a Rolling Shutter Camera-IMU System”. In: *IEEE Sensors Journal* 22.8 (2022), pp. 7920–7930. DOI: [10.1109/JSEN.2022.3152572](https://doi.org/10.1109/JSEN.2022.3152572).
- [26] Yulin Yang, B. P. W. Babu, Chuchu Chen, Guoquan Huang, and Liu Ren. “Analytic Combined IMU Integration for Visual-Inertial Navigation”. In: *Proc. of the IEEE International Conference on Robotics and Automation*. Paris, France, 2020.

- [27] Kevin Eckenhoff, Patrick Geneva, and Guoquan Huang. “Closed-form Preintegration Methods for Graph-based Visual-Inertial Navigation”. In: *International Journal of Robotics Research* 38.5 (2019), pp. 563–586.
- [28] Médéric Fourmy, Thomas Flayols, Pierre-Alexandre Léziart, Nicolas Mansard, and Joan Solà. “Contact Forces Preintegration for Estimation in Legged Robotics using Factor Graphs”. In: *2021 IEEE International Conference on Robotics and Automation (ICRA)*. 2021, pp. 1372–1378. DOI: [10.1109/ICRA48506.2021.9561037](https://doi.org/10.1109/ICRA48506.2021.9561037).
- [29] Adnane Jadid, Linda Rudolph, Frieder Pankratz, and Gudrun Johanna Klinker. “Utilizing Multiple Calibrated IMUs for Enhanced Mixed Reality Tracking”. In: *2019 IEEE International Symposium on Mixed and Augmented Reality Adjunct (ISMAR-Adjunct)* (2019), pp. 384–386.
- [30] Jongwon Lee, David Hanley, and Timothy Bretl. “Extrinsic Calibration of Multiple Inertial Sensors From Arbitrary Trajectories”. In: *IEEE Robotics and Automation Letters* 7.2 (2022), pp. 2055–2062. DOI: [10.1109/LRA.2022.3143290](https://doi.org/10.1109/LRA.2022.3143290).
- [31] Lintong Zhang, David Wisth, Marco Camurri, and Maurice Fallon. “Balancing the Budget: Feature Selection and Tracking for Multi-Camera Visual-Inertial Odometry”. In: *IEEE Robotics and Automation Letters* 7.2 (2022), pp. 1182–1189. DOI: [10.1109/LRA.2021.3137910](https://doi.org/10.1109/LRA.2021.3137910).
- [32] Thomas Schneider, Mingyang Li, Cesar Cadena, Juan Nieto, and Roland Siegwart. “Observability-aware self-calibration of visual and inertial sensors for ego-motion estimation”. In: *IEEE Sensors Journal* 19.10 (2019), pp. 3846–3860.
- [33] David Schubert, Thore Goll, Nikolaus Demmel, Vladyslav Usenko, Jörg Stückler, and Daniel Cremers. “The TUM VI Benchmark for Evaluating Visual-Inertial Odometry”. In: *2018 IEEE/RSJ International Conference on Intelligent Robots and Systems (IROS)*. 2018, pp. 1680–1687. DOI: [10.1109/IROS.2018.8593419](https://doi.org/10.1109/IROS.2018.8593419).
- [34] Yulin Yang, Patrick Geneva, Xingxing Zuo, and Guoquan Huang. “Online IMU Intrinsic Calibration: Is It Necessary?” In: *Proc. of the Robotics: Science and Systems*. Paris, France, 2020.
- [35] OpenCV Developers Team. *Open Source Computer Vision (OpenCV) Library*. Available: <http://opencv.org>. 2021.
- [36] Chao Guo, Dimitrios Kottas, Ryan DuToit, Ahmed Ahmed, Ruipeng Li, and Stergios Roumeliotis. “Efficient Visual-Inertial Navigation using a Rolling-Shutter Camera with Inaccurate Timestamps”. In: Berkeley, CA, 2014.
- [37] Timothy D Barfoot. *State estimation for robotics*. Cambridge University Press, 2017.
- [38] Andreas Wächter and Lorenz T Biegler. “On the implementation of an interior-point filter line-search algorithm for large-scale nonlinear programming”. In: *Mathematical programming* 106 (2006), pp. 25–57.
- [39] Rainer Kümmel, Giorgio Grisetti, Hauke Strasdat, Kurt Konolige, and Wolfram Burgard. “G2o: A general framework for graph optimization”. In: *2011 IEEE International Conference on Robotics and Automation*. 2011, pp. 3607–3613. DOI: [10.1109/ICRA.2011.5979949](https://doi.org/10.1109/ICRA.2011.5979949).
- [40] Frank Dellaert. *Factor graphs and GTSAM: A hands-on introduction*. Tech. rep. Georgia Institute of Technology, 2012.
- [41] Sameer Agarwal, Keir Mierle, and The Ceres Solver Team. *Ceres Solver*. Version 2.2. Oct. 2023. URL: <https://github.com/ceres-solver/ceres-solver>.

- [42] Andela Jurić, Filip Kendeš, Ivan Marković, and Ivan Petrović. “A Comparison of Graph Optimization Approaches for Pose Estimation in SLAM”. In: *2021 44th International Convention on Information, Communication and Electronic Technology (MIPRO)*. 2021, pp. 1113–1118. DOI: [10.23919/MIPRO52101.2021.9596721](https://doi.org/10.23919/MIPRO52101.2021.9596721).
- [43] Nikolas Trawny and Stergios I Roumeliotis. “Indirect Kalman filter for 3D attitude estimation”. In: *University of Minnesota, Dept. of Comp. Sci. & Eng., Tech. Rep* 2 (2005), p. 2005.
- [44] Joan Sola. “Quaternion kinematics for the error-state Kalman filter”. In: *arXiv preprint arXiv:1711.02508* (2017).
- [45] Vladyslav Usenko, Nikolaus Demmel, David Schubert, Jörg Stückler, and Daniel Cremers. “Visual-Inertial Mapping With Non-Linear Factor Recovery”. In: *IEEE Robotics and Automation Letters* 5.2 (2020), pp. 422–429. DOI: [10.1109/LRA.2019.2961227](https://doi.org/10.1109/LRA.2019.2961227).
- [46] Gregory S Chirikjian. *Stochastic models, information theory, and Lie groups, volume 2: Analytic methods and modern applications*. Vol. 2. Springer Science & Business Media, 2011.
- [47] Guoquan Huang. “Improving the Consistency of Nonlinear Estimators: Analysis, Algorithms, and Applications”. PhD thesis. Department of Computer Science and Engineering, University of Minnesota, 2012. URL: <https://conservancy.umn.edu/handle/11299/146717>.
- [48] Agostino Martinelli. “Observability properties and deterministic algorithms in visual-inertial structure from motion”. In: *Foundations and Trends in Robotics* (2013), pp. 1–75.
- [49] Kejian J Wu, Chao X Guo, Georgios Georgiou, and Stergios I Roumeliotis. “Vins on wheels”. In: *2017 IEEE International Conference on Robotics and Automation (ICRA)*. IEEE. 2017, pp. 5155–5162.
- [50] Yulin Yang, Patrick Geneva, Kevin Eckenhoff, and Guoquan Huang. “Degenerate Motion Analysis for Aided INS with Online Spatial and Temporal Calibration”. In: *IEEE Robotics and Automation Letters (RA-L)* 4.2 (2019), pp. 2070–2077.
- [51] Woosik Lee, Kevin Eckenhoff, Yulin Yang, Patrick Geneva, and Guoquan Huang. “Visual-Inertial-Wheel Odometry with Online Calibration”. In: *Proc. of the IEEE/RSJ International Conference on Intelligent Robots and Systems*. Las Vegas, NV, 2020.
- [52] J. A. Hesch, D. G. Kottas, S. L. Bowman, and S. I. Roumeliotis. “Consistency Analysis and Improvement of Vision-aided Inertial Navigation”. In: *IEEE Transactions on Robotics* 30.1 (2014), pp. 158–176.
- [53] Yulin Yang and Guoquan Huang. “Observability Analysis of Aided INS with Heterogeneous Features of Points, Lines and Planes”. In: *IEEE Transactions on Robotics* 35.6 (Dec. 2019), pp. 399–1418.
- [54] Mingyang Li and Anastasios I. Mourikis. “Vision-aided inertial navigation with rolling-shutter cameras”. In: *International Journal of Robotics Research* 33.11 (Sept. 2014), pp. 1490–1507.